# Northumbria Research Link

# Advances in designs and mechanisms of semiconducting metal oxide nanostructures for high-precision gas sensors operated at room-temperature

Zhijie Li [a], Hao Li [a], Zhonglin Wu [a], Mingkui Wang [b], Jingting Luo [c], Hamdi Torun [d], Pingan Hu [e], Chang Yang [f], Marius Grundmann [f], Xiaoteng Liu [d], YongQing Fu [d,a]*

[a] School of Physics, University of Electronic Science and Technology of China, Chengdu, 610054, P. R. China

[b] Wuhan National Laboratory for Optoelectronics, Huazhong University of Science and Technology, Luoyu Road 1037, Wuhan 430074, P. R. China

[c] Shenzhen Key Laboratory of Advanced Thin Films and Applications, College of Physics and Energy, Shenzhen University, 518060 Shenzhen, China

[d] Faculty of Engineering and Environment, Northumbria University, Newcastle Upon Tyne, NE1 8ST, UK

[e] Key Laboratory of Micro-systems and Micro-structures Manufacturing of Ministry of Education, Harbin Institute of Technology, Harbin 150080, P. R. China.

[f] Felix-Bloch-Institut für Festkörperphysik, Universität Leipzig, Linnéstr. 5, 04103 Leipzig, Germany

- Corresponding author: Prof. Richard Yongqing Fu, e-mail: richard.fu@northumbria.ac.uk

**Abstract**

High-precision gas sensors operated at room temperature are attractive for various real-time gas monitoring applications, with advantages including low energy consumption, cost effectiveness and device miniaturization/flexibility. Sensing materials, which play a key role for the good gas sensing performance, are currently focused extensively on semiconducting metal oxide nanostructures (SMONs) used in the conventional resistance type gas sensors. This topical review highlights the designs and mechanisms of different SMONs with various patterns (e.g. nanoparticles, nanowires, nanosheets, nanorods, nanotubes, nanofilms, etc.) for gas sensors to detect various hazardous gases at the room temperature. The key topics include: (1) single phase SMONs including both n-type and p-type ones; (2) noble metal nanoparticles and metal ion modified SMONs; (3) composite oxides of SMONs; (4) composites of SMONs with carbon nanomaterials. Enhancement of sensing performance of the SMONs at the room temperature can also be enhanced using photo-activation effect such as ultraviolet light. The SMON based mechanically flexible and wearable room temperature gas sensors are also discussed. Various mechanisms have been discussed for the enhanced sensing performance, which include redox reactions, heterojunction generation, formation of metal sulfides and spillover effect. Finally, major challenges and prospects for the SMONs based room temperature gas sensors are highlighted.

**Key words:** Semiconducting metal oxide; Nanostructure; Gas sensor; Hazardous gas; Sensing mechanism; Sensing performance.

**Contents**

## 1. Introduction

Various types of hazardous gases, such as $H_2S$, $CO$, $NO_2$, $NH_3$, $H_2$, $CH_4$, toluene, acetone, ethanol, methanol and benzene, are routinely and daily released from industrial and agriculture processes, or emitted as vehicle exhaust emissions. Some of them, such as $H_2$ and $CH_4$, are explosive when exposed to air, whereas the others, such as $NO_2$ and toluene, are harmful for human health and environment, when their concentrations are above a critical threshold, sometimes as low as in parts-per-million (ppm) levels. Therefore, development of high-precision gas sensors with high sensitivity, fast response, good selectivity, low limit of detection (LOD), as well as *in-situ* and real-time monitoring capabilities is paramount [1, 2]. For this purpose, various types of gas sensors have been developed, mainly including resistive [3-5], optical [6-9], ultrasonic and acoustic wave [10-12], thermoelectric [13, 14] and electrochemical [15-17] ones.
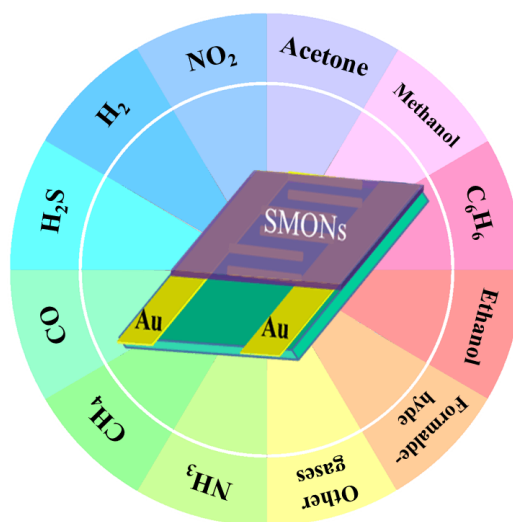


Fig. 1. Schematic diagram of resistance-type gas sensors based on semiconducting metal oxide nanostructures for detection of various hazardous gases.

Among these gas sensors, the resistive gas sensor is one of the most popular types, and is simple and easy to be fabricated using cost effective processes. The transduction mechanism of resistive gas sensors is based on the change in resistance of a sensing layer upon adsorption and reaction with the target gas molecules. The sensing layer usually determines the sensitivity and selectivity. Therefore, the sensing materials and the structures of the sensing layer are highly critical to their sensing performance. The

sensing materials used in these resistive gas sensors are mainly semiconducting metal oxide nanostructures (SMONs) [18-21], carbon materials [22-26] and organic semiconductors [27-30]. Compared to the carbon materials and organic semiconductors, the SMONs generally have higher sensitivity, quicker response/recovery speed, better reversibility and stability, and they are cost-effective with simple fabrication processes [18-20]. The SMONs have large specific surface areas with numerous active sites, which facilitate fast adsorption and reaction of target gases, thus enhancing their sensing performance. They have been used to detect various hazardous gases for different applications as shown in Fig. 1. These SMON sensing materials mainly include $ZnO$ [31, 32], $CuO$ [33-36], $SnO_2$ [37-39], $TiO_2$ [40, 41], $Fe_2O_3$ [42, 43], $In_2O_3$ [44-47], $Co_3O_4$ [48-50] and $WO_3$ [18, 51]. For further improvement of sensing performance, they have been modified using noble metals [52-55], metal ions [56-60], and carbon materials [61-64]. Composites of multi-phase SMONs [65-67] have also been frequently reported.

SMONs-based sensors are usually heated to a higher temperature (between 100 °C to 400 °C) for performance enhancement at the expense of structural complications [42-47]. Operation at elevated temperature levels significantly increases the energy-consumption, overall device size and cost of gas sensors. Heating up to a high temperature could lead to changes of microstructure of the sensing nanomaterials, which can result in degradation of sensing performance. In addition, high-temperature sensing has its practical limitations. Particularly, heating is very dangerous for the detection of flammable and explosive gases, with a risk of explosion. Therefore, sensors operated at room temperature (RT) are desirable for minimizing energy consumption and cost, increasing security and stability, realizing device miniaturization and suitability for handheld operations [68, 69]. For these reasons, RT gas sensors based on the SMONs receive extensive attention in recent years. Different configurations of SMONs employing nanostructures have been demonstrated with desirable performance enhancements [70], regarding to sensitivity, response/recovery time, selectivity, reversibility, reproducibility and long-term stability. Various MSONs have been designed and synthesized, such as nanorods [71-75], nanoparticles [76-81], nanowires [82-89], nanospheres [90], nanosheets [91-94], nanotubes [95-98], and mesoporous nanostructures [99-103].

The literature in SNOM-based RT gas sensing is rich and the application area is very critical. New devices have been regularly introduced. Although the merits of the SMONs based RT gas sensors have already been demonstrated, currently there are still some key challenges:

(1) The sensing performance of these SMON based gas sensors is limited, when operated at RT. For example, many of these sensors exhibit insufficient sensitivities [104-108].

(2) The response/recovery times of many RT gas sensors, which are crucial for rapid detection of target dangerous gases to timely trigger an alarm, are generally quite long, sometimes, up to tens of minutes [109-111].

(3) Poor reversibility has been reported for some of these sensors operated at RT [101].

(4) Poor selectivity is another key limitation for the RT gas sensors. Selectivity of many SMON based RT gas sensors needs to be improved to avoid interference and cross-talks [112].

The aim of this topical review is to critically evaluate the design and structure of SMONs-based gas sensors that may help guide the design of new devices. The performance of these SMONs based gas sensors operated at RT could be improved significantly by modifying the SMONs using noble metal nanoparticles [113-116], metal ions [117-119], composites of multiple-SMON [120-123] and carbon nanomaterials [124-126]. In addition, not only the quantity of chemisorbed oxygen species [127], defects [128] and element compositions [129, 130] on the surface of SMONs, but also the structural properties, i.e. porosity [131], heterojunction properties [132-134] and conductivity [135, 136] can affect the RT gas sensing performance. Therefore, understanding the relationship between sensing properties and structures of SMONs is crucial to design the gas sensing materials with the good sensing performance operated at RT.

Several review papers have been published on gas sensors based on the different SMON sensing materials, including n-type oxide semiconductors such as ZnO [20, 137], $Fe_2O_3$ [138], $SnO_2$ [39, 139, 140], p-type oxide semiconductors [141], metal oxide-based heterojunctions [142], noble metal/metal oxide semiconductors [143, 144] and graphene-metal oxide nanohybrids [145]. However, these review papers discuss the sensing properties of

the sensors which are generally operated at higher working temperatures above RT [146-150]. Others about the RT gas sensors are focused more on certain types of SMONs based on RT sensors. such as nanostructured ZnO based RT gas sensors [151]. However, there is no comprehensive review which is focused on the recent progress of various SMONs for high-precision gas sensors operated at RT. Therefore, this review will comprehensively summarize and discuss the recent developments of the RT gas sensors based on single phase SMONs, noble metal and metal ion modified SMONs, composites of SMONs with other metal oxides, and the composites of SMONs with carbon nanomaterials, as shown in the Fig. 2. In addition, we will discuss the effect of UV light stimulation to enhance the performance of SMONs based RT gas sensors, and mechanically flexible RT gas sensors based on the SMONs.
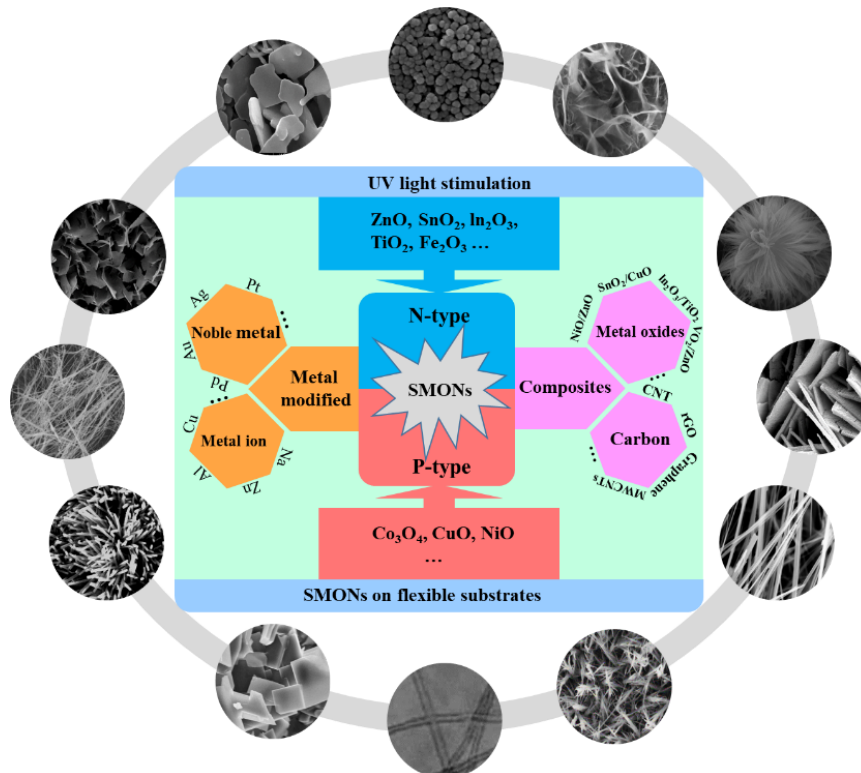


Fig. 2. Schematic diagram of various semiconducting metal oxide nanostructures used for RT gas sensors presented in this review.

## 2. Room temperature gas sensors based on single phase semiconducting metal oxide nanostructures

### 2.1 N-type semiconducting metal oxide nanostructures and gas sensors

N-type SMONs are the most reported sensing materials for the RT resistive gas sensors, and they include ZnO [152-156], SnO$_2$ [157-160], In$_2$O$_3$ [161], WO$_3$ [162], TiO$_2$ [163-166], Fe$_2$O$_3$ [167-169], MoO$_3$ [170], VO$_2$ [171] and CeO$_2$ [172]. Various forms of nanostructures including nanoparticles, nanorods, nanowires, nanoflowers, nanosheets, nanofilms, nanotubes, porous structures and hierarchical nanostructures have been employed to detect various types of gases including H$_2$S [99, 101], NO$_2$ [157], H$_2$ [173], NH$_3$ [174], acetone [175], alcohol [106], HCHO [176], liquefied petroleum gas (LPG), etc. Table 1 summarizes some of the reported RT sensors using the n-type SMONs.

Table 1 Summary of room temperature sensing properties of n-type semiconducting metal oxide nanostructures

| Material | Structure | Synthesis method | Target gas | C (ppm) | Response | $t_{res}/t_{rec}$ | LOD | Ref. |
|----------|-----------|------------------|-----------|---------|----------|-------------------|-----|------|
| ZnO | Combs | CVD | H$_2$S | 4 | 6 | 22/540 s | 100 ppb | [152] |
| ZnO | Dendritic | Vapor-phase transport | H$_2$S | 500 | 26.4 | 20/50 s | 10 ppm | [153] |
| ZnO | Nanorods | Hydrothermal | H$_2$S | 1 | ~35 | ~20/- min | 0.05 ppm | [109] |
| ZnO | quantum dots | Colloidal progress | H$_2$S | 50 | 113.5 | 16/820 s | 10 ppm | [177] |
| ZnO | Nanorods | Vapor-phase transport | H$_2$S | 1 | 296 | 320/3592 s | 0.5 ppm | [71] |
| ZnO | Thin films | Thermal evaporation | Ethanol | 100 | 3 | - | - | [178] |
| ZnO | Tetrapod network | Thermal oxidation | Ethanol | 1000 | ~4.5 | 300/- s | ~10 ppm | [179] |
| ZnO | Nanorods | Laser ablation | Ethanol | 250 | 14 | - | ~1 ppm | [154] |
| ZnO | Nanorods | Electrospinning | Ethanol | 100 | 23 | 26/43 s | ~1 ppm | [180] |
| ZnO | Nanowires | Electrospinning | Ethanol | 100 | 78 | 9/12 s | ~1 ppm | [82] |
| ZnO | Nanorods | Wet chemical route | NH$_3$ | 200 | 24.1 | 239/398 s | ~50 ppm | [181] |
| ZnO | Nanowires | AAO template | NH$_3$ | 50 | 68[#] | 28/29 s | ~10 ppm | [83] |
| ZnO | Thin film | Spray pyrolysis | NH$_3$ | 25 | 233 | 20/25 s | 5 ppm | [182] |
| ZnO | Thin films | Magnetron sputtering | NH$_3$ | 100 | 304 | 92/113 s | 5 ppm | [112] |
| ZnO | Nanowalls | Solution | NO$_2$ | 50 | ~6.2 | 23/11 s | ~5 ppm | [91] |
| ZnO | Nanowire | Drop-cast | NO$_2$ | 20 | 32 | 72/69 s | ~5 ppm | [183] |
| ZnO | Nanorods | Wet chemical route | NO$_2$ | 1 | 100[#] | ~5 /~20 min | ~1 ppm | [110] |
| ZnO | Nanowires | CVD | NO | 10 | 46[#] | - | 1.5 ppm | [184] |
| ZnO | Nanocomb | CVD | CO | 250 | 7.22 | 200/50 s | - | [185] |
| ZnO | Nanorod array | Microwave hydrolysis | CO | 100 | 81.1[#] | -/2.5 min | 10 ppm | [72] |

| Material | Morphology | Method | Gas | Conc | Response | Res/Rec time | Limit | Ref |
|---|---|---|---|---|---|---|---|---|
| ZnO | Nanowires | CVD | $H_2$ | 121 | 8[#] | 29/- s | - | 108 |
| ZnO | Nanorods | Chemical deposition | $H_2$ | 150 | ~2[#] | 50-80/- s | - | 186 |
| ZnO | Nanorods | Hydrothermal | $H_2$ | 200 | ~4[#] | 30s/50-90 s | ~1 ppm | 187 |
| ZnO | Nanotubes | Aqueous chemical | $H_2$ | 500 | 29.6[#] | - | - | 188 |
| ZnO | Thin film | Spray pyrolysis | $H_2$ | 150 | 63 | 320/200 s | - | 189 |
| ZnO | Nanorods | RF magnetron sputtering | $H_2$ | 1000 | 91[#] | 18.8/~130 s | 0.2 ppm | 173 |
| ZnO | Nanorod array | Atomic layer deposition | $H_2$ | 500 | 162 | 30/- s | 5 ppm | 190 |
| ZnO | Nanorod array | Chemical deposition | $H_2$ | 1000 | 500[#] | 176/116 s | - | 191 |
| $MoO_3$ | Nanoribbons | Hydrothermal | $H_2$ | 1000 | 90[#] | 14.1/- s | 0.5 ppm | 192 |
| $SnO_2$ | Nano-film | Sol‐gel | $H_2$ | 1000 | 2570[#] | 192/95 s | - | 193 |
| $SnO_2$ | Nanotubes | Electrospinning | $NO_x$ | 9.7 | 89.2[#] | 6/218 s | 9.7 ppb | 95 |
| $SnO_2$ | Nanocrystals | Chemical precipitation | $NO_2$ | 11 | 33[*] | 100/250 s | ~3 ppm | 76 |
| $SnO_2$ | Thin films | Pulsed laser deposition | $NO_2$ | 4 | 7730 | 3/176 s | ~4 ppm | 157 |
| $SnO_2$ | Thin film | Sol‐gel | Ozone | 0.5 | 3.1 | 15/12 min | - | 194 |
| $SnO_2$ | Nanorods | Microwave | $O_2$ | 10 | ~16.5[*] | ~200/~50 s | ~1 ppm | 73 |
| $SnO_2$ | Nanoporous | Hydrothermal | Acetone | 100 | 14.64[*] | 30/20 s | ~10 ppm | 99 |
| $SnO_2$ | nanocrystals | Sol‐gel | $NH_3$ | 50 | 694.4[#] | 175/210 s | - | 158 |
| $SnO_2$ | Nanowires | Precipitation | Ethanol | 6000 | 8000 | - | - | 88 |
| $In_2O_3$ | Nanowire | CVD | $H_2S$ | 20 | 2 | 48/56 s | 1 ppm | 84 |
| $In_2O_3$ | Whisker | Carbothermal | $H_2S$ | 10 | 30[#] | 4/120 min | 200 ppb | 104 |
| $In_2O_3$ | Nanotubes | Electrospinning | $H_2S$ | 20 | 167 | 287/636 s | ~1 ppm | 161 |
| $In_2O_3$ | Nanotubes | Electrospinning | $H_2S$ | 50 | 320.14 | 45/127 s | 200 ppb | 100 |
| $In_2O_3$ | Porous thin film | Template | $H_2S$ | 50 | 240000 | 140/- s | 1 ppm | 101 |
| $In_2O_3$ | Microcrystallite | Thermal oxidation | $NH_3$ | 1000 | 92[#] | 100/60 s | ~250 ppm | 195 |
| $In_2O_3$ | Nanotubes | Precipitation | $NH_3$ | 20 | 2500 | <20/20 s | ~5 ppm | 111 |
| $In_2O_3$ | Octahedrons | Sol‐gel | $NO_2$ | 200 | ~70 | ~500/~500 s | 0.1 ppm | 196 |
| $In_2O_3$ | Mesoporous nanocrystals | Hydrothermal | $NO_x$ | 97 | 158.7[*] | 96/- s | 970 ppb | 102 |
| $In_2O_3$ | Cubic crystals | Hydrothermal | Ethanol | 100 | 1.4 | 5/3 s | ~10 ppm | 105 |
| $WO_{3-x}$ | Quantum dots | Solvothermal | HCHO | 100 | 1.6 | 2/3 min | 1.5 ppm | 77 |
| $WO_3$ | Nanocolumns | Hydrothermal | Isopropanol | 200 | 6.7 | 53/274 s | 1 ppm | 162 |

| | | | | | | | | |
|---|---|---|---|---|---|---|---|---|
| WO$_3$ | Nano-film | Thermal evaporation | Ethanol | 30 | 35[#] | ~300/300 min | ~10 ppm | [106] |
| TiO$_2$ | Thin film | Anodic oxidation | NH$_3$ | 100 | 0.32[*] | <2/2 min | ~50 ppm | [107] |
| TiO$_2$ | Quantum dot | Hydrolysis method | NH$_3$ | 0.2 | 2.13 | 88/23 s | 0.2 ppm | [164] |
| TiO$_2$ | Nano-film | Sol-gel | NH$_3$ | 50 | 35[#] | 4/6 min | ~10 ppm | [163] |
| TiO$_2$ | Nano-film | Magnetron sputtering | NH$_3$ | 100 | 7857 | 34/90 s | 5 ppm | [174] |
| TiO$_2$ | Nanoparticles | Sol-gel | NH$_3$ | 100 | 10080.8 | 35.5/59 s | ~1 ppm | [78] |
| TiO$_2$ | Nanodots | Nano-oxidation | NO | 10 | 31[#] | 91/184 s | ~5 ppm | [165] |
| TiO$_2$ | Nanoparticles | Hydrothermal | NO$_2$ | 40 | 1093 | 48/52 s | 0.02 ppm | [79] |
| TiO$_2$ | Nanorods | Hydrothermal | CH$_4$ | 60 | 6028 | - | 5 ppm | [166] |
| TiO$_2$ | Nanorods | Acid vapor oxidation | O$_2$ | 40000 | 1.68 | 40/75 s | 1000 ppm | [74] |
| TiO$_2$ | Nanotubes | Electrochemical anodization | CHCl$_3$ | 20000 | ~0.76 | ~3/- min | 1000 ppm | [167] |
| TiO$_2$ | Thin film | Magnetron sputtering | CH$_3$NH$_2$ | 10 | 11.3[#] | 200/260 s | ~2 ppm | [197] |
| TiO$_2$ | Nanotube arrays | Electrochemical anodization | HCHO | 50 | ~37[#] | 3/- min | 0.04 ppm | [176] |
| TiO$_2$ | Nanotubes | Electrochemical anodization | Methanol | 1000 | 60[#] | 34/130 s | 10 ppm | [96] |
| TiO$_2$ | Nanotubes | Electrochemical | Acetone | 100 | 70.18[#] | 19/14 s | ~10 ppm | [97] |
| Fe$_2$O$_3$ | Nanoparticles | Hydrothermal | H$_2$S | 100 | 38.4 | ~180/~3700 s | 50 ppb | [80] |
| Fe$_2$O$_3$ | Nanonails | Screen printing | LPG | 20000 | 51 | 120/150 s | 5000 ppm | [168] |
| MoO$_3$ | Thin film | Magnetron sputtering | NO | 200 | 92[#] | 30/1500 s | 5 ppm | [170] |
| VO$_2$ | Nanorods | CVD | NO$_2$ | 5 | 2.42 | 59/86 s | ~1 ppm | [171] |
| VO$_2$ | Nanorods | Thermal evaporation | CH$_4$ | 500 | 35[*] | 75/158 s | ~100 ppm | [75] |
| V$_2$O$_5$ | Nanoneedles | Vapor deposition | Acetone | 1.7 | 1.025 | 73/- s | 941 ppb | [175] |
| CeO$_2$ | Nanowires | Hydrothermal | H$_2$S | 0.05 | 1.11 | 24/15 s | 50 ppb | [86] |

*Notes:*

*C = concentration;*

*t$_{res}$/t$_{rec}$ = response time /recovery time;*

*LOD = limit of detection;*

*Response is defined as Ra/Rg (for reducing gases) or Rg/Ra (for oxidizing gases), Ra: resistance of the sensor exposed to reference, Rg: resistance of the sensor exposed to target:*

*\* Here the response is defined as ΔR/Rg (for reducing gases) or ΔR/Ra (for oxidizing gases), ΔR: the change in resistance.*

*# Here the response is defined as (ΔR/Rg)×100% (for reducing gases) or (ΔR/Ra)×100% (for oxidizing gases).*

### 2.1.1 Gas sensing mechanisms

Gas sensing mechanism of semiconductor oxides based resistive sensor is mostly based on the changes of resistance after they are exposed to the target gases due to the chemical interactions between target gas molecules and the adsorbed oxygen ions on the surface of SMONs [153, 154]. Conductance of n-type SMONs relies on electron carriers. When the n-type SMONs are surrounded by air, the oxygen molecules are absorbed on their surfaces. The absorbed oxygen molecules extract electrons from the conduction band of surface layer, which results in the formation of negatively charged chemisorbed oxygen ions including $O_2^-$, $O^-$ and $O^{2-}$ at different operating temperatures. Due to the decrease in the electron density, an electron depletion layer is formed on the surface of SMONs and a potential barrier is generated [42, 43]. Therefore, the conductivity of the SMONs decreases, thus resulting in an increased resistance.

The operation temperature of gas sensors determines the types of chemisorbed oxygen ions. For example, they are mainly $O_2^-$ when the temperature is below 100 °C. When the working temperature is increased between 100 °C and 300 °C, the $O_2^-$ ions will capture electrons and then transfer into $O^-$ ions. The $O^-$ can be converted into $O^{2-}$ ions at a higher working temperature above 300 °C. The formation process of oxygen ions can be summarized using the following equations [42, 43]:

$$O_{2\ (gas)} \leftrightarrow O_{2\ (ads)} \tag{1}$$

$$O_{2\ (ads)} + e^- \leftrightarrow O_{2\ (ads)}^- \quad (<100\ ^oC) \tag{2}$$

$$O_{2\ (ads)}^- + e^- \leftrightarrow 2O_{\ (ads)}^- \quad (100\ ^oC\text{-}300\ ^oC) \tag{3}$$

$$O_{\ (ads)}^- + e^- \leftrightarrow O_{\ (ads)}^{2-} \quad (>300\ ^oC) \tag{4}$$
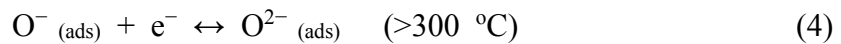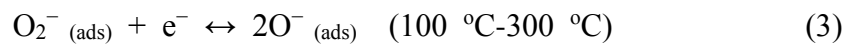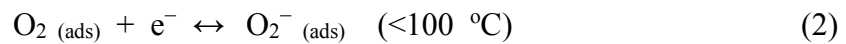
Therefore, at RT, the oxygen ions on the surface of n-type SMONs is mainly $O_2^-$ ions. When the sensor is exposed to the target gases, the gas molecules are absorbed on the surface of SMONs, and then react with these chemisorbed oxygen ions.

Ec: bottom of conduction band; Ev: top of valence band; EFn: bulk Fermi level;
EFs: surface Fermi level; Δφ: potential barrier;
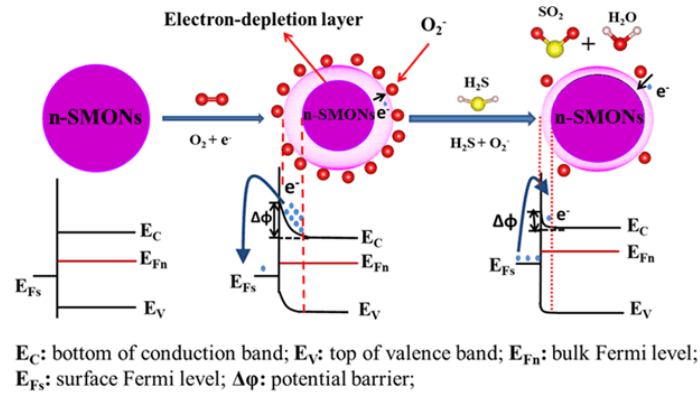
Fig. 3. Schematic diagram of sensing mechanism of n-type semiconducting metal oxide nanostructures for reducing gas of $H_2S$

If the target gases are reducing gases, such as $H_2S$, $H_2$, $NH_3$, HCHO, or $C_2H_5OH$, the chemical reaction releases electrons, which are reinjected back to the electron depletion layer (see Fig. 3, the schematic diagram for $H_2S$ gas sensing mechanism). This results in the reduction of the electron depletion layer and reduces the potential barrier energy ($\Delta\phi$). As a result, the surface resistance of SMONs is decreased. On the contrary, if the target gases are oxidizing gases, such as NO, $NO_2$, $Cl_2$ and $O_3$, the reaction with the chemisorbed oxygen ions will capture the electrons, which will widen the electron depletion layer, resulting in an increase of the potential barrier energy ($\Delta\phi$). Accordingly, the surface resistance of the SMONs is increased.

There are generally three definitions for the response values of n-type SMON based gas sensor, which are Ra/Rg, (Ra-Rg)/Rg and ((Ra-Rg)/Rg)×100% for the target reducing gases, respectively (where Rg and Ra are the resistance of sensors in the target gas and air, respectively). Whereas for the oxidizing gases, Ra and Rg need to be inter-changed in the above three definitions [196]. The time from the injection of the targeting gas to the time of reaching the 90% of the final response is defined as the response time, and the time from the extraction of the gas to the time of reaching 10% of the final response is defined as the recovery time.

Generally, formation of chemisorbed oxygen ions determines the sensing performance. However, the gas sensing mechanism is sometimes attributed to the formation of new compounds as a result of reactions between the target gas and the

surface of the SMONs. For example, $H_2S$ gas molecules can react with ZnO to form ZnS at RT [71, 109]. Formation of such type of conductive metal sulfide significantly decreases the resistance of the SMON-based sensors, which accounts for high sensitivities of n-type SMONs-based sensors for $H_2S$.

Chemical and electronic sensitization of the SMONs can be realized by adding noble metals on their surface and thus can remarkably enhance their sensing properties. Surface modifications and introduction of defects on the surfaces and interfaces such as introduction of heterojunctions [134] and vacancies [117] influence the sensing perfo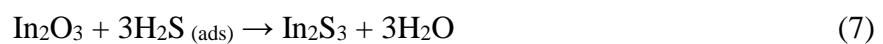rmance of SMONs sensing materials. Addition of carbon nanomaterials on the surface of SMONs can also significantly improve their conductivity and enhance their RT sensitivities at RT [135]. In addition, the alkaline center [129] and hydroxide radicals [198] on the surfaces of SMONs have also been reported to affect the sensing properties, which will be discussed further.

### 2.1.2   Room temperature hydrogen sulfide sensors

N-type SMONs based on ZnO [152], $In_2O_3$ [199], $CeO_2$ [86] and $Fe_2O_3$ [80] have frequently been reported for $H_2S$ gas sensing at RT. Among these, ZnO and $In_2O_3$ are wide band-gap semiconductors, with their band gaps of 3.3 eV and 3.6 eV, respectively. They are very effective for $H_2S$ sensing because $H_2S$ molecules can be easily decomposed and react with the chemisorbed oxygen species on the surface of these sensing material duo to the small bond energy of H-S-H. On the surface of ZnO or $In_2O_3$, the $H_2S$ molecules not only react with the oxide ions of $O_2^-$ to form $SO_2$ and $H_2O$, but also react with ZnO or $In_2O_3$ to form ZnS or $In_2S_3$, based on the following reactions [71, 101, 109]:

$$2H_2S_{(g)} + O_2^-{}_{(ads)} \leftrightarrow 2H_2O_{(g)} + 2SO_2{}_{(g)} + 3e^- \tag{5}$$

$$ZnO + H_2S_{(ads)} \rightarrow ZnS + H_2O \tag{6}$$

$$In_2O_3 + 3H_2S_{(ads)} \rightarrow In_2S_3 + 3H_2O \tag{7}$$
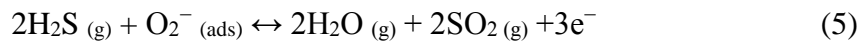
The reactions with the oxide ions increase electron concentrations on the surface of ZnO or $In_2O_3$, which lead to a significant decrease in resistance. Because the ZnS and $In_2S_3$ are metallic conductors, the formation of ZnS or $In_2S_3$ also decreases the resistance of sensors, thus the responses to the gases are enhanced significantly at RT.

Formation of ZnS or In$_2$S$_3$ is an exothermic process and spontaneously occurs at RT, so the sensors based on ZnO or In$_2$O$_3$ nanostructures are very suitable to detect H$_2$S at RT. Due to the formation of these metal sulfides, which are not reactive to most of other gases, such as NH$_3$, H$_2$, NO$_2$, CO, CH$_4$, C$_2$H$_5$OH, HCHO, the selectivity of RT sensors made of the nanostructured ZnO or In$_2$O$_3$ to H$_2$S is excellent. Therefore, the ZnO and In$_2$O$_3$ nanostructured gas sensors generally have high response and excellent selectivity for the H$_2$S gas sensing.

Reaction of metal sulfides in sensing process and the transformation of metal sulfides back to metal oxides in the recovery process are sometimes very slow at RT. Therefore, for the RT H$_2$S gas sensors, the response time and especially the recovery time are often relatively long, sometimes as long as several hours [71, 109]. Furthermore, the sensors may not fully recover at RT [101]. The sensor is often needed to heat to a relatively higher temperature (e.g. 200 °C to 300 °C) in the recovery process for a complete recovery or shortening of the recovery time down to minute-scales [109].
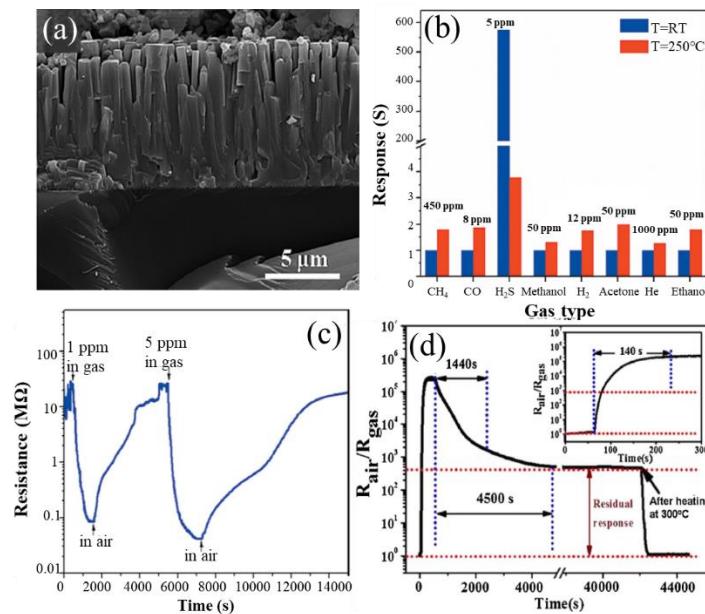


Fig. 4. (a) Cross-section SEM image of vertically aligned ZnO rods; (b) selectivity of the sensor at 25°C and 250 °C; (c) response/recovery curves to 1 and 5 ppm H$_2$S at room temperature. [71], © 2015 Elsevier. (d) The response/recovery curve at 50 ppm H$_2$S gas at room temperature. [101], © 2017 Elsevier.

Hosseinia *et al.* [71] prepared vertically aligned ZnO rods with a diameter of 300-500 nm and a length of 1-9.5 μm using a vapor phase transport method. The nanorods are grown along the c-axis or (0002) planes perpendicularly to the substrate surface as shown in Fig. 4a. The porous network of vertically aligned ZnO rods forms directional channels, which facilitates the mobility of gas molecules. As shown in Fig. 4b, the sensor based on the vertically aligned ZnO rods shows much higher response to $H_2S$ at 26 °C than that at 250 °C, and its response value for $H_2S$ at RT is almost 600 times larger than those for other gases, such as $CH_4$, CO, $H_2S$, methanol, ethanol, acetone, $H_2$ and He. Whereas at 250 °C, it is less than twice of the original value. The response and recovery times of this sensor are very long, which are 320 s and 3592 s for 1 ppm $H_2S$ as shown in Fig. 4c. ZnO nanorods were also grown using a hydrothermal method with the diameters of 70-110 nm and length of 0.2-1.3μm and then used for $H_2S$ sensing [109]. These sensors exhibit a high response (about 35 to 1 ppm $H_2S$) and a very low LOD (50 ppb). However, its response time is longer than 20 min, and the sensor is difficult to be recovered at RT. Response and recovery rates of RT $H_2S$ gas sensors can be improved using dendritic ZnO nanostructures prepared using a vapor-phase transport method with Cu as catalyst at 930 °C [153]. The multilevel branches of ZnO have well-oriented nanorods with diameters of 60 to 800 nm. The response/recovery times are 20/50 s, which make this sensor the fastest SMON-based $H_2S$ sensor at RT reported so far. The sensor exhibits a high response of 26.4 to 500 ppm $H_2S$ and a good selectivity against various gases including $H_2S$, $NH_3$, $H_2$ and $NO_2$ in dry air at RT. The large degree modulation of the contact energy barriers due to the $H_2S$ gas in ZnO dendrites is the key reason for their excellent sensing performance at RT.

Nanostructured $In_2O_3$ is another widely studied material for $H_2S$ sensing. Apart from reactions of $H_2S$ gas with oxygen ions on the surface of $In_2O_3$, the formation of $In_2S_3$ is another key factor for the sensor's high response at RT. Remarkably, the response value of the $In_2O_3$ nanostructure can reach to 240000 for 50 ppm of $H_2S$ at RT [101] as shown in Fig. 4d. The micro/nanostructured porous $In_2O_3$ film was synthesized onto an $Al_2O_3$ ceramic tube using a self-assembly method [101], which has an ordered porous structure with a thickness of 200 nm. Although the sensor does not fully recover to its baseline

at RT, it can be rapidly and completely recovered at 300 ºC. Using a conventional electrospinning process, Duan *et al.* [100] prepared $In_2O_3$ thick walled toruloid nanotubes. Owing to their larger surface areas, the nanotubes have more active sites among them, which results in enhanced responses to $H_2S$ gas. The sensors based on the $In_2O_3$ nanotubes exhibit high response values of 320.14 to 50 ppm $H_2S$ and fast response/recovery times of 45/127 s at the RT. In addition, a good selectivity and a very low LOD with a value of 100 ppb have been demonstrated [100]. Porous $In_2O_3$ nanotubes with a cubic phase have been prepared using the electrospinning method [161], and a high response value of 166.6 to 20 ppm $H_2S$ has been demonstrated. However, the response/recovery times are quite long (287/636 s).

Other n-type SMONs such as $\alpha$-$Fe_2O_3$ [80] and $CeO_2$ [86] have also been reported as good sensing materials for $H_2S$ sensing at RT. For example, porous $\alpha$-$Fe_2O_3$ nanoparticles with a diameter of 34 nm and pore sizes from 2 nm to 10 nm were obtained after annealing a FeOOH nanoparticles precursor [80]. The sensor based on these porous $\alpha$-$Fe_2O_3$ nanoparticles exhibits a high sensitivity (38.4 for 100 ppm $H_2S$) with a low LOD (50 ppb). In addition, it has a good selectivity to $H_2S$ against the other gases (e.g., $C_2H_5OH$, CO, $H_2$ and $NH_3$) and shows a good reproducibility. The response time is fast with a value of 180 s. However, the recovery time is very long with a value of 3750 s for 100 ppm $H_2S$. $CeO_2$ nanowires [86] were also synthesized using a facile hydrothermal process and they show fast response/recovery times with values of 24/15 s for 50 ppb $H_2S$.

For the $\alpha$-$Fe_2O_3$ and $CeO_2$ nanostructure-based $H_2S$ gas sensors, the main sensing mechanism is the interactions of the $H_2S$ molecules with the oxygen ions on its surface. Accordingly, the sensing is much faster than those sensors based on ZnO and $In_2O_3$, although their response to $H_2S$ is much lower [80, 86].

### 2.1.3 Room temperature nitrogen dioxide sensors

Various SMONs based gas sensors have demonstrated excellent sensing performance at RT for $NO_2$ gas sensing, using different materials such as ZnO [110, 200, 201], $SnO_2$ [76], $In_2O_3$ [196] and $WO_3$ [202-206], $Sb_2O_5$ [207], $Bi_2O_3$ [208] etc. The sensing mechanism

of SMONs to the $NO_2$ is based on the formation of $NO_2^-$ by capturing electrons and the reaction between $NO_2$ gas molecules and $O_2^-$ ions on the surface of the SMONs. All these reactions extract electrons from the surface of the SMONs, thus resulting an increase in the resistance of these sensors, based on the following reactions [209]:

$$NO_2 \text{ (gas)} + e^- \leftrightarrow NO_2^- \text{ (ads)} \tag{8}$$

$$NO_2^- \text{ (ads)} + O_2^- \text{ (ads)} + 2e^- \leftrightarrow NO \text{ (gas)} + 2O^{2-} \text{ (ads)} \tag{9}$$
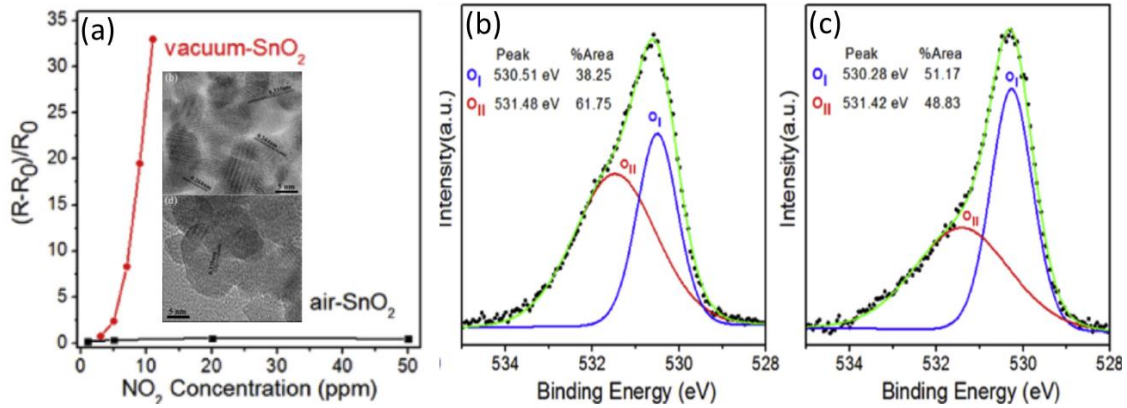


Fig. 5. (a) Response of vacuum-annealed $SnO_2$ compared to air-annealed $SnO_2$ nanocrystals to different concentrations of $NO_2$ at room temperature, the inset shows the TEM images of two types of nanocrystals; (b) and (c) deconvolution of the O 1s peaks of X-ray photoelectron spectroscopy (XPS) for vacuum-$SnO_2$ and air-$SnO_2$ (the peaks with red color belong to adsorbed O ions). [76], 2016 Elsevier.

One of the outstanding features of SMON-based RT $NO_2$ gas sensors is their fast response speeds due to the strong oxidation of $NO_2$ molecules. Kodu *et al.* [157] reported $NO_2$ sensors based on granular $SnO_2$ thin film with a thickness of ~90 nm deposited using a pulsed laser deposition method. The sensor exhibits not only a remarkably high response value of 7730 to 4 ppm $NO_2$, but also a very fast response time of 3 s at RT. Wei *et al.* [76] prepared $SnO_2$ nanocrystals by annealing the $Sn(OH)_4$ precursor powders at 550 °C in both vacuum and ambient air environments, respectively. The vacuum-annealed $SnO_2$ and air-annealed $SnO_2$ nanocrystals have different particle diameters of 7.2 nm and 10.3 nm as shown in Fig. 5a. The response value of the vacuum-annealed $SnO_2$ sensor at RT is ~2.4 to 5 ppm of $NO_2$, which is higher than that of air-annealed $SnO_2$ (~0.35). This is mainly because the increased oxygen vacancies on the surface of

the vacuum-annealed $SnO_2$ are much more than those on the air-annealed $SnO_2$ nanocrystals, which can be identified by X-ray photoelectron spectroscopy (XPS) analysis as shown in Figs. 5b and 5c.

Yu *et al.* [91] prepared ZnO nanowalls with uniformly distributed and cross-linked nanowalls of ~20 nm using a solution method. The cross-linked nanowalls have a porous structure with pore sizes from 200 nm to 500 nm. The sensor exhibits a high response value (6.4) and fast response/recovery times (23/11 s) towards 50 ppm $NO_2$ at RT with a good repeatability. Based on the analysis from fluorescence emission spectrum, it was identified [82] that the key factors for effective $NO_2$ sensing are: (1) the presence of oxygen vacancies in the ZnO nanowall nanostructures, and (2) a delicate balance between oxygen vacancies defects and porosity.

$TiO_2$ and $In_2O_3$ are two other frequently reported nanomaterials for $NO_2$ sensing. Tshabalala *et al.* [79] prepared $TiO_2$ nanoparticles with an average particle size of 6.5 nm using a hydrothermal method. The fluffy and porous $TiO_2$ layer has a pore volume of 0.4170 $cm^3$/g and a large surface areas of 80.3 $m^2$/g [79]. The porous nanostructures, high concentration of oxygen vacancies and the interstitial defect states on the surface are crucial for the efficient adsorption and desorption of $NO_2$ gas molecules. Therefore, the sensor made of these nanostructures exhibits a high response (1093 to 40 ppm $NO_2$), fast response/recovery times of 48/52 s and a low LOD of 0.02 ppm at RT. However, the selectivity of this sensor is poor with its relatively high responses to many other gases such as $H_2$, $NH_3$ and $CH_4$. $In_2O_3$ octahedrons have also been prepared using the sol-gel technique for $NO_2$ sensing [102], and the sensor using these $In_2O_3$ octahedrons has a response value of 63 to 200 ppm $NO_2$ at RT, with a good selectivity to $NO_2$ against CO, $H_2$ and $NH_3$.

### 2.1.4   Room temperature ammonia sensors

The sensing mechanism of SMON-based ammonia gas sensors operated at RT is also based on the reactions between $NH_3$ gas molecules and adsorbed $O_2^-$ ions on the surfaces of the SMONs as shown in the following reactions [92, 183]:

$$NH_{3\,(gas)} \rightarrow NH_{3\,(ads)} \tag{10}$$

$$4NH_{3\,(ads)} + 3O_2^- \rightarrow 2N_2 + 6H_2O + 3e^- \qquad (11)$$
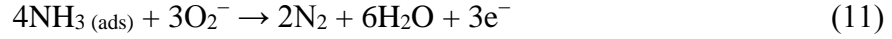
Majority of the single phase n-type SMONs without modifications by other elements can be used for $NH_3$ gas sensors, including ZnO [210-212], $In_2O_3$ [111], $SnO_2$ [213], $SnS_2$ [214], $MoO_3$ [215], $WO_3$ [216] and $TiO_2$ [217]. They have good RT performance for $NH_3$ sensing with high response and fast response/recovery. Among these, the sensors based on $In_2O_3$ and $TiO_2$ exhibit ultra-high responses and response/recovery times. For example, a RT sensor based on $TiO_2$ nanoparticles has an ultra-high response of 10080.8 to 100 ppm of $NH_3$ and fast response/recovery times of 35.5/59 s [78].
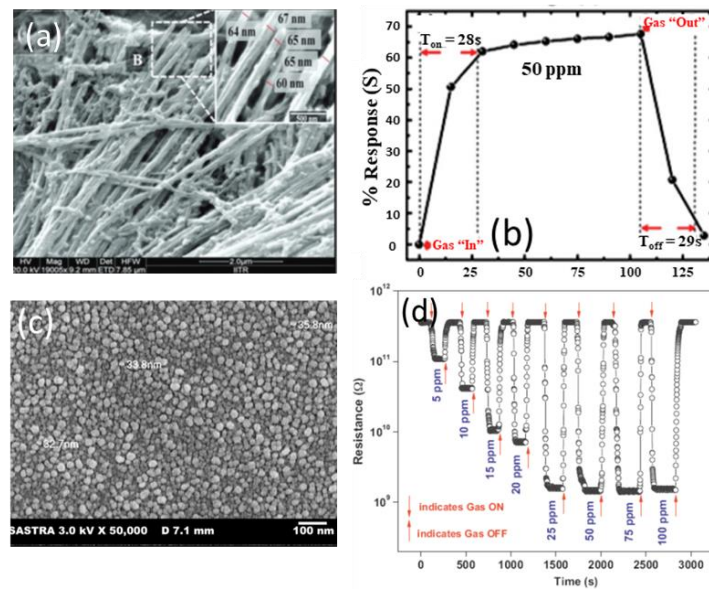


Fig. 6. (a) SEM images of ZnO nanowire array; (b) response/recovery curves of the ZnO nanowire array for 50 ppm $NH_3$ [83], © 2014 The Royal Society of Chemistry. (c) SEM image of nanostructured ZnO thin films on glass substrates; (d) response/recovery curves of the nanostructured ZnO thin film-based sensor for $NH_3$[182], 2013 Elsevier.

Du *et al.* [111] reported a RT $NH_3$ gas sensor using porous $In_2O_3$ nanotubes. This gas sensor exhibits an ultra-high response value of 2500 and a good reproducibility with response and recovery times less than 20 s, both of which are better than those of the sensors made of $In_2O_3$ nanowires or nanoparticles. The performance enhancement is attributed to the porous structure and ultra-high surface-to-volume ratio of the porous $In_2O_3$ nanotubes, which can adsorb more oxygen molecules. Another gas sensor made

of TiO$_2$ films prepared using a reactive magnetron sputter method also exhibits an excellent response with a value of 7857 to 100 ppm of NH$_3$, fast response/recovery times of 34/90 s and a low LOD of ~5 ppm [174]. Kumar *et al.* [83] used an anodic aluminum oxide template route to prepare highly ordered ZnO nanowire arrays as the sensing layer for detection of NH$_3$. The diameters of these nanowires are in the range of 60 to 70 nm and their length is about 11 μm as shown in Fig. 6a. At the RT, the sensor exhibits 68% of response value (defined as ($\Delta$R/Rg)$\times$100%) to 50 ppm NH$_3$ and fast response/recovery times (28/29 s) (see Fig. 6b) [83]. Another NH$_3$ sensor made of nanostructured ZnO thin films [112] synthesized using a magnetron sputtering technique shows a high response with a value of 304 to 100 ppm NH$_3$ with response/recovery times of 92/113 s.

Mani *et al.* [182] reported a sensor made of a nanostructured ZnO thin film (shown in Fig. 6c) using a spray pyrolysis technique. As shown in Fig. 6d, the sensor using this thin film exhibits a high response with a value of 233 to 25 ppm of NH$_3$ at RT, and fast response and recovery times of 20/25 s. It has a good selectivity to ammonia gas against other VOC gases (i.e. ethanol, methanol, benzyl alcohol, 2-propanol and acetone). Moreover, the sensor is insensitive to relative humidity. However, the sensor becomes saturated when the concentration of NH$_3$ is above 20 ppm, indicating that the LOD is about from 5 ppm to 25 ppm. In brief, high response, fast response/recovery, and superior LOD have been achieved for the n-type SMON-based RT NH$_3$ gas sensors.

### 2.1.5   Room temperature ethanol sensors

Most n-type SMONs made of ZnO [218-220], Fe$_2$O$_3$ [221], SnO$_2$ [222], In$_2$O$_3$ [105], TeO$_2$ [85] and WO$_3$ [106] can be used for ethanol sensing. The sensing mechanism of n-type SMON-based ethanol gas sensors is based on the interaction of ethanol gas molecules with chemisorbed O$_2^-$ ions on the surfaces of the SMONs. The ethanol molecules react with the adsorbed oxygen ions to form CO$_2$ and H$_2$O. Subsequently, electrons are released thus resulting in an increase in electron density and a decrease in potential barrier energy. These can be expressed using the following reactions [180]:

$$CH_3CH_2OH_{(gas)} \rightarrow CH_3CH_2OH_{(ads)} \qquad (12)$$

$$C_2H_5OH + 3O_2{}^-{}_{(ads)} \rightarrow 2CO_2 + 3H_2O + 3e^- \qquad (13)$$
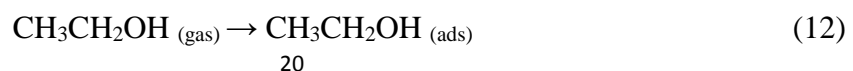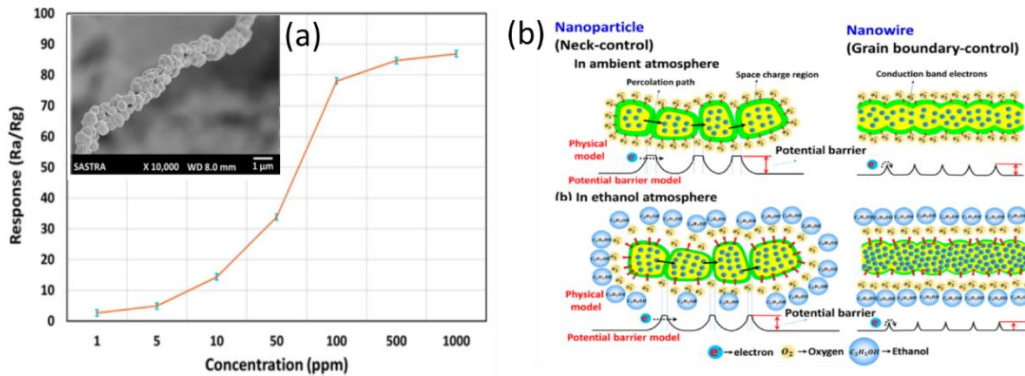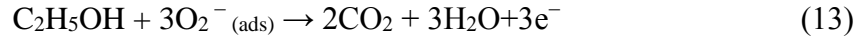


Fig. 7. (a) Responses of the ZnO nanowire sensor to different concentrations of ethanol at room temperature, the inset shows the SEM image of ZnO nanowire; (b) the schematic diagram of ethanol sensing mechanism. [82], © 2017 American Chemical Society.

The RT ethanol gas sensors based on the n-type SMONs usually exhibit rapid response and recovery. For example, a sensor based on In$_2$O$_3$ cubic crystals [105] prepared using a hydrothermal method exhibits very fast response/recovery (3/5 s). However, the response is poor with a value of only 1.4 to 100 ppm ethanol vapors. The fast response/recovery times together with high responses have been reported for the sensor made of ZnO nanowires [82, 180]. Shankar *et al.* [82] reported an ethanol sensor made of ZnO nanowires (see Fig. 7a) prepared using the electrospinning. The self-assembled ZnO nanowires with two different molecular weights of poly(vinyl alcohol) (PVA), e.g., 14000 and 140000 g/mol, were prepared using an electrospinning technique, and then heat-treated to transform them into ZnO nanospheres and nanowires at a temperature of 600 °C. These nanostructures have a good selectivity to ethanol compared to other VOCs including ethanol, methanol, acetaldehyde, and acetone when operated at RT. The nanowires based sensors have a higher ethanol response (78 to 100 ppm) than those based on the nanoparticles (about 48 to 100 ppm) [76]. The nanowire-based ones also show fast response/recovery times of 9/12 s. Furthermore, the nanowire-based sensor has an excellent repeatability.

Fig. 7b shows a schematic diagram of ethanol sensing mechanism for the ZnO-based sensor [82]. The chemisorption of oxygen molecules on the sensor surface results in the

formation of a space charge region on the surface of ZnO, which can act as a barrier for electron transports in the ZnO sensing layer [82]. Due to the formation of double-spaced charge layers from the intergranular contacts of nanoparticles, the potential barrier energy is increased, which results in the broadening of the percolation path and hinders the electron transport. This further influences the adsorption−desorption rate and the sensing properties to ethanol. However, the intergranular contact resistance will be reduced in the ZnO nanowires, which decreases the potential barrier energy, thus enhancing the sensing performance.

Similarly, $TiO_2$ nanotubes [96] prepared using an electrochemical anodization method and $TeO_2$ nanowires [85] prepared using thermal evaporation also show good responses to ethanol [85, 96]. However, the selectivity is poor as they are also sensitive to methanol and propanol.

### 2.1.6   Room temperature hydrogen sensors
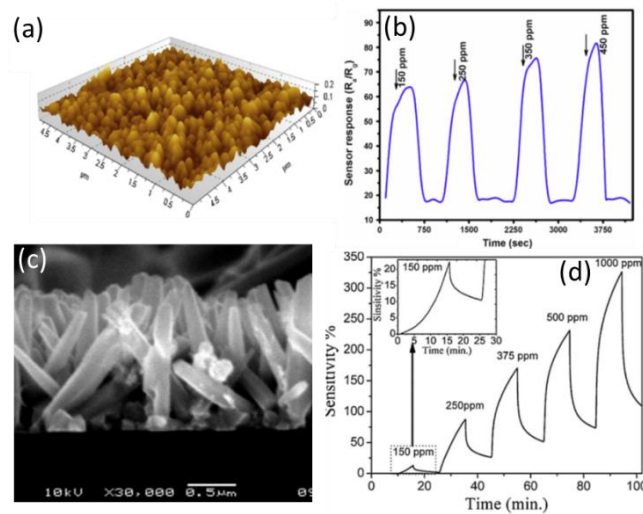


Fig. 8. (a) AFM image of the ZnO films and (b) response/recovery curves of ZnO film-based gas sensor to different concentrations of $H_2$. [189], © 2014 Springer Nature. (c) Cross section SEM image of the ZnO nanorods and (d) response/recovery curves of ZnO nanorod-based gas sensor to different concentrations of $H_2$. [191], © 2013 Elsevier.

Hydrogen gas is one of the extremely flammable and explosive gases. Therefore,

detection of traces of hydrogen gas using the RT gas sensors is critical to avoid the dangers of explosion. For this application, the sensors must be fast, highly sensitive and selective. In particular, the fast response is paramount for a timely detection of a possible hydrogen leakage. As summarized in Table 1, the SMONs made of ZnO [188, 189], $MoO_3$ [192] and $SnO_2$ [193] have been demonstrated for hydrogen sensing at RT using various nanostructures including nanofilm [189], nanowires [108], nanotubes [188] and nanorods [190, 191]. The sensing mechanism is based on the reaction of $H_2$ molecules with chemisorbed $O_2^-$ ions on the surface of the SMONs, as shown in the following chemical equation [189]:

$$2H_2 + O_2^-\,_{(ads)} \rightarrow 2H_2O + e^- \tag{14}$$

From the literature, sensors made from ZnO films [189] and ZnO nanorods [191] show high responses to $H_2$, but long response/recovery times (see Fig. 8).
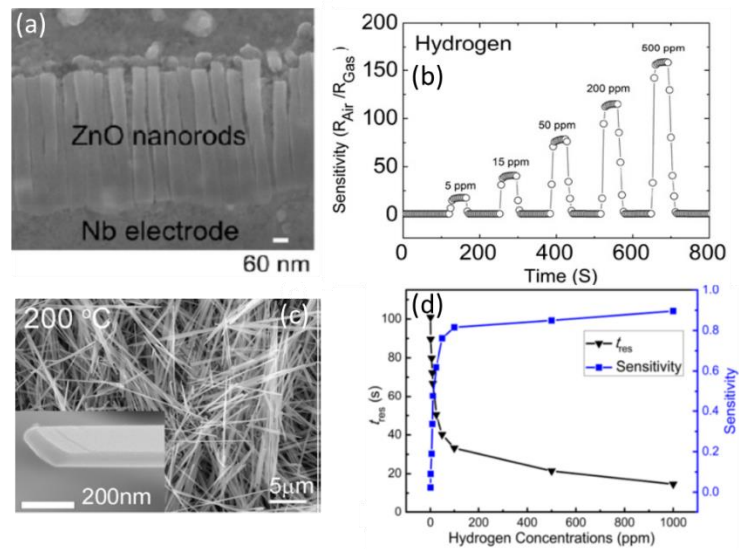


Fig. 9. (a) TEM image of vertical ZnO nanorods; (b) Response/recovery curves of vertical ZnO nanorods-based gas sensor versus different concentrations of $H_2$. [190], © 2012 Elsevier. (c) SEM images of α-$MoO_3$ nanoribbons; (d) response values and times of α-$MoO_3$ nanoribbons-based gas sensor versus different concentrations of $H_2$. [192], © 2015 American Chemical Society.

Using anodized aluminum oxides as nano-templates, Lim et al. [190] synthesized vertical ZnO nanorods (see Fig. 9a) using atomic layer deposition, and a highly

sensitive and fast response/recovery $H_2$ gas sensor was fabricated using these vertical ZnO nanorods. A response value of 162 for 500 ppm $H_2$ and a response time of 30 s were demonstrated (see Fig. 9b) [193]. A faster response $H_2$ gas sensor was also reported using [001]-oriented α-$MoO_3$ nanoribbons (see Fig. 9c) [192] with a response time of 14.1 s for 1000 ppm of $H_2$ and a low LOD of 500 ppb (see Fig. 9d) [192]. It has a good reproducibility and a high selectivity against ethanol, CO and acetone.

In brief, the RT gas sensor based the n-type SMONs can detect most type of hazardous gases, with advantages such as easy preparation, low cost, simple post-treatment and good stability of structure. Various morphologies of nanostructures for the n-type SMONs have been synthesized and used into the gas sensors operated at the RT. These sensors have been widely used to detect various gases and some good sensing properties have been achieved. However, it should be addressed that for most of these n-type SMON-based RT gas sensors, their sensitivity at RT is much lower than that at a higher working temperatures. Their responses and recovery times are quite long, and sometimes these sensors cannot be fully recovered at RT. In addition, at RT, the sensing performance is seriously affected by various environmental factors, such as humidity and external light source. To enhance their sensing properties at RT, modification of these n-type SMONs should be adopted, which will be discussed in Section 3.

### 2.2    P-type semiconducting metal oxide nanostructures and gas sensors

Up to now, the major p-type SMONs used in RT gas sensing are CuO [223-225], $Co_3O_4$ [92, 103] and NiO [94, 226], and the main target gases include $NH_3$ [98, 103], $H_2S$ [224, 225] and $NO_2$ [226], as listed in Table 2. Apart from the sensing mechanism which is based on the reaction of target gases with the oxygen ions on the surface of SMONs, the formation of metal sulfides is another key reason for $H_2S$ sensing, especially for CuO nanostructures [93, 225].

Table 2 Summary of room temperature sensing properties of p-type semiconducting metal oxide nanostructures

| Material | Structure | Synthesis method | Target gas | C (ppm) | Response | $t_{res}/t_{rec}$ | LOD | Ref. |
|---|---|---|---|---|---|---|---|---|
| CuO | Nanosheets | Hydrothermal | $H_2S$ | 0.01 | 1.25 | 234/76 s | 10 ppb | [93] |
| CuO | Thin films | Thermal evaporation | $H_2S$ | 5 | ~250[#] | 60/90 s | 100 ppb | [224] |
| CuO | Flower | Hydrothermal | $H_2S$ | 1 | 2.1 | 240/1341 s | 0.1 ppm | [225] |
| CuO | Tube | Biotemplate | $H_2S$ | 5 | ~41 | 29/41 s | 2 ppb | [98] |
| CuO | Nanofibers | Electrospinning | $H_2S$ | 100 | 2.23 | 4.3/- s | 1 ppm | [227] |
| CuO | Nanoparticles | Sol-gel-combustion | $NH_3$ | 100 | 9.83[*] | ~150/~500 s | - | [81] |
| CuO | Nanoparticles | Sol–gel-combustion | $NH_3$ | 100 | 0.99[*] | 30/- s | - | [228] |
| CuO | Nanorectangles | Hydrothermal | $NH_3$ | 5 | ~0.25[*] | 90/120 s | 5 ppm | [223] |
| CuO | Microspheres | Reflux method | $NO_x$ | 97 | 64.93[#] | 5.33 /- s | 0.97 ppm | [90] |
| CuO | Nanoplatelets | Sonochemical method | $NO_2$ | 40 | 53737 | - | - | [229] |
| $Cu_xO$ | Virus-like | Chemical solution | $NO_2$ | 4 | 28.1 | 22/42 s | 1 ppm | [230] |
| CuO | Nanowires | Thermal oxidation | Ethanol | 100 | 202 | 0.19/0.19 s | ~10 ppm | [36] |
| CuO | Nanoribbons | Wet chemical | Ethanol | 100 | 210[#] | 8/25 s | 20 ppm | [231] |
| NiO | Nanosheets | Hydrothermal | $NO_2$ | 60 | 3.05[*] | ~200/~300 s | ~5 ppm | [94] |
| NiO | Nanosheets | Hydrothermal | $NO_2$ | 60 | 1.8[*] | ~250/~250 s | ~7 ppm | [226] |
| NiO | Nanosheets | Microwave synthesis | $NO_2$ | 10 | 0.56 | - | - | [232] |
| NiO | Dendritic-like | Electrolytic | $NH_3$ | 30 | 19[#] | 40/1500 s | - | [233] |
| $Co_3O_4$ | Nanosheets | Hydrothermal | $NH_3$ | 100 | 9.5 | 9/134 s | 0.2 ppm | [92] |
| $Co_3O_4$ | Porous structure | Template | $NH_3$ | 100 | 146[#] | 2/- s | 0.5 ppm | [103] |
| $Co_3O_4$ | Nanoparticles | Thermal treatment | $NO_x$ | 100 | 52.1[#] | - | 100 ppb | [234] |
| $Co_3O_4$ | Nanosheets | Hydrothermal | CO | 50 | - | 15/ 20s | - | [235] |
| $Cr_2O_3$ | Nanospheres | Hydrothermal | Ethanol | 40 | 9* | - | 5 ppm | [236] |
| $Cr_2O_3$ | Mesoporous | Impregnation | Ethanol | 1000 | 13.0 | - | 10 ppm | [237] |
| $\beta$-$MnO_2$ | Thin films | Spray pyrolysis | $CH_3COH$ | 10 | 89[#] | 60/11 s | 10 ppm | [238] |
| $MnO_2$ | Nanofibers | Chemical solution | $NH_3$ | 100 | 20[#] | - | 1 ppm | [239] |
| $\alpha$-$MnO_2$ | Nanospheres | Self-assembly | $NH_3$ | 20000 | 0.2 | - | - | [240] |

*Notes:*

*C = concentration;*

*$t_{res}/t_{rec}$ = response time /recovery time;*

*LOD = limit of detection;*

*Response is defined as Ra/Rg (for reducing gases) or Rg/Ra (for oxidizing gases), Ra: resistance of the sensor exposed to reference, Rg: resistance of the sensor exposed to*

*target:*
*\* Here the response is defined as ΔR/Rg (for reducing gases) or ΔR/Ra (for oxidizing gases), ΔR: the change in resistance.*
*# Here the response is defined as (ΔR/Rg)×100% (for reducing gases) or (ΔR/Ra)×100% (for oxidizing gases).*

### 2.2.1 Gas sensing mechanisms



$E_C$: bottom of conduction band; $E_V$: top of valence band; $E_{Fn}$: bulk Fermi level;
$E_{Fs}$: surface Fermi level; $\Delta\varphi$: potential barrier;
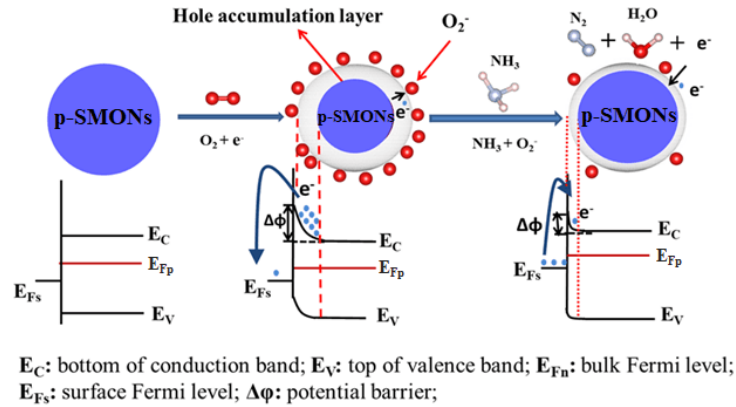
Fig. 10. Schematic diagram of sensing mechanism for p-type semiconducting metal oxide nanostructures to reducing gas of $NH_3$.

Generally, the sensing mechanism of p-type SMONs is based on the changes of surface resistance as a result of the changes in the concentrations of hole carriers due to their redox reaction with the target gases. When exposed to air at RT, the oxygen ions of $O_2^-$ are formed from the adsorbed oxygen molecules on the surface of p-type semiconductor and they capture electrons from the conduction band of the SMONs. The density of hole carriers is increased, thus resulting in the decrease in the surface layer's Fermi level. Due to an accumulated hole layer formed on the surface of p-type SMONs, the conductivity will be increased and the resistance of the sensors is decreased. This is opposite to the sensing mechanism for the n-type SMONs sensors discussed in the last section.

The sensing mechanism of the p-types SMONs to the reducing gas of $NH_3$ is schematically shown in Fig. 10. When the reducing gas molecules (such as $NH_3$) are adsorbed on the surface of SMONs, the reaction between the $NH_3$ and $O_2^-$ ions will release electrons, which will combine with the holes, resulting in an increase in the Fermi level and reduction of the holes accumulation layer. Consequently, the

26

conductivity of the SMON layer is decreased. However, for the oxidizing gases, more free electrons are captured from the surface of the p-type SMONs. For example, the $NO_2$ molecules adsorbed on the sensor surface can capture electrons from the p-type SMONs to form $NO_2^-$ as listed in the reaction equation (8). This significantly increases the concentrations of holes carriers, thus resulting the increase in conductivity of the p-type SMONs-based gas sensors. In summary, the resistance of p-type SMONs based sensors will be increased in the presence of the reducing gases, whereas their resistance will be decreased in the presence of the oxidizing gases.

### 2.2.2   Room temperature hydrogen sulfide sensors

At present, the dominant p-type SMONs for RT $H_2S$ gas sensors is CuO, which exhibits excellent sensing performance when operated at RT, especially with the high sensitivity and fast response and recovery. Different from the sensing mechanisms discussed above which are based on the reactions between the target gases with the oxygen ions, the formation of CuS is highly responsible to the sensing response to $H_2S$ at RT.
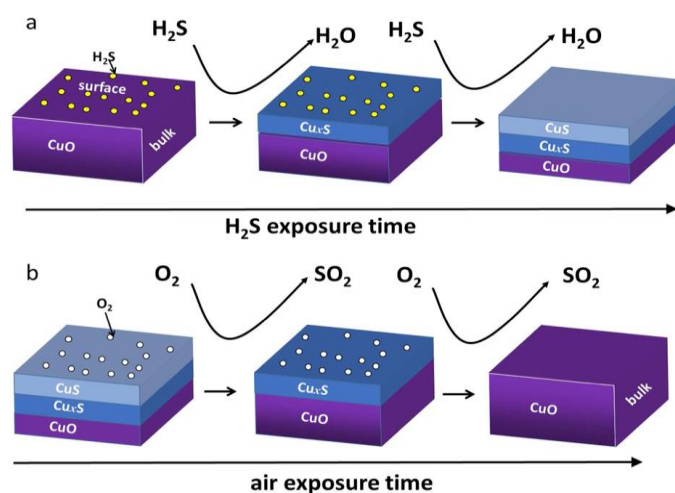


Fig. 11. Schematic diagrams of sensing mechanism of CuO: (a) response process in $H_2S$ and (b) recovery process in air. [93], ©2016 American Chemical Society.

Fig. 11 shows schematic diagrams of the sensing mechanism for CuO-based $H_2S$ sensor. $H_2S$ molecules can react with CuO to form CuS on the surface at RT, based on the following reactions [93, 225],

$$H_2S_{(g)} + CuO_{(s)} \rightarrow CuS_{(s)} + H_2O_{(g)} \tag{15}$$

$$CuS_{(s)} + O_{2\,(g)} \rightarrow CuO_{(s)} + SO_{2\,(g)} \tag{16}$$
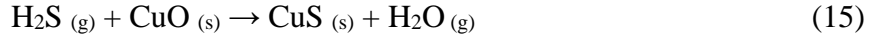
The CuS is a metallic-like conductor. Formation of CuS on the SMON's surface which will dramatically decrease the resistance of the sensor. Consequently, although the $H_2S$ is a reducing gas, the response of the sensors exhibits a decrease in resistance. The RT $H_2S$ gas sensors are highly selective owing to this unique interaction between the $H_2S$ and CuO. However, their recovery times are relatively long at the RT due to the requirement for the transformation from CuS to CuO.
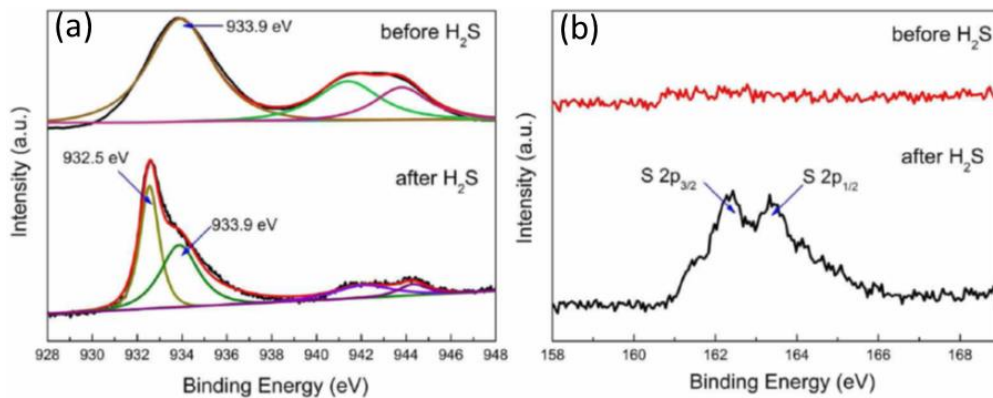


Fig. 12. (a) Cu $2p_{3/2}$ and (b) S 2p XPS spectra of porous CuO nanosheets before and after exposure to $H_2S$. [93], © 2016 American Chemical Society.

This $H_2S$ sensing mechanism has been proved from different studies. For example, Li *et al.* [93] reported a $H_2S$ sensor based on porous CuO nanosheets with a thickness about 60 nm on alumina tubes, prepared using a hydrothermal method. The sensor based on these porous CuO nanosheets has an excellent selectivity to $H_2S$. It exhibits high response values to $H_2S$, but no apparent responses to $NH_3$, CO, NO, $NO_2$, $H_2$, and $C_2H_5OH$ [93]. The sensor has a superior LOD as low as 10 ppb and a good reproducibility at RT. Sensing mechanism based on the transformation from CuO into CuS on the surface of nanosheets has been verified using the XPS analysis. As the XPS spectra shown in Figs. 12, after the CuO is exposed in $H_2S$ gas, a new peak of the Cu $2p_{3/2}$ at 930.8 eV appears which is attributed to CuS, and the S $2p_{3/2}$ and S $2p_{1/2}$ states at 162.3 and 163.4 eV can be identified. Similarly, nanostructures of hierarchically flower-like CuO nanostructures [225] have been prepared, and the sensors made of these

nanostructured CuO exhibit high sensitivity, good reproducibility and high sensing selectivity to $H_2S$ at RT. Zhang *et al.* [98] prepared tube-like CuO nanostructures using pomelo flesh as a bio-template. The unique tube-like CuO nanostructures enhance the diffusion of $H_2S$ molecules and promote the rapid fast formation of CuS. The $H_2S$ sensor based on the tube-like CuO nanostructures has a good selectivity to $H_2S$, compared to gases such as gasoline, formaldehyde, $CH_4$, $H_2$, acetone, CO, toluene, and ethanol. The response/recovery times are lower than 60 s for the $H_2S$ in a wide range of 10 ppb~10 ppm. In addition, the sensor demonstrates a stable detection performance at RT over 3 months.

### 2.2.3 Room temperature ammonia sensors
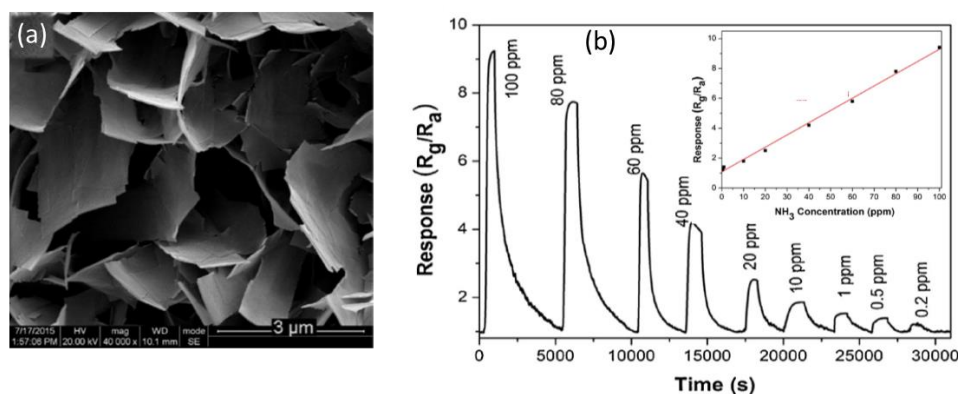


Fig. 13. (a) SEM image of network $Co_3O_4$ nano-sheet arrays; (b) response/recovery curves of the network $Co_3O_4$ nano-sheet arrays based sensor to different concentrations of $H_2S$ at room temperature (the inset shows the response value). [92], © 2016 Elsevier.

The CuO nanostructures are also suitable for $NH_3$ sensing at RT. Sakthivel *et al.* [223] fabricated a flexible $NH_3$ sensor on polyethylene terephthalate substrate using CuO nano-rectangles, which were synthesized using a surfactant-free hydrothermal method. The flexible RT sensor made of the CuO nano-rectangles is effective for sensing ammonia even under different bending conditions as it exhibits identical response and response/recovery times. Furthermore, this flexible $NH_3$ sensor exhibits both good stability and reproducibility in a three-month testing period [223].

$Co_3O_4$ nanostructures [92] have also been found effective for $NH_3$ detection with fast

response speeds at RT. Fig. 13a shows an image of network $Co_3O_4$ nano-sheet arrays deposited on an alumina tube prepared using a hydrothermal method. The average sheet thickness of $Co_3O_4$ nano-sheet is 39.5 nm. $NH_3$ molecules react with the surface chemisorbed $O_2^-$ ions and form $N_2$ and $H_2O$. As shown in Fig. 13b, the response time for the gas sensor is as short as 9 s for 0.2 ppm $NH_3$ at RT. The sensor responds linearly to the concentrations of $NH_3$ within a range between 1 ppm -100 ppm. It also exhibits a good performance in reproducibility, stability and selectivity to $NH_3$ (compared to $H_2$, CO, $H_2S$ and $C_2H_5OH$). 3D hierarchical porous $Co_3O_4$ nanostructures [103] were synthesized by Wu *et al.* using polystyrene spheres as the template. The average particle size is 20 nm and the specific surface area is 58.75 $m^2/g$. The structures have macro-size pores, mesopores and plenty of irregular structural defects. The sensor made of these porous $Co_3O_4$ nanostructures exhibits a sensitivity of 146% (defined as $(\Delta R/Rg)\times100\%$) to 100 ppm $NH_3$, and has a fast response time of 2 s. However, the recovery time is very long, e.g., longer than 1000 s [103].

Apart from CuO and $Co_3O_4$ nanostructures, the NiO [233, 240] and $MnO_2$ [239] were also used to make the RT $NH_3$ gas sensors, although the response was found to be very slow. Applying special nanostructures can improve the responses of the sensors. For example, the hierarchical hollow nanospheres of $\alpha$-$MnO_2$ composed of densely aligned nanowires was reported to exhibit an improved $NH_3$ gas sensing sensitivity, and faster response and recovery than the standard $\alpha$-$MnO_2$ nanowires [240]. Doping with metal ions such as Al doped NiO was also reported as an effective route for improving the sensitivity and responses of the sensor operated at RT [233].

### 2.2.4 Room temperature nitrogen dioxide sensors

P-type nanostructures have also been reported as good RT $NO_2$ sensing materials. When they are exposed in the oxidizing gases, such as $NO_x$, the $NO_x$ molecules are absorbed on the surface and form $NO_x^-$ and holes, and the reactions of $NO_x$ with the chemisorbed oxygen ions also increase the concentration of holes on the surface, which can be revealed from the reaction equations (17) to (19) [234]. These reactions will widen the width of accumulated hole layer on the surface of p-type SMONs, and cause the

increase of conductivity of the sensors.

$$NO_{x\ (gas)} \leftrightarrow NO_x^-{}_{(ads)\,+}\,h^+ \tag{17}$$

$$NO_{(gas)} + O_2^-{}_{(ads)} \leftrightarrow NO_2^-{}_{(ads)} + O^-{}_{(ads)} + h^+ \tag{18}$$

$$NO_{2\ (ads)} + O_2^-{}_{(ads)} \leftrightarrow NO_3^-{}_{(ads)} + 2O^-{}_{(ads)} + h^+ \tag{19}$$
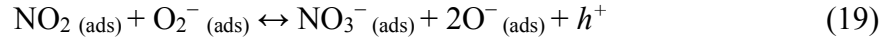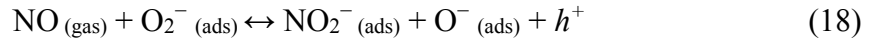
Self-assembled mesoporous $Cu_xO$ virus-like microspheres [230] exhibited a high response of 28.4 and response/recovery times of 22/42 s to 4 ppm $NO_2$ gas measured at RT. The good sensing performance of this special microstructure is attributed to the formation of hierarchical 3D nanostructures, micropores and large surface area for the effective gas diffusion, the abundant surface oxygen vacancies and the heterojunctions at the interfaces between $CuO$ and $Cu_2O$. The RT $NO_2$ gas sensors were also made using unique chain $Co_3O_4$ structures [234] and self-assembled polycrystalline hexagonal $NiO$ nanosheets [226]. Because of the reduced grain boundaries, which minimizes the carriers' scattering at the interfaces during the chemisorption of $NO_2$, these special $Co_3O_4$ nanostructures showed much better responses to the $NO_2$ than those made of the $Co_3O_4$ and $NiO$ nanoparticles.

Apart from detecting $H_2S$, $NH_3$ and $NO_2$, the RT sensors based on the p-type SMONs have also been used for detecting other types of gases. For example, sensor made of $MnO_2$ shows good sensing performance for the acetaldehyde vapor [238], and at the ambient temperature, $\beta$-$MnO_2$ thin film was reported to have good sensing responses and fast response/recovery. The sensitivity was found to be 89% for sensing the 10 ppm acetaldehyde vapor, and the response and recovery times were found to be of 60 s and 11 s, respectively. This sensor has also showed a good selectivity to the acetaldehyde gas, comparing with the other reducing gases such as acetone, benzene, diethylamine, ethanol, dimethylamine, 2-propanol, monomethylamine and ammonia [238]. Sensors made of $Co_3O_4$ nanosheets was also reported to have very fast response and recovery of 15/20 s to 50 ppm CO and $CH_4$ [235].

The p-type $Cr_2O_3$ based gas sensor is normally operated at higher temperatures above 100 °C, and there are few reports about the $Cr_2O_3$ based RT gas sensors. However, 3D cubic mesoporous $Cr_2O_3$ nanostructures were recently prepared and the sensor made of this nanostructure exhibits an enhanced sensitivity for detecting ethanol vapor at room

temperature, which is much better than those of the dense $Cr_2O_3$ film [237]. The response of the 3D cubic mesoporous $Cr_2O_3$ sensor is 13.0 to 1000 ppm ethanol, whereas it is only 2.0 for the dense $Cr_2O_3$ film.

Although there are some reports for using the p-type SMONs in gas sensors operated at high temperature, these are much less compared to those of using n-type SMONs. The sensitivity of p-type SMON sensors is generally not as high as that of the n-type SMON sensors. Modification of the p-type SMONs using noble metal nanoparticles or metal ions is an effective route to further enhance the sensing performance, which will be discussed in the Section 3.

## 3. Room temperature gas sensors based on modified and composite semiconducting metal oxide nanostructures

### 3.1 Metal modified semiconducting metal oxide and gas sensors

#### 3.1.1 Gas sensors based on noble metal modified semiconducting metal oxide nanostructures

Due to their chemical sensitization and electronic sensitization, noble metals have been widely applied for surface modifications of the SMONs, which has become one of the effective routes to improve their sensing performance, especially for the sensors operated at RT [241]. This can be seen form the comparison of room temperature sensing properties between the pristine and noble metal modified SMONs as listed in Table 3. So far, the noble metals used to modify the SMON based gas sensors are mainly Au [242-246], Ag [247, 248], Pt [249, 250] and Pd [251-254]. Nanoparticles of the noble metals of are usually decorated onto surfaces of SMONs using wet-chemical method [116], thermal vaporization [253], sputtering method [255] and electrospinning technology [256]. Many of these sensors have the commonly reported spill-over effect [241], which means that the active centers on the surface of the solid catalyst produce oxygen active species by adsorbing oxygen molecules. Due to this effect, more the oxygen ions are formed on the surface of the SMONs. Being as excellent active catalysts, noble metal nanoparticles can facilitate the adsorption of oxygen molecules and enhance the formation of oxygen ions by chemical reduction, which then spill onto the surface of

the SMONs, thus increasing the concentration of oxygen ions. The target molecules can also be directly adsorbed onto these noble metal nanoparticles, and then they migrate onto the surface of the SMONs to react with the oxygen ions. These spill-over effects significantly enhance the sensing performance. In addition, these noble metal nanoparticles can also accelerate the transfer of electrons onto the surfaces of the SMONs. Therefore, both the chemical sensitization and electronic sensitization enhance the sensitivity and speed of the SMONs-based sensors.

Table 3 Comparison of room temperature sensing properties of the noble metal modified semiconducting metal oxide nanostructures

| Material | Structure | Synthesis method | Target gas | Concentration (ppm) | Response value | $t_{res}/t_{rec}$ | LOD | Ref. |
|---|---|---|---|---|---|---|---|---|
| Au/ZnO ZnO | Nanostars | Hydrothermal | CO | 50 1000 | 55.3 0 | 10/12 s - | 5 ppm - | [113] |
| Pt/ZnO ZnO | Nanowires | Vapor-liquid-solid | CO | 0.1 | 1.02 0 | 120/180 s - | 100 ppb - | [114] |
| Au/ZnO ZnO | Nanowires | Hydrothermal | $H_2S$ | 5 | 79.4 5 | -/170 s -/860 S | ~1 ppm - | [242] |
| Au/ZnO ZnO | Nanorods | Vapor phase transport | $H_2S$ | 3 | ~475 ~125 | 11/20 min 10/13 min | ~0.5 ppm | [257] |
| Pd/ZnO | Nanoparticles | Sol-gel | $NO_2$ | 50 | 45.2[#] | 67/250 s | 10 ppm | [251] |
| Au/ZnO ZnO | Core-shells Shell | Sol-gel | HCOH | 5 | 10.57 1.91 | 138/104 s 332/736 s | 500 ppb - | [258] |
| Pt/$SnO_2$ | Porous | Solvothermal | CO | 100 | 64.5 | 144/882 s | ~50 ppm | [115] |
| Au/$SnO_2$ $SnO_2$ | Nanoparticles | Sputtering | $NO_2$ | 50 | 90[#] ~25[#] | 70/- s - | 600 ppb - | [243] |
| Au/$In_2O_3$ $In_2O_3$ | Nanorods | Aqueous solution | CO | 100 | 9 0 | 30/30 s - | ~50 ppm - | [244] |
| Ag/$TiO_2$ $TiO_2$ | Nanoparticles | Sol-gel | Ethanol | 5 | 4.35 1.54 | 52/61 s 112/136 s | 0.15 ppm - | [247] |
| Ag/$TiO_2$ $TiO_2$ | Nanorods | Wet chemical | Ethanol | 50 | 11. 98[*] 8.15[*] | 3/73 s 6/213 s | ~5 ppm | [116] |
| Pd/$TiO_2$ $TiO_2$ | Nanofibers array | Electrospinning | $NH_3$ | 100 | 6.97 0 | 3/150 s - | ~0.1 ppm - | [259] |
| Au/$TiO_2$ $TiO_2$ | Core-shell Shell | Sol-gel | $O_3$ | 2.5 | 3.27 1.36 | 5/24 s 32/76 s | 0.4 ppm - | [260] |
| Pt/$VO_x$ | Thin films | Magnetron sputtering | $CH_4$ | 500 | 18.2[#] | ~1000/~2000s | ~500 ppm | [261] |
| Au/$VO_2$ $VO_2$ | Nanosheets | CVD | $CH_4$ | 500 | ~70[#] ~35[#] | ~50/~100 s - | ~100 ppm | [262] |
| Au/$VO_2$ $VO_2$ | Nanowires | CVD/Ion sputtering CVD | $NO_2$ | 5 | 3.22 ~1 | ~50/~600 s - | ~0.5 ppm - | [130] |

| | | | | | | | | |
|---|---|---|---|---|---|---|---|---|
| Pd/Ga$_2$O$_3$ Ga$_2$O$_3$ | Nanowires | Thermal evaporation | NO$_2$ | 100 | 41.44[#] 0 | 200/70 s - | ~10 ppm - | 263 |
| Pd/ZnO | Nanowires | Electrochemical deposition | H$_2$ | 100 | 13100 | 6.4/7.4 s | - | 252 |
| Pd/ZnO | Nanowires | CVD | H$_2$ | 4000 | 1017.9[#] | 36/50 s | 20 ppm | 264 |
| Pd/ZnO ZnO | Nanorods | Aqueous solution | H$_2$ | 1000 | 91.2[#] ~20[#] | 18.8/- s - | 0.2 ppm - | 265 |
| Pt/SnO$_2$ SnO$_2$ | Nanoparticles | Aqueous solution | H$_2$ | 1000 | 10500 0 | 20/- s - | - | 249 |
| Pd/SnO$_2$ SnO$_2$ | Nanofibers | Electrospun | H$_2$ | 1000 | 12.09 ~3 | 4/3 s 2/- s | 0.02 ppm - | 266 |
| Pd/SnO$_2$ | Nanoparticles | Thermal vaporization | H$_2$ | 10000 | 120000[#] | 2/- s | 40 ppm | 253 |
| Pd/TiO$_2$ TiO$_2$ | Nanotubes | Sputtering | H$_2$ | 8000 5000 | 92.05[#] 54.6[#] | 3.8/43.3 s 73.8/103.8 s | - | 255 |
| Pt/TiO$_2$ | Nanocomposites | Pressing and sintering | H$_2$ | 1000 | 6000 | 10/20 s | - | 267 |
| Pd/WO$_3$ WO$_3$ | Nanocomposites Nanoplates | Hydrothermal | H$_2$ | 1000 | 34 ~0 | 24/- s - | - | 268 |
| Pt/Nb$_2$O$_5$ Nb$_2$O$_5$ | Porous ceramics | Pressing and sintering | H$_2$ | 10000 | 165 0 | 7/39 s - | 200 ppm - | 269 |
| Pt/In$_2$O$_3$ | Nanocubes | Hydrothermal | H$_2$ | 15000 | ~20 | 33/66 s | - | 241 |
| Au/In$_2$O$_3$ In$_2$O$_3$ | Nanofibers | Electrospinning | Ethanol | 100 | 11.12 5.4 | 47/351 s - | 20 ppm - | 270 |

*Notes:*

*C = concentration;*

*t$_{res}$/t$_{rec}$ = response time /recovery time;*

*LOD = limit of detection;*

*Response is defined as Ra/Rg (for reducing gases) or Rg/Ra (for oxidizing gases), Ra: resistance of the sensor exposed to reference, Rg: resistance of the sensor exposed to target:*

*\* Here the response is defined as ΔR/Rg (for reducing gases) or ΔR/Ra (for oxidizing gases), ΔR: the change in resistance.*

*# Here the response is defined as (ΔR/Rg)×100% (for reducing gases) or (ΔR/Ra)×100% (for oxidizing gases).*
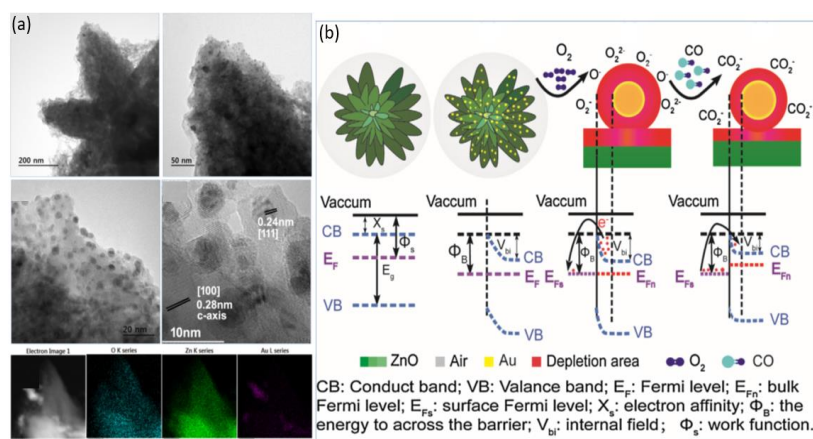
Fig. 14 (a) TEM images and element mapping of Au/ZnO nanostars; (b) Energy band diagrams of ZnO and Au/ZnO nanostars before and after CO exposure [113], © 2017 Elsevier.

At RT, some gases such as CO and $H_2$ are very difficult to be detected using the sensors made of the pristine SMONs. However, this problem might be solved by modifying the surface of these SMONs using noble metal nanoparticles. For example, Arunkumar et al. [113] prepared ZnO nanostar features using a hydrothermal route and then decorated these nanostars using Au nanoparticles with an average size of ~5-6 nm as shown in Fig. 14a. The ZnO nanostars decorated with 3 wt% gold nanoparticles can enhance the response (~15 for 50 ppm CO) and achieve very fast response/recovery times (~8/15 s) at 35 °C [113]. The selectivity of the sensor for Co sensing is excellent against the other interfering gases including methanol, ethanol, acetone and hydrogen. Fig. 14b shows the energy band diagrams of ZnO and Au/ZnO nanostars before and after CO exposure. Due to the spillover effect, a nanoscale depletion region is formed at the interface between Au nanoparticles and ZnO as a result of strong electronic interactions, thus altering the height of Schottky barrier. Therefore, the enhanced performance of the sensor operated at RT is attributed to the spillover effect [113].

Choi et al. [114] grew a network of ZnO nanowires using a vapor-liquid-solid method and then these nanowires were functionalized with Pd nanodots using a γ-ray radiolysis method, and the sensor made of these decorated nanowires shows an improvement of the sensing performance. This improvement is attributed to the electronic and chemical

sensitizations from the Pd nanodots [114]. Wang *et al.* [115] reported a highly sensitive RT CO sensor based on $Pt/SnO_2$ porous nanostructures. The porous $SnO_2$ nanostructures were synthesized using a solvothermal method, and Pt nanoparticles were then decorated onto the $SnO_2$ using hexachloro-platinic acid. The sensor exhibits a good response with a value of 64.5 to 100 ppm CO at RT. It also shows a good selectivity, compared to the other gases including CO, $H_2$, $N(CH_3)_3$, $NH_3$ and $CH_4$. Similarly, a RT CO gas sensor made of $Au/In_2O_3$ composite nano-rods was fabricated, and showed a high response and fast response/recovery times (30/30 s to100 ppm CO) [244].
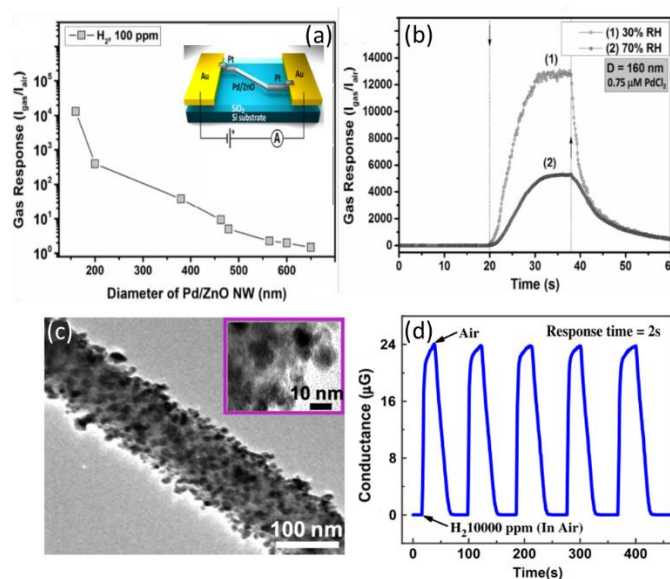


Fig. 15. (a) Responses of nanosensor based on single Pd/ZnO nanowires with different diameters to 100 ppm of $H_2$ at RT and 30% RH (the inset shows the schematic of the nanosensor device structure); (b) response of Pd/ZnO nanowires based sensor to 100 ppm of $H_2$ at 30% and 70% RH at RT. [252], © 2018 Elsevier. (c) TEM image of 30 at% $Pd/SnO_2$ nanofiber; (d) the response/recovery curves of 30 at% $Pd/SnO_2$ nanofiber based sensor for $H_2$ gas. [253], © 2010 Elsevier.

Modification of SMONs by noble metals can not only enhance the sensitivity, but also significantly improve the selectivity and response/recovery speed. For example, ZnO nanowire-based sensor modified with Pd nanoparticles exhibits both ultra-high sensitivity and very fast response and recovery [252, 264]. A Pd-modified ZnO nanowire-based RT nanosensor was prepared using electrochemical deposition by Lupan *et al* [252],

and it exhibits very fast response/recovery times of 6.4/7.4 s and a super-high response value of 13100 to 100 ppm $H_2$ as shown in Figs. 15a and15b. This $H_2$ sensor shows a very good selectivity against the other gases such as CO, $CH_4$, ethanol and acetone. The sensor can be operated with very low current levels at an ultra-low power consumption [252].

Ultra-sensitive RT hydrogen gas sensors based on noble metal modified $SnO_2$ have also been reported. For example, the sensor based on $Pt/SnO_2$ nanoparticles exhibits a super-high response (e.g., 10500 to 1000 ppm $H_2$) at RT [249]. Lee *et al.* [253] reported a RT hydrogen sensor made of $Pd/SnO_2$ nanowires (as shown in Fig. 15c) prepared using a thermal evaporation method, and the sensor shows an ultra-high sensitivity of about 120000% (defined as $(\Delta R/Rg)\times100\%$) to 10000 ppm $H_2$ and a fast response time of 2 s as shown in Fig. 15d. The $Pd/SnO_2$ nanofibers [266] were also synthesized using an electrospinning method, and the sensor made of these nanofibers exhibits a super-fast response/recovery times to $H_2$ (4/3 s to 1000 ppm $H_2$) and an ultra-low LOD of 20 ppb. The response of a sensor made of $Pt/TiO_2$ nanocomposites to 1000 ppm $H_2$ in $N_2$ was also reported as high as 6000 at RT, with short response/recovery times of only 10/20 s [267].
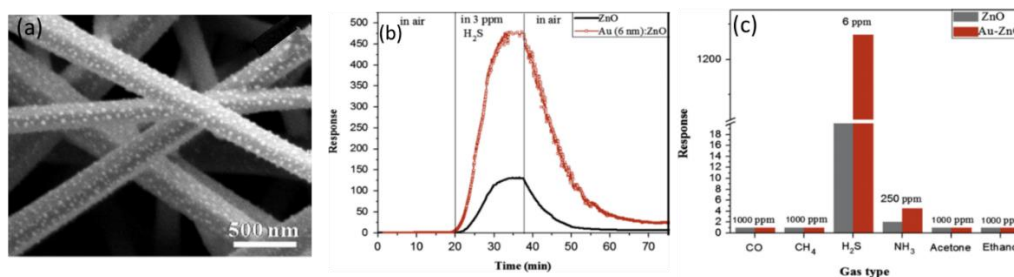


Fig. 16. (a) SEM image of Au/ZnO nanorods; (b) response/recovery curves of the Au/ZnO nanorods-based sensor and pristine ZnO nanorods-based sensor to 3 ppm $H_2S$ at room temperature; (c) responses of Au/ZnO nanorods-based sensor and pure ZnO nanorods-based sensor to different gases. [257], © 2015 Elsevier.

Apart from the chemical sensitization and electronic sensitization, there are other mechanisms to enhance the sensing performance of the SMONs. For example, the formation of nano-scale Schottky type junctions between Au nanoparticles and ZnO

nanorods and Au sulfidation with high concentrations of $H_2S$ [257]. Hosseini *et al.* [257] prepared ZnO nanorods using a vapor phase transport method, and found that $H_2S$ sensing performance has been significantly enhanced at RT after the modification of the surface of ZnO nanorods with Au nanoparticles (see Fig. 16a). As shown in Figs. 16b and 16c, both high response (1270 to 6 ppm of $H_2S$) and good $H_2S$ selectivity of the Au/ZnO nanorods have been achieved, which are much better than those of the pristine ZnO nanorods.

In summary, due to the combined effects of chemical sensitization and electronic sensitization, noble metal nanoparticles and other nanostructures are suitable to be used to modify the SMONs in order to improve the sensing performance of the RT gas sensors. One significant improvement is the shortening of the response and recovery times, along with the enhanced response values and selectivity.

### 3.1.2 Gas sensors based on conventional metal ion doped semiconducting metal oxide nanostructures

Doping of metal ions in the SMONs can increase the number of active sites and defects on the surface of SMON nanocrystals, thus enhance the amount of oxygen species and increase the adsorbed gas molecules on the sensor's surface. Therefore, the gas sensing performance of the SMONs can be effectively improved by doping of metal ions including $Al^{3+}$ [117, 271], $Cu^{2+}$ [272, 273], $Zn^{2+}$ [274], $Ni^{2+}$ [275, 276], $Co^{3+}$ [277, 278], $Fe^{3+}$ [279], $Mg^{2+}$ [280] and $Sb^{5+}$ [281]. The recent key sensing applications of RT gas sensors using this method are summarized in Table 4.

Table 4 Summary of room temperature sensors made of metal ion doped semiconducting metal oxide nanostructures and their sensing properties

| Material | Structure | Synthesis method | Target gas | C (ppm) | Response | $t_{res}/t_{rec}$ | LOD | Ref. |
|---|---|---|---|---|---|---|---|---|
| Al/NiO | Nanosheets | Solvent-thermal | $NO_2$ | 10 | 2.77* | 50/200 s | 250 ppb | [117] |
| Sb/WO₃ | Nanoparticles | Chemical solution | $NO_2$ | 10 | 51 | ~150/~200 s | ~1 ppm | [209] |
| Cu/Cu₂O | Hollow spheres | Hydrothermal | $NO_2$ | 10 | 6.27 | 34/- s | - | [282] |
| Cu/ZnO | Nanorods | Hydrothermal | $NH_3$ | 20 | 31.1# | 15/48 s | ~10 ppm | [118] |
| Sb/SnO₂ | Nanoparticles | Sol‑gel | $NH_3$ | 50 | 4316# | 70/- s | - | [283] |

| | | | | | | | | |
|---|---|---|---|---|---|---|---|---|
| Zn/NiO | Dendritic crystals | Electrolytic | NH$_3$ | 30 | 0.2* | 5/30 s | 5 ppm | [119] |
| Mg/ZnO | Thin films | Spray pyrolysis | NH$_3$ | 100 | 769 | 34/28 s | ~1 ppm | [284] |
| Ce$_{0.94}$Zr$_{0.06}$O$_2$ | Nanosheets | Sol-hydrothermal | NH$_3$ | 100 | 87 | - | 100 ppb | [127] |
| Co/CuCo$_2$O$_4$ | Nanoplatelets | Hydrothermal | NH$_3$ | 400 | 7.9# | -/14 min | ~25 ppm | [273] |
| Fe/WO$_3$ | Microspheres | Spray pyrolysis | Ethanol | 400 | ~140 | ~10/~40 s | ~100 ppm | [279] |
| Al/ZnO | Hexagonal facets | Sol-gel | Ethanol | 300 | 94# | 68/50 s | - | [271] |
| Co/TiO$_2$ | Nanoparticles | Sol-gel | Ethanol | 500 | ~105# | - | - | [277] |
| SnO$_2$:Sb | Nanowires | CVD | Ethanol | 300 | 1.3 | 10/87 s | 40 ppm | [285] |
| Na/ZnO | Nanoflowers | Solution route | Acetone | 100 | 3.35 | 18/63 s | 0.2 ppm | [286] |
| Ni/ZnO | Nanorods | Electrodeposition | Acetone | 100 | 1.6 | - | - | [275] |
| Sb/SnO$_2$ | Nanoribbons | Thermal evaporation | H$_2$S | 100 | ~18 | ~500/~500 s | 100 ppb | [281] |
| Zn/ZnO | Nanotetrapods | Thermal evaporation | H$_2$S | 4 | 38# | ~200/~1000 s | 1 ppm | [287] |
| Zn/In$_2$O$_3$ | Nanowires | CVD | CO | 5 | ~57# | 20/10 s | ~1 ppm | [274] |
| Sb/SnO$_2$ | Nanoporous films | Sol-gel | Cl$_2$ | 3 | 500* | 60/120 s | ~1 ppm | [288] |
| Mg/ZnO | Nanorods | Frequency sputtering | H$_2$ | 200 | 30 | 85/70 s | - | [289] |
| Mg/ZnO | Film | Rf sputtering | H$_2$ | 200 | 35-40 | 75/54 s | - | [280] |
| Cd/ZnO | Nanowires | Electrodeposition | H$_2$ | 100 | 274# | 14/11 s | - | [89] |
| Al/ZnO | Nanowires | Electrodeposition | Ethanol | 1000 | 1.7 | 10/30 s | - | [290] |
| Co/TiO$_2$ | Mesoporous | Self-assembly | H$_2$ | 1000 | 4082 | 66/- s | 50 ppm | [278] |
| Nb/TiO$_2$ | Nanotubes | Annealing | H$_2$ | 1000 | 30.9# | 100/- s | - | [291] |

*Notes:*

*C = concentration;*

*t$_{res}$/t$_{rec}$ = response time /recovery time;*

*LOD = limit of detection;*

*Response is defined as Ra/Rg (for reducing gases) or Rg/Ra (for oxidizing gases), Ra: resistance of the sensor exposed to reference, Rg: resistance of the sensor exposed to target:*

*\* Here the response is defined as ΔR/Rg (for reducing gases) or ΔR/Ra (for oxidizing gases), ΔR: the change in resistance.*

*# Here the response is defined as (ΔR/Rg)×100% (for reducing gases) or (ΔR/Ra)×100% (for oxidizing gases).*
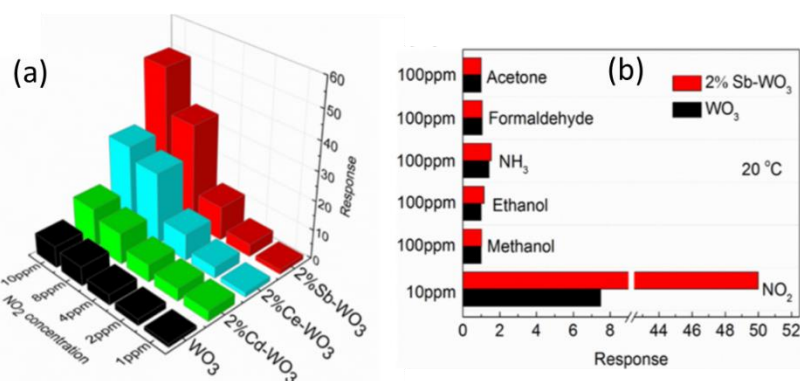
Fig. 17. (a) Responses of sensors made of 2%-Sb-WO$_3$, 2%-Ce-WO$_3$ and 2%-Cd-WO$_3$ to different concentration of NO$_2$; (b) responses of sensors made of 2%-Sb-WO$_3$ to different gases. [209], © 2017 American Chemical Society.

The amount of dopant Al$^{3+}$ ions was found to significantly affect the gas sensing properties of NiO nanosheets [117]. Al$^{3+}$ doped NiO nanosheets have introduced many new oxygen vacancies due to aliovalent ion doping. Superoxide complexes such as Ni$^{2+}$-O$_2^{-}$ are easily formed on the surface of the NiO due to the existence of oxygen vacancies. As they are very active, they can significantly increase the sensitivity of the NiO nanosheets. Compared with those of the pure NiO nanosheets, the response to NO$_2$ for the Al doped NiO nanosheets based sensor to NO$_2$ was enhanced up to 35 times at RT. Doping with metal ions including Sb, Cd, and Ce have also been proved to enhance the sensing properties of the WO$_3$ nanoparticles to NO$_2$ gas at RT [209]. Among these, Sb-doped WO$_3$ nanoparticles exhibit a 6.8 times higher response and a much better selectivity than those of the undoped WO$_3$ (as shown in Figs. 17). The enhancement mechanisms have been identified to be the increase in the number of oxygen vacancies on the surface of metal doped WO$_3$ based on the analysis results from photoluminescence, Raman spectroscopy and XPS [209].

The responses and recovery speeds of the sensor can be significantly improved by doping of metal ions into the SMONs, which is important for the practical applications of the RT gas sensors. For example, Zn-doped NiO dendritic nanostructure [119] exhibits faster responses (5-8 times) and faster recovery (30-50 times) rates than those of the pure NiO dendritic crystals. Sensor based on Mg-doped ZnO thin films on glass substrates deposited through spray pyrolysis process [284] shows a much higher response

(796 towards 100 ppm of $NH_3$) and faster response/recovery speeds (34/28 s) than those of the pure ZnO film measured at RT. The sensor based on Sb doped $SnO_2$ nanowires prepared using a chemical vapor deposition (CVD) method [285] shows a typical p-type behavior, and a fast response time of about 10 s to 300 ppm ethanol at RT.
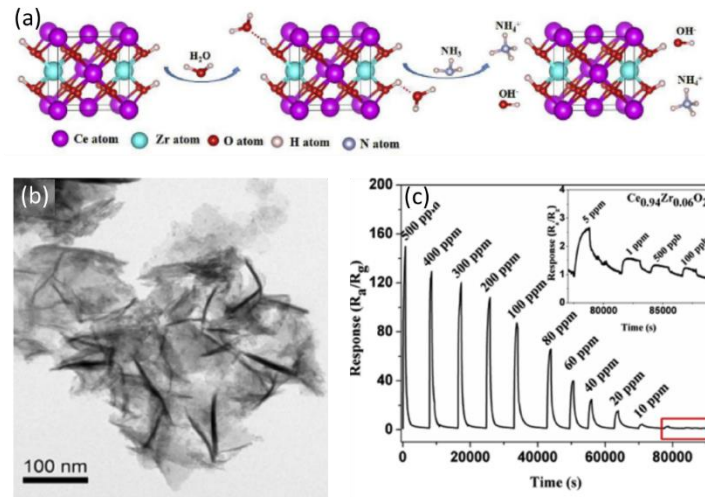


Fig. 18. (a) Schematic diagrams of the $NH_3$ reaction mechanism on the surface of $Ce_{0.94}Zr_{0.06}O_2$ nano-sheets; (b) TEM image of porous $Ce_{0.94}Zr_{0.06}O_2$ nano-sheets; (c) response/recovery curves of the porous $Ce_{0.94}Zr_{0.06}O_2$ nanosheets based sensor to $NH_3$. [127], © 2018 Elsevier.

Adsorption of water vapor on the SMONs surfaces is sometimes enhanced by metal ions doping, which seems a bad news for a gas sensor. However, for RT $NH_3$ gas sensors, this is especially beneficial as the $NH_3$ molecules react with the absorbed $H_2O$ to form the $NH_4^+$ and $OH^-$ as is schematically shown in Fig. 18a. The electrolytic conductivity of $NH_4^+$ and $OH^-$ can significantly improve the sensitivity of sensors at RT [127, 198]. Porous $Ce_{0.94}Zr_{0.06}O_2$ nano-sheets (see Fig. 18b) with an average thickness of 8 nm was prepared using a sol-hydrothermal process [127]. Doping of $Zr^{4+}$ ions into the $CeO_2$ nanosheets enlarges the specific surface areas (185.4$m^2$/g) and increases the pore volumes (0.51 $cm^3$/g). These modifications result in a much higher sensitivity (e.g. 87 to100 ppm $NH_3$) at RT (see Fig. 18c), better selectivity and a very low LOD of 100 ppb.

The $H_2$ sensors made of metal ion doped SMONs were reported to exhibit high responses, although their response/recovery times were also reported to be longer than

those made of the noble ions modified SMONs-based RT $H_2$ gas sensors [278, 280, 289, 291].

For examples, Co-doped $TiO_2$ sensors exhibit an ultra-high response with a value of 4082 to 1000 ppm $H_2$ gas, although the response time is 66 s, which is quite slow for detection of highly explosive $H_2$ [278].

In summary, compared to those sensors made of noble metal nanoparticle modified SMONs, the improved effects of gas sensors made of the metal ions modified SMONs are not as significant. However, the SMONs can be modified simultaneously by both metal ions and noble metal nanoparticles, which will combine the advantages of both metal ions and noble metal nanoparticles.

## 3.2  Composites of semiconducting metal oxide nanostructures and gas sensors

### 3.2.1  Mechanism for enhanced sensing performance

The RT gas sensing performance of the SMONs operated at RT can be improved by integrating them with other metal oxides or carbon nanomaterials. For example, heterojunctions can be formed at the interfaces of different metal oxides or at the interfaces between SMONs and carbon nanomaterials, as schematically illustrated in Fig. 19. At the p-n heterojunctions between p-type and n-type SMONs, the electrons at the conduction band states of n-type SMONs will transfer to the lower energy valence band states of p-type SMONs across the interface. Thus, a depletion layer will form at the p-n heterojunction due to recombination of electrons and holes.

For the n-n heterojunction, the electrons will be transported at the interfaces between different materials due to their differences of their conduction band states. As a result, a depletion layer forms at the surface of n-type SMONs with higher-energy conduction band states due to the loss of electrons. At the same time, an accumulation layer forms at the surface of n-type SMONs with lower-energy conduction band states due to the accumulation of electrons.

For the p-p heterojunction, the major charge carriers are holes. Due to the differences of valence band energies of different SMONs, the charge carriers are transported from one p-type SMON (which has a higher energy valence band state) to the other p-type

SMON (which has a lower-energy valence band state). Therefore, there are hole depletion region formed at the surface of the first SMONs (with higher energy valence band state) and the hole accumulation region forms at the surface of the second SMONs (with a lower energy valance band state) as shown in Fig. 19.
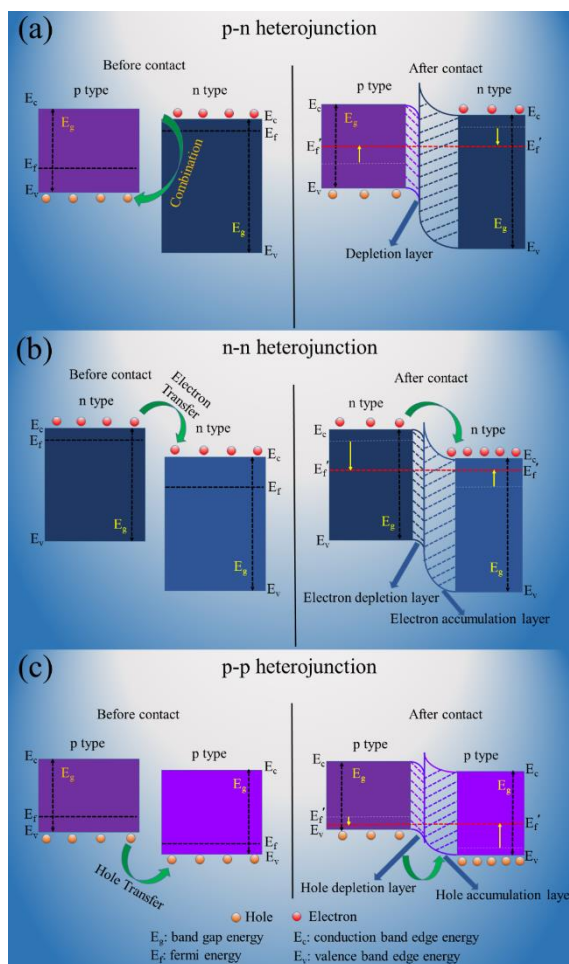


Fig. 19. Schematic illustrations of the energy band structures at heterojunction interfaces of different types of heterojunctions. (a) p-n junction, (b) n-n junction and (c) p-p junction.

These formed heterojunctions can effectively accelerate the transport of electrons. On the other hand, these heterojunctions can also enhance oxygen adsorption, therefore, abundant oxygen vacancies are formed on the surfaces of the SMONs composites, which can provide new active sites for sensing reaction. In addition, the composites of SMONs often contain numerous mesopores, which are beneficial to the adsorption and desorption of gas molecules. All of these effects will improve the sensitivity and

response rates of the RT gas sensors made of composites of the SMONs.

### 3.2.2  Gas sensors based on composites of semiconducting metal oxide nanostructures and other metal oxides

Composite oxides of the SMONs have been proposed to combine two or more semiconducting metal oxides together to enhance the gas sensing performance at RT. The examples of composites include: n-type SMONs with n-type SMONs (e.g. $Fe_2O_3$/ZnO [292], ZnO/$SnO_2$ [293], $In_2O_3$/$SnO_2$ [134, 294]), p-type SMONs with n-type SMONs (e.g. NiO-ZnO [120], CuO/$TiO_2$ [121], $In_2O_3$/CuO [122], NiO/$WO_3$ [295]) and p-type SMONs with p-type SMONs (e.g. $Cu_2O$/$Co_3O_4$ [296] and NiO/CuO [131] In addition, the composite formed by integrating the SMONs with non-semiconductor metal oxide (e.g. $K_2O$/$In_2O_3$ [129] and CaO/$SnO_2$ [251]) have also been reported.

Table 5 summarizes the recently reported RT gas sensors made of composite oxides of the SMONs and/or other metal oxides. For these composite oxides, a number of oxygen vacancies are formed on both the surfaces and interfaces, which provides many active sites for the gas sensing reactions. Plenty of defects will also be formed at the interfaces of nanostructures in different metal oxides nanoparticles. In addition, the heterojunctions are usually formed at the interfaces of different metal oxides, which can effectively accelerate the electron transfer between different particles, thus accelerating the response speed of the sensor. Besides, the composite oxides often contain lots of mesoporous structures due to the accumulation of nanoparticles, which are beneficial to the adsorption and desorption of gas molecules. These factors can improve the sensing performance of the sensor made of these composite oxides, especially for the sensitivity and response speed. Most sensors made of the composite oxides exhibit very fast response times at RT. For examples, the gas sensor based on nanocomposite of CuO/$TiO_2$ [121] shows a very fast response time of 2 s at RT, and the sensor based on plate-like NiO/$WO_3$ nanocomposites [295] exhibits excellent sensitivity and ultrafast response/recovery times (2.5/1.1s) to $NO_2$ at RT.

Table 5 Room temperature sensing properties of composite of semiconducting metal oxide nanostructures and other metal oxides

| Material | Structure | Synthesis method | Target gas | C (ppm) | Response | $t_{res}/t_{rec}$ | LOD | Ref. |
|---|---|---|---|---|---|---|---|---|
| NiO/ZnO | Nanocones | Hydrothermal | NH$_3$ | 50 | 42[#] | 27/150 s | ~15 ppm | [120] |
| CuO/TiO$_2$ | Nanoparticles | Sol-gel | NH$_3$ | 50 | 97[#] | 2/55 s | ~5 ppm | [121] |
| In$_2$O$_3$/CuO | Nanofibers | Electrospinning | NH$_3$ | 100 | 1.9[*] | 2/- s | 0.3 ppm | [122] |
| Silica/CeO$_2$ | Nanoparticles | Hydrothermal | NH$_3$ | 80 | 3244[#] | 750/- s | 0.5 ppm | [198] |
| Fe$_2$O$_3$/ZnO | Nanorods | Sol-gel | NH$_3$ | 0.4 | 10000 | 20/20 s | - | [292] |
| Cr$_2$O$_3$/ZnO | Thick film | Screen-printing | NH$_3$ | 300 | 13.7[*] | 25/75 s | - | [297] |
| CuO/MNO$_2$ | Flower/sheets | Hydrothermal | NH$_3$ | 100 | 135[#] | 120/600 s | 20 ppm | [298] |
| ZnO/SnO$_2$ | Thin film | Hydrothermal | NH$_3$ | 20 | 1.1 | 300/- s | 5 ppm | [293] |
| NiO/WO$_3$ | Plates | Annealing | NO$_2$ | 30 | 4.8 | 2.5/1.1 s | 5 ppm | [295] |
| CaO/SnO$_2$ | Rod-like | Electrospinning | NO$_x$ | 97 | 6.63[*] | - | 10 ppb | [299] |
| In$_2$O$_3$/SnO$_2$ | Nanorods | Electrospinning | NO$_x$ | 100 | 8.98[*] | 4.67/- s | 0.1 ppm | [134] |
| In$_2$O$_3$/TiO$_2$ | Nanofibers | Electrospinning | NO$_x$ | 97 | 41.1[#] | 3/- s | 97 ppb | [300] |
| Al$_2$O$_3$/TiO$_2$ | Nanotubes | Induction | NO$_x$ | 97 | 88.04[#] | ~8/~8 s | 0.97 ppm | [301] |
| K$_2$O/In$_2$O$_3$ | Nanowires | Template | NO$_x$ | 97 | 151.78[*] | 12/- s | 48.5 ppb | [129] |
| NiO/SnO$_2$ | Nanosheets | Annealing | NO$_2$ | 60 | ~7.5[*] | - | ~5 ppm | [302] |
| SnO$_2$/NiO | Thin film | RF sputtering | H$_2$S | 10 | 440 | - | 100 ppb | [123] |
| Cu$_2$O/Co$_3$O$_4$ | Heteroarrays | Electrodeposition | H$_2$S | 20 | ~2600 | ~100/~100 s | ~0.1 ppm | [296] |
| NiO/CuO | flower-like | Hydrothermal | NO$_2$ | 100 | 77.16[#] | 2 s/- | 1 ppm | [131] |
| NiO/In$_2$O$_3$ | Nanofibers | Electrospinning | H$_2$S | 3 | 6 | 14/22 s | 3 ppm | [303] |
| SnO$_2$/CuO | Heterojunctions | Screen printing | H$_2$S | 1 | 3672[*] | 15/- s | 10 ppm | [304] |
| CuO/ZnO | Nanorods | Pulsed laser deposition | H$_2$S | 0.5 | 25[#] | 180/15 s | ~0.5 ppm | [305] |
| In$_2$O$_3$/ZnO | Core-shells | Hydrothermal | H$_2$S | 700 | 925[#] | - | 20 ppm | [306] |
| α-Fe$_2$O$_3$/ZnO | Nanowires | Piezo-surface coupling | Ethanol | 700 | 706.8[#] | - | ~100 ppm | [307] |
| ZnO/CuO | Nanoparticles | Hydrothermal | Alcohol | 20 | 3.32 | 62/83 s | ~150 ppm | [308] |
| VO$_2$/ZnO | Heteronanostructures | Heteroepitaxial | Acetone | 100 | 4.51 | 8/18 s | ~10 ppm | [309] |
| CuO/ZnO | Thick film | Screen-printing | Cl$_2$ | 300 | 195[*] | 18/50 s | - | [310] |
| ZnO/SnO$_2$ | Heterojunctions | Hydrothermal | Ozone | 0.06 | 12 | 13/90 s | 20 ppb | [311] |
| NiO/Nb$_2$O$_5$ | Nanoparticles | Hydrothermal | H$_2$ | 500 | 1.68 | 100.42/524.84 s | - | [312] |
| Cr$_2$O$_3$/Nb$_2$O$_5$ | Nanoparticles | Hydrothermal | H$_2$ | 200 | 5.24 | 40/- s | - | [313] |

*Notes:*

*C = concentration;*

*$t_{res}$/$t_{rec}$ = response time /recovery time;*

*LOD = limit of detection;*

*Response is defined as Ra/Rg (for reducing gases) or Rg/Ra (for oxidizing gases), Ra: resistance of the sensor exposed to reference, Rg: resistance of the sensor exposed to target:*

*\* Here the response is defined as ΔR/Rg (for reducing gases) or ΔR/Ra (for oxidizing gases), ΔR: the change in resistance.*

*# Here the response is defined as (ΔR/Rg)×100% (for reducing gases) or (ΔR/Ra)×100% (for oxidizing gases).*
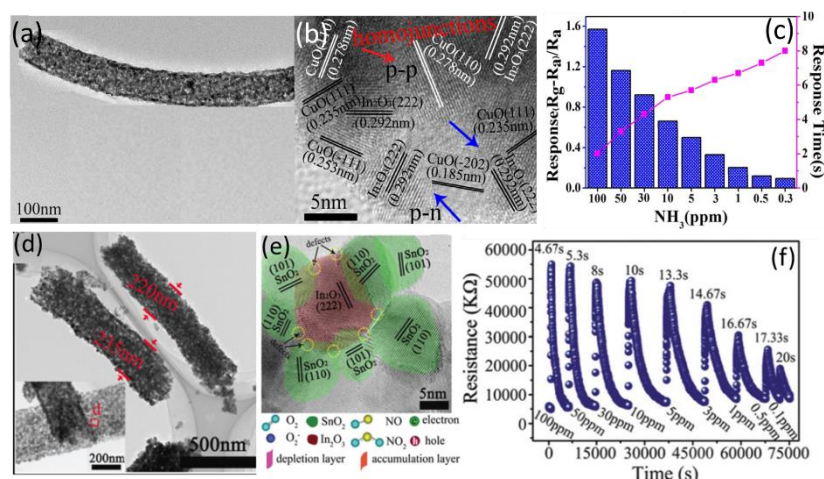


Fig. 20. (a) TEM and (b) HRTEM images of mesoporous $In_2O_3$/CuO composite multijunction nanofibers, (c) response values and times of the sensor to different concentrations of $NH_3$. [122], © 2018 Elsevier. (d, e) TEM images of composite of $In_2O_3$/$SnO_2$ nanorod heterostructures; (f) response/recovery curves of the sensor to different concentration of $NO_x$. [134] © 2015 The Royal Society of Chemistry.

The composite of mesoporous $In_2O_3$/CuO multijunction nanofibers [122] was prepared using an electrospinning method by Zhou *et al*. The composite is composed with the $In_2O_3$ nanoparticles and CuO nanoparticles (with a molar ratio of Cu:In of 100:5). The TEM images shown in Figs. 20a and 20b indicate that the composite has many mesoporous structures with diameters from 1.9 to 22.9 nm and large specific surface areas (48.7 $m^2$/g). The $In_2O_3$ nanoparticles are surrounded by the CuO nanoparticles to form numerous p-p homojunctions and p-n heterojunctions [122]. XPS analysis indicates that the ratio of oxygen defect/vacancy on its surface is as high as 45.4%. Due to the

existence of larger specific and mesoporous surface areas and the availability of chemisorbed oxygen and the formation of heterojunctions, the sensor has a much higher response to $NH_3$ than those of a CuO nanostructured sensor. The response time is also very short with a value lower than 8 s for $NH_3$ from 0.3 to 100 ppm (see Fig. 20c). The selectivity and LOD are also significantly improved due to the addition of $In_2O_3$.

Xu et al. [134] prepared composites of $In_2O_3$/$SnO_2$ nanorod heterostructures (see Figs. 20d and 20e) using the electrospinning to improve the oxygen deficiency and carrier density of the $SnO_2$. The $SnO_2$ nanoparticles are distributed along with the $In_2O_3$ to form numerous heterojunctions and defects at their interfaces. The availability of oxygen vacancies on the surface and at the interface has been verified using XPS [134]. Compared with pure $SnO_2$ nanorods, $In_2O_3$/$SnO_2$ nanorods (with the atom ratio of 25:0.3 of Sn:In) exhibit 11 times higher response to $NO_x$ with a very faster response time of 4.67 s and a lower LOD with a value of 0.1 ppm (see Fig. 20f).

NiO/CuO nanocomposites with the NiO:CuO molar ratio of 1:1 have been synthesized using a hydrothermal method [131], and the nanocomposites are consisted of CuO nanoparticles and NiO nanoplates with lots of mesoporous structures. The p-p heterojunctions formed at the interfaces of NiO and CuO accelerates the electron transfers from NiO to CuO, thus resulting in a faster response. The mesoporous hierarchical nanostructures with much larger surface areas facilitate effective adsorption and desorption of gas molecules on the surface. Thus, it exhibits an ultra-fast response speed (2 s to 100 ppm $NO_2$) to $NO_2$ at RT.
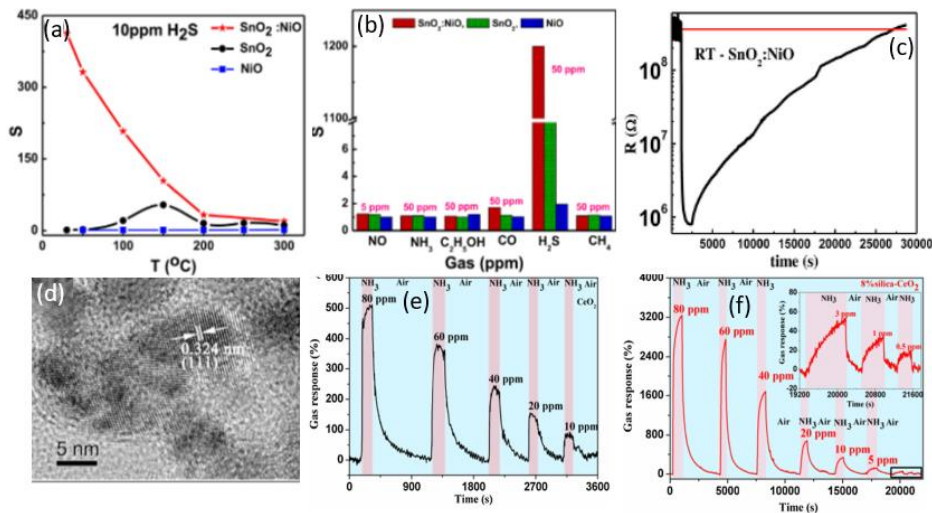
Fig. 21. (a) Response histogram of $SnO_2/NiO$ thin film-based room temperature gas sensor to different gases; (b) response values of the $SnO_2/NiO$ thin film-based RT gas sensor to different concentration of $H_2S$; (c) response/recovery curve to 100 ppm $H_2S$. [123], © 2017 Elsevier. (d) TEM image of 8% silica-$CeO_2$; (e) response/recovery curves of the pure $CeO_2$-based sensor to $NH_3$; (f) response/recovery curves of the 8% silica-$CeO_2$-based sensor to $NH_3$. [198], © 2017 Elsevier.

Kaur *et al.* [123] prepared a $SnO_2/NiO$ thin film using a sputtering method and then fabricated a RT $H_2S$ sensor As shown in Fig. 21a, the sensor exhibits a high response with a value of 440 to 10 ppm $H_2S$, which is 9 and 415 times higher than those made of pure $SnO_2$ and NiO films, respectively. Selectivity has also been improved using the $SnO_2/NiO$ thin film (see Fig. 21b). The formation of p-n heterojunctions using the p-type NiO and n-type $SnO_2$ semiconductors apparently changes the resistance of the composite film. The enhanced response of $SnO_2$:NiO nanocomposite sensor is mainly due to the modifications of p-n junctions resulted from the conversion of NiO to metallic NiS. However, the recovery time is quite long (>20000 s, see Fig. 21c).

Wang *et al*. [198] reported a composite oxide sensor using 8% silica modified $CeO_2$ nanomaterials (see Fig. 21d) synthesized using a sol-hydrothermal route. The addition of silica increases the specific surface areas (83.75 $m^2/g$) and decreases the crystal sizes. Due to the existence of silica, lots of $OH^-$ species are formed on the surface of the sensor, which facilitate the adsorption of water, and the water molecules react with $NH_3$ to generated $NH^{4+}$ and $OH^-$ and decrease the electrical resistance of the sensor. As shown in Figs. 21e and 21f, the $NH_3$ gas sensing performance of the sensor is significantly enhanced as compared to that of pure $CeO_2$ at RT. Its response value reaches 3244% (defined as $(\Delta R/Rg) \times 100\%$) for 80 ppm of $NH_3$ gas.
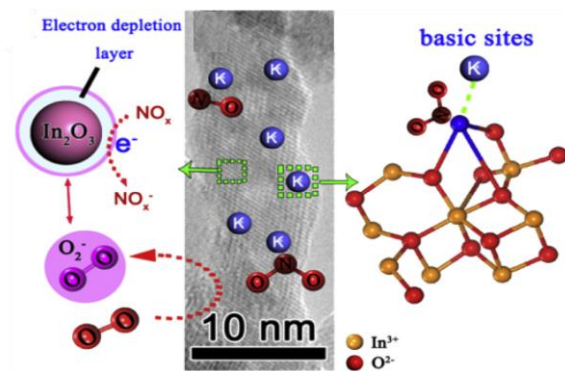
Fig. 22. Gas sensing mechanism to $NO_x$ of mesoporous $K_2O$-$In_2O_3$ nanowires. [129], © 2016 Elsevier.

The composites of alkali metal oxide and SMONs have also been reported as an effective way to enhance of the sensitivity for sensing acidic gases, such as $NO_x$ [129]. As shown in the gas sensing mechanism of mesoporous $K_2O$-$In_2O_3$ nanowires in Fig. 22 the alkali metal oxides on the surfaces can serve as alkaline center, which is beneficial to the adsorption and diffusion of acidic gases. Using mesoporous Santa Barbara Amorphous Material-16 (SBA-16) as a template, Rehman *et al.* [129] prepared highly crystalline mesoporous $K_2O$-$In_2O_3$ nanowires with the diameters of 4-8 nm and pore sizes of 3-5 nm. The composite nanowires possess numerous chemisorbed oxygen and alkaline centers on their surfaces. The gas sensing performance of the mesoporous $K_2O$-$In_2O_3$ composite nanowires has been significantly improved with the addition of $K_2O$. Its response is 151.78 to 97 ppm of $NO_x$, the response time is decreased to 12 s, and the LOD is as low as 48.5 ppb at RT [129].

Most reported composite SMON sensors exhibit higher response values and faster response time than those of the single phase SMONs. Many active sites can be generated in the composite SMONs, such as oxygen vacancies, heterojunctions, defects and mesopores, which can effectively enhance the sensing performance. The composite SMON can be further modified by noble metal nanoparticles, which takes advantage of the chemical sensitization and electronic sensitization of noble metal nanoparticles on the composite SMONs.

### 3.2.3 Gas sensors based on composites of semiconducting metal oxide nanostructures and carbon nanomaterials

Carbon nanomaterials including carbon nanotubes and graphene have been demonstrated as promising sensing materials [314]. However, the carbon nanomaterial-based gas sensors generally show low sensitivity and slow response/recovery speeds at RT. The synergistic effect by combining SMONs and carbon nanomaterials can improve the sensing performance because: (1) conductivity is significantly improved; (2) many active sites (such as oxygen functional groups, vacancies and defects) are formed at the interfaces. Because of the fast carrier transport kinetics, the composites of the SMONs combined with carbon nanomaterials show the enhanced sensitivity and fast response/recovery at RT.

Table 6 summarizes the RT sensing properties of some composite nanostructures of the SMONs and carbon nanomaterials. Among these carbon materials, the composites of reduced graphene oxide (rGO) and SMONs are the mostly investigated one for the gas sensor applications. The rGO has been used to combine with various types of the SMONs for enhancing the gas sensing properties, and these SMONs include $Fe_2O_3$ [315], $In_2O_3$ [316], ZnO [317, 318], $Fe_3O_4$ [319], $SnO_2$ [320-324], $WO_3$ [325], $NiO/SnO_2$ [326] and $Pd/TiO_2$ [327].

Table 6 Room temperature sensing properties of composite nanostructures of semiconducting metal oxide nanostructures and carbon nanomaterials

| Material | Structure of SMONs | Synthesis method of SMONs | Target gas | C (ppm) | Response | $t_{res}/t_{rec}$ | LOD | Ref. |
|---|---|---|---|---|---|---|---|---|
| Graphene/$SnO_2$ | Nanoparticles | Sol-gel | $NO_2$ | 20 | ~9.5 | <1/5 min | 5 ppm | [124] |
| $SnO_2$/rGO | Nanoparticles | Hydrothermal | $NO_2$ | 1000 | 22.87# | 100/- s | 1 ppm | [328] |
| $SnO_2$/rGO | Nanoparticles | Hydrothermal | $NO_2$ | 1 | 3.8 | 14/190 s | 50 ppb | [329] |
| $WO_3$/MWCNTs | Nanoparticles | Metal organic decomposition | $NO_2$ | 0.1 | 0.25* | 10.5/20 min | 100 ppb | [125] |
| rGO/α-$Fe_2O_3$ | Nanoparticles | Hydrothermal | $NO_2$ | 5 | 3.86 | 76/946 s | 0.1 ppm | [126] |
| α-$Fe_2O_3$/rGO | Nanospheres | Hydrothermal | $NO_2$ | 90 | 150.63# | -/1648 s | 0.18 ppm | [330] |
| $Fe_3O_4$/Graphene | Nanoparticles | Hydrothermal | $NO_2$ | 400 | 24.2# | 275/738 s | ~30 ppm | [331] |
| Graphene/ZnO | Spheres | Solvothermal | $NO_2$ | 50 | 8# | 132/164 s | ~10 ppm | [332] |
| ZnO/rGO | Nanowalls | Solution | $NO_2$ | 50 | 9.61 | 25/15 s | ~5 ppm | [135] |
| ZnO/rGO | Nanorods | Oriented growth | $NO_2$ | 1 | 119# | 75/132 s | 50 ppb | [333] |
| rGO/NiO | Nanosheets | Hydrothermal | $NO_2$ | 0.25 | 0.04* | 576/121 s | ~0.25 ppm | [334] |
| $In_2O_3$/rGO | Nanosheets | Hydrothermal | $NO_2$ | 30 | 8.25 | 4/24 min | ~5 ppm | [335] |

| Material | Morphology | Method | Gas | Conc. | Response | Response/Recovery | Detection limit | Ref. |
|---|---|---|---|---|---|---|---|---|
| In$_2$O$_3$/rGO | Layers | Reflux | NO$_x$ | 97 | 1.45$^*$ | 25/- s | 970 ppb | [336] |
| rGO/CeO$_2$ | Bilayer | Spray | NO$_2$ | 10 | 20.5$^\#$ | 92/- s | ~1 ppm | [337] |
| rGO/Cu$_2$O | Nanoparticles | Chemical solution | NO$_2$ | 1 | 5.2 | 29.2/76.8 s | 100 ppb | [338] |
| CuO/rGO | Nanosheets | Chemical solution | NO$_2$ | 1 | 14 | 66/34 s | 60 ppb | [339] |
| Co$_3$O$_4$/rGO | Thin sheets | Hydrothermal | NO$_2$ | 800 | ~8$^\#$ | 1.5/1 min | 60 ppm | [340] |
| CuxO/Graphene | Nanoflowers | Reflux | NO$_x$ | 97 | 95.1$^\#$ | 9.6/- s | 97 ppb | [341] |
| CeO$_2$/Graphene | Nanosheets | Solvothermal | NO$_x$ | 300 | 12.76$^\#$ | 1.3/- s | 5 ppm | [342] |
| Graphene/SnO | Hybrid film | CVD | NH$_3$ | 100 | 35$^\#$ | ~10/- s | ~5 ppm | [343] |
| SnO$_2$/rGO | Nanorods | Hydrothermal | NH$_3$ | 200 | 1.3 | 8/13 s | 20 ppm | [344] |
| SnO$_2$/MWCNTs | Nanocomposites | Microelectronic | NH$_3$ | 200 | 26 | <5/5 min | ~40 ppm | [136] |
| rGO/TiO$_2$ | Microspheres | Hydrothermal | NH$_3$ | 30 | ~3.5$^\#$ | ~10/~10min | 5 ppm | [345] |
| Cu$_2$O/rGO | Nanorods | Hydrothermal | NH$_3$ | 200 | 2.04 | 28/206 s | ~100 ppm | [346] |
| ZnO/GrO | Nanosheets | Chemical solution | NH$_3$ | 1 | 24$^\#$ | 6/2-3 s | 1 ppm | [347] |
| ZnO/CNT | Networks | Flame | NH$_3$ | 100 | 330 | 18.4/35 s | 200 ppb | [348] |
| VO$_2$/CNT | Nanocomposites | Hydrothermal | NH$_3$ | 45 | 0.04$^*$ | 290/1800 s | 20 ppb | [349] |
| Graphene/SnO$_2$ | Nanohybrids | Electrochemical deposition | HCOH | 5 | 4.6$^\#$ | 46/95 s | 0.02 ppm | [350] |
| rGO/TiO$_2$ | Nanosheets | Spray method | HCOH | 0.5 | 0.4$^\#$ | 70/126 s | ~0.1 ppm | [351] |
| SnO$_2$/rGO | Quantum wires | Spin coating | H$_2$S | 50 | 33 | 2/292 s | 43 ppb | [4] |
| TiO$_2$/rGO | Nanotubes | Hydrothermal | Methanol | 800 | 96.93$^\#$ | 18/61 s | 10 ppm | [352] |
| ZnO/MWNTs | Nanorods | Hydrothermal | Ethanol | 50 | 4.5$^\#$ | 7/11 s | ~5 ppm | [353] |
| CuO/rGO | Nanocomposites | Hydrothermal | CO | 1 | 2.56$^\#$ | 70/160 s | 0.25 ppm | [354] |
| SnO$_2$/MWCNT | Nanofibers | Electrospinning | CO | 50 | 1.29 | - | 47 ppm | [355] |
| SnO$_2$/rGO | Hybrid film | Hydrothermal | Acetone | 10 | 2.1$^\#$ | 107/95 s | ~10 ppm | [356] |
| ZnO/Graphene | Nanotubes | Hydrothermal | H$_2$ | 100 | 28.08$^\#$ | 30/~150 s | 10 ppm | [357] |
| CuO/rGO/CuO | Sandwich | Hydrothermal | H$_2$ | 1500 | ~12$^\#$ | 80/60 s | 10 ppm | [358] |
| F-MWCNTs/SnO$_2$ | Networks | Sputtering | H$_2$ | 500 | 5.4$^\#$ | -/9 s | - | [359] |
| SnO$_2$/Ni-graphene | Nanoparticles | Chemical solution | NO | 40 | 15 | - | - | [360] |
| Pd/SnO$_2$/rGO | Nanoparticles | Chemical solution | H$_2$ | 10000 | 50$^\#$ | - | 100 ppm | [361] |
| Pd/SnO$_2$/rGO | Nanoparticles | Hydrothermal | CO | 1600ppm | 9.5$^\#$ | 2 min/2 min | ~50ppm | [362] |
| Pd/SnO$_2$/rGO | Nanoparticles | Hydrothermal | Methane | 4000ppm | 2.07$^\#$ | 10 min/-- | - | [363] |
| Ag/SnO$_2$/rGO | Nanoparticles | Hydrothermal | NO$_2$ | 5 | 2.17 | 49/339 s | 1 ppm | [364] |
| Pd/SnO$_2$/rGO | Nanoparticles | Chemical solution | NH$_3$ | 5 ppm | 7.6$^\#$ | 7min/50min | ~5ppm | [365] |

| | | | | | | | | |
|---|---|---|---|---|---|---|---|---|
| Pd/TiO$_2$/rGO | Nanorods | One-pot polyol | NH$_3$ | 50 | 14.9# | 184 s/ 81 s | 2.4 ppm | [366] |
| Pd/RGO/TiO$_2$ | Nanotube | Electrochemical anodization | Methanol | 700 | ~70# | - | - | [367] |
| CNT/Au/SnO$_2$ | Nanotube | Chemical solution | CO | 2500 | 70 | - | - | [368] |
| WO$_3$/S/rGO | | Hydrothermal | NO$_2$ | 20 ppm | 149.5# | 6 s/56 s | 0.25 ppm | [369] |
| SnO$_2$/S/rGO | Hydrothermal | | NO$_2$ | 5 ppm | 20.31# | 40 s/357 s | 1ppm | [370] |

*Notes:*

*C = concentration;*

*t$_{res}$/t$_{rec}$ = response time /recovery time;*

*LOD = limit of detection;*

*Response is defined as Ra/Rg (for reducing gases) or Rg/Ra (for oxidizing gases), Ra: resistance of the sensor exposed to reference, Rg: resistance of the sensor exposed to target:*

*\* Here the response is defined as ΔR/Rg (for reducing gases) or ΔR/Ra (for oxidizing gases), ΔR: the change in resistance.*

*# Here the response is defined as (ΔR/Rg)×100% (for reducing gases) or (ΔR/Ra)×100% (for oxidizing gases).*
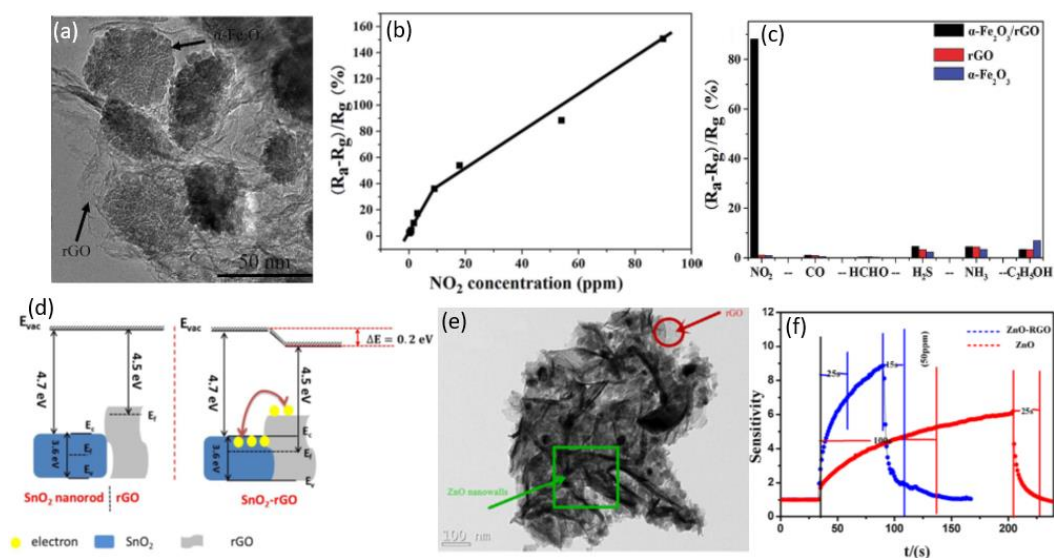


Fig. 23 (a) TEM image of the α-Fe$_2$O$_3$/rGO composite; (b) response values of the sensor based on α-Fe$_2$O$_3$/rGO at different NO$_2$ concentrations; (c) response histogram of the sensor to different gases. [330], © 2014 The Royal Society of Chemistry. (d) Band gap diagrams of SnO$_2$-nanorods/reduced graphene oxide nanostructures before and after combination. [344], © 2017 Elsevier. (e) TEM image of the ZnO/rGO composite; (f) response/recovery curves to 50 ppm NO$_2$ of the sensor based on a-ZnO/rGO or ZnO. [135], © 2017 Elsevier.

The RT $NO_2$ sensor fabricated using rGO/α-$Fe_2O_3$ [126] exhibits a response value of 3.86 to 5 ppm $NO_2$, which is better than that of pure rGO, whose response is 1.38. In addition, it has significantly shorter response/recovery times of 32/1432 s, compared wtih those of the sensors made of the pure rGO (2059s, 40130s). Dong *et al.* [330] reported a nanocomposite combining α-$Fe_2O_3$ nanosphere and reduced graphene oxide nanosheets as shown in Fig. 23a. The α-$Fe_2O_3$ nanospheres with a diameter from 40 to 50 nm were grown on the surface of graphene nanosheets using a hydrothermal method, and the improved sensing performance from the sensor made of this composite was attributed to the synergistic effect of a-$Fe_2O_3$/rGO and large specific surface areas. In addition to the interaction of $NO_2$ with $O_2^-$ on the surface of a-$Fe_2O_3$, $NO_2$ molecules also capture the electrons from the rGO to form $NO_2^-$, thus resulting in an increased hole density, and a decreased resistance of rGO. Therefore, the a-$Fe_2O_3$/rGO nanocomposites exhibit a much higher response to $NO_2$ at RT than that of either the pure rGO or a-$Fe_2O_3$ nanospheres. Its LOD for the $NO_2$ gas is as low as 0.18 ppm (see Fig. 23b), and a good selectivity has been demonstrated against CO, HCHO, $H_2S$, $NH_3$ and $C_2H_5OH$ (see Fig. 23c).

Besides the good conductivity of carbon materials, the improved interfacial electron transfer is another a key factor for improving the SMONs' sensing performance by adding carbon nanomaterials. For example, an RT $NH_3$ gas sensor was fabricated using $SnO_2$ nanorods/rGO composite nanostructures [344], and the sensor shows fast response/recovery with times of 8/13 s to 200 ppm $NH_3$ at RT. Fig. 23d shows the band gap diagrams of $SnO_2$-nanorods/rGO nanostructures before and after the combination of two nanostructures. The p-n heterojunctions are formed at the interface between the rGO and $SnO_2$ as the rGO is a p-type semiconductor. The Fermi energy of the rGO is higher than that of the $SnO_2$, so electrons can be transported to $SnO_2$ from the rGO, which can further enhance the adsorption of $NH_3$ molecules to improve the gas sensing performance.

Formation of heterojunction structures was found to contribute the sensing performance of the ZnO nanowall/rGO nanocomposite [135], in which the ZnO nanowalls

were vertically grown on the rGO thin film using a soft solution process to obtain a heterojunction structure as shown in Fig. 23e. At the interfaces between the rGO and ZnO nanowalls of the p-n heterostructures, the Fermi energy of the rGO is higher than that of the ZnO. Therefore, the charge transfer from rGO layers to the conduction band of ZnO enhances the adsorption of $NO_2$ molecules. If compared with the sensor made of pure ZnO nanowalls, the sensor made of the ZnO/rGO heterojunction shows a higher response and shorter response/recovery times to $NO_2$ at RT (see Fig. 23f) [135].

Another key mechanism for the improved gas sensing performance for the SMONs/rGO composite is the increased oxygen vacancy on the SMONs, such as in the $SnO_2$-rGO composite [329]. Due to the p-n heterojunction formed at the interfaces between n-type $SnO_2$ and p-type rGO, electrons can easily transfer from the $SnO_2$ into the rGO to form abundant oxygen vacancies on the surface of $SnO_2$. These oxygen vacancies are the electronic charge carriers to increase the conductivity of the composite, and they can adsorb oxygen molecules to form more active sites, which will capture electrons from $SnO_2$ and form the oxygen ions to react with target gas molecules. The oxygen vacancy also facilitates the fast adsorption of the $NO_2$ molecules onto the surface of $SnO_2$. All these reasons are contribute to the excellent sensing properties of $SnO_2$/rGO composite based sensors to $NO_2$ gas at RT.

However, the recovery of these composites of SMONs with carbon materials is very slow, although UV-light illumination can be used to enhance a fast and complete recovery. For example, rGO-$CeO_2$ hybrids were synthesized by anchoring small $CeO_2$ nanocrystals onto rGO nanosheets using a solvothermal method, and the RT $NO_2$ gas sensor made of this hybrid showed a full recovery time of several hours. [371] However, the recovery time can be significantly reduced to within 258 s with the aid of UV-light illumination. This UV light enhancement will be further discussed in Section 3.3.
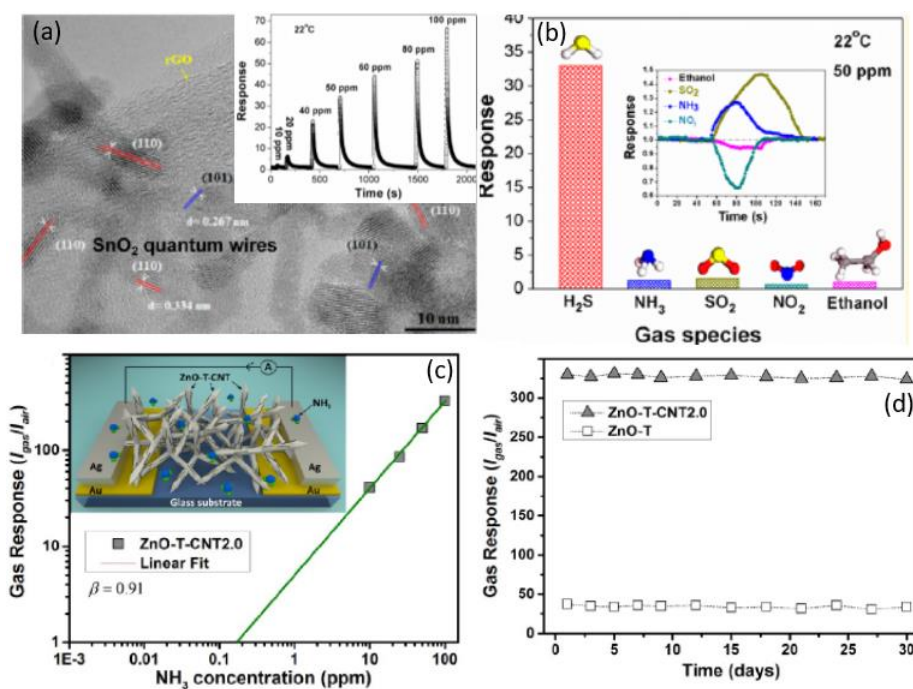
Fig. 24. (a) TEM image of the $SnO_2$ quantum wires/rGO nanosheets, the inset shows the response/recovery of the sensor based on $SnO_2$ quantum wires/rGO nanosheets for different $H_2S$ concentrations; (b) response histogram of the $SnO_2$ quantum wires/rGO nanosheets bases sensor to different gases. [4], © 2016 American Chemical Society. (c) Response values at different concentrations of $NH_3$ gas for 2%CNTs/ ZnO networks (the inset presents the sensor structure); (d) long-time stability of the RT gas sensors to 100 ppm of $NH_3$ at 30% RH. [348], © 2017 American Chemical Society.

Fig. 24a shows that an ultra-fast response time for sensing of $H_2S$ gas (which is the fastest reported in literature with a value of 2s to 50 ppm of $H_2S$) can be achieved using a sensor made of $SnO_2$ quantum wires/rGO nanosheets [4]. The electronic interactions of $SnO_2$ quantum wires and rGO nanosheets can enhance the electron transport [4], and increase the response and recovery speed. In addition, the sensor made of the $SnO_2$ quantum wires/rGO nanosheets shows a response of 33 with an excellent selectivity against other types of gases including $NH_3$, $SO_2$, $NO_2$ and ethanol at RT as shown in Fig. 24b. In this composite material, the ultrathin and one-dimensional microstructure of $SnO_2$ quantum wires is effective in providing large surface areas for gas adsorption and reaction.

The sensors made of composites integrating the rGO with p-type SMONs (such as CuO and $Co_3O_4$) also show enhanced sensing performance. The RT gas sensor based on the CuO/rGO nanohybrids can detect a low-concentration of $NO_2$ with a highly sensitive response (14 to 1 ppm $NO_2$) and fast response/recovery times (66 /34 s), mainly due to formation of large surface areas and enhanced carrier transfers between the CuO and $NO_2$ molecules [339]. Furthermore, Ding et al. reported that the integration of chemically functionalized three-dimension graphene oxide hydro-gels with metal-organic frameworks derived $Co_3O_4$ nanostructures achieved ultra-high response, short response time and distinct cross-selectivity [372].

The composite of SMONs with carbon nanotubes (CNT) such as SWCNTs/$SnO_2$ [373] and CNT/$SnO_2$ [374-377] can also improve the sensing performance [378]. The p-n junctions formed between the SMONs and p-type MWCNTs are responsible for their enhanced gas sensing responses. For example, Srivastava et al. [124] reported an RT $NO_2$ gas sensor based on multi-walled carbon nanotubes/$SnO_2$. The sensor exhibits a much higher response to $NO_2$ than the pure $SnO_2$ based sensor operated at RT. Due to the good conductivity of the CNTs and the high porosity of the ZnO networks [348], the response value of 2%CNTs/ZnO networks has been increased from 37 to 330 when the sensor was exposed to 100 ppm $NH_3$ at RT (see Fig. 24c). The response/recovery times are decreased from 58/61 s to 18/35 s, respectively. The sensor also displays a good stability at the RT over a duration of one month (see Fig. 24d). In addition, the CNTs can serve as acceptors for the released electrons, which are injected into the SMONs from the target gases. A $H_2S$ gas sensor made of nanocomposite of $SnO_2$ quantum dot/MWCNT based $H_2S$ gas sensor reported by Liu et al. [379] exhibited a high response value of 108 to 50 ppm $H_2S$ with fast response/recovery times of 23/44 s.

Adding the metal noble nanoparticles into the composite is another method to further improve the gas sensing performance of SMONs/rGO composite. Being good catalysts, these noble metal nanoparticles can enhance the catalytic efficiency by creating extra new sites to promote fast adsorption of gas molecules and decrease the reaction temperatures by lowering the activation energy of the gas sensing reactions. For example, Shojaee et al. [362] reported that the nanocomposites of Pd loaded $SnO_2$ and

partially reduced graphene oxide showed a good performance to detect CO from 50 to 1600 ppm with fast response and recovery times at 26 °C. The Pd/SnO$_2$/rGO based H$_2$ sensor [361] and Pd/TiO$_2$/rGO based NH$_3$ sensor [366] prepared using a chemical solution method exhibited higher sensitivity and faster response time than those of the SnO$_2$/rGO and TiO$_2$/rGO sensors. In addition of Pd nanoparticles, Ag nanoparticles were also be used to improve the RT sensing performance of SnO$_2$-rGO hybrids for detection of NO$_2$. The Ag/SnO$_2$/rGO hybrid composites exhibits much shorter response time and recovery time (49 s and 339 s) to 5 ppm NO$_2$ at RT than those of the SnO$_2$-rGO hybrids (415 s and 740 s) [364].

Similar to those cases for the rGO/SMONs composites, modifications of the CNT/SMONs composites using noble metal nanoparticles can also improve their gas sensing property. For example, CNT/Au/SnO$_2$ composites were synthesized by homogeneously coating SnO$_2$ and Au nanocrystals onto the CNTs, and then applied to detect CO gas at RT [368]. The sensor made of the CNT/Au/SnO$_2$ composites shows a better selectivity to the CO than that of the CNT/SnO$_2$ composite. It has a high sensitivity of 70 when exposed to 2500 ppm of CO, and shows a higher sensitivity values to CO gases with different concentrations varied from 500 to 2500 ppm when compared with those of the Au/SnO$_2$ composites.

In brief, due to the high conductivity of carbon nanomaterials and the formation of heterojunction, the response/recovery times of the composites of SMONs with carbon nanomaterials are much shorter than those from the pure SMONs, although it seems that the increase of response values achieved using these composites might be less significant.

### 3.3 Room temperature photoactivated gas sensors based on semiconducting metal oxide nanostructures

Generally, many of the SMONs-based gas sensors are needed to heat up for the best gas sensing performance, which is inconvenient in many situations. Instead, UV light can be used to activate and enhance the gas sensing performance of SMONs operated at RT [380]. The reported SMONs whose sensing properties can be improved by UV light are mainly ZnO [381-385], In$_2$O$_3$ [386] [387], TiO$_2$ [388] [389] and SnO$_2$ [390, 391], which have been

summarized in Table 7. The SMONs can absorb the UV light to produce photo-generated electrons and holes. The photo-generated electrons on the surface can enhance the chemisorption of oxygen molecules to form more $O_2^-$ as listed in the Eq. (20) and (21) [392], thus can enhance the sensitivity and response/recovery times of the SMONs under the UV light.

$$h\upsilon \rightarrow h^+ + e^- \tag{20}$$
$$O_2 + e^-_{\ (h\upsilon)} \rightarrow O_2^-_{\ (h\upsilon)} \tag{21}$$

Table 7 Room temperature sensing properties of semiconducting metal oxide nanostructures enhanced by UV light

| Material | Structure | Synthesis method | Target gas | C (ppm) | Response | $t_{res}/t_{rec}$ | LOD | Ref. |
|---|---|---|---|---|---|---|---|---|
| ZnO | Microwires | Surface etching | $NO_2$ | 20 | 411[#] | 221/118 s | ~10 ppm | [381] |
| ZnO | Nanowires | Wet-chemical | $C_2H_5OH$ | 700 | 85[#] | - | ~100 ppm | [382] |
| ZnO | Nanorods | Hydrothermal | HCHO | 110 | 11.5[*] | 14/0.5 min | 1.8 ppm | [383] |
| ZnO | Nanofibers | Electrospinning | HCHO | 100 | 12.3 | 32/17 s | ~5 ppm | [384] |
| $In_2O_3$ | Nanostructures | Arc-discharge | NO | 50 | 41.7 | ~10/- min | ~2 ppm | [386] |
| $In_2O_3$ | Nanoporous particles | Nanocasting | Ozone | 0.22 | 200 | 2.5/- min | 50 ppb | [387] |
| $TiO_2$ | Hollow microspheres | Hydrothermal | HCHO | 5 | ~40 | 40/55 s | 124 ppb | [388] |
| $TiO_2$ | Thin film | Rf-sputter | $NO_2$ | 250 | ~1.8[#] | 100/210 s | 100 ppm | [389] |
| $SnO_2$ | Nanowires | - | $NO_2$ | 10 | ~85[#] | 10/15 min | ~0.1 ppm | [390] |
| $ZnO/SnO_2$ | Nanorods | Wet chemical | $NO_2$ | 0.5 | 1266[*] | 7/8 min | ~200 ppb | [393] |
| $SnO_2/TiO_2$ | Hollow spheres | Thermal evaporation | Ethanol | 100 | 160 | 50/150 s | - | [394] |
| $NiO/TiO_2$ | Microspheres | Hydrothermal | $NH_3$ | 100 | 140[#] | ~400/~400 s | ~10 ppm | [395] |
| Ag/ZnO | Nanorods | Hydrothermal | HCHO | 40 | 119.8[#] | - | 5 ppm | [396] |
| ZnO | Nanoparticles | Hydrothermal | $NO_2$ | 20 | 85[*] | 26/16 s | ~1 ppm | [397] |

*Notes:*

*C = concentration;*

$t_{res}/t_{rec}$ *= response time /recovery time;*

*LOD = limit of detection;*

*Response is defined as Ra/Rg (for reducing gases) or Rg/Ra (for oxidizing gases), Ra:*

*resistance of the sensor exposed to reference, Rg: resistance of the sensor exposed to target:*
*\* Here the response is defined as ΔR/Rg (for reducing gases) or ΔR/Ra (for oxidizing gases), ΔR: the change in resistance.*
*# Here the response is defined as (ΔR/Rg)×100% (for reducing gases) or (ΔR/Ra)×100% (for oxidizing gases).*

With the assistance of the UV LED (photon energy of 2.5 mW), the RT gas sensor made of mesoporous hollow $TiO_2$ microspheres [388] exhibited a high response to formaldehyde with faster response/recovery (40/50 s) and good selectivity. Higher response has also been reported using the sensor made of $ZnO/SnO_2$ composite materials [393] to detect $NO_2$ under the UV light illumination at RT. After the sensing materials is exposed to $NO_2$ gas, the $NO_2$ molecules will collect the photo-generated electrons to form the NO and $O_2^-$ as shown in Eq. (22) [397], which results in an increase in the resistance of the sensor.

$$2NO_{2\,(g)} + e^-_{\,(h\upsilon)} \rightarrow 2NO_{\,(h\upsilon)} + O_2^-_{\,(h\upsilon)} \tag{22}$$
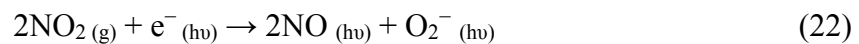
Simultaneously, a heterojunction is formed at the interfaces between ZnO and $SnO_2$. The photogenerated electrons are transferred from the ZnO to $SnO_2$ due to the higher Fermi energy level of ZnO than that of $SnO_2$ (see Fig. 25a). The efficient charge separation increases charge concentrations on the surface of $SnO_2$, which remarkably improves the sensitivity under the UV light stimulation at RT as shown in Figs. 25b.
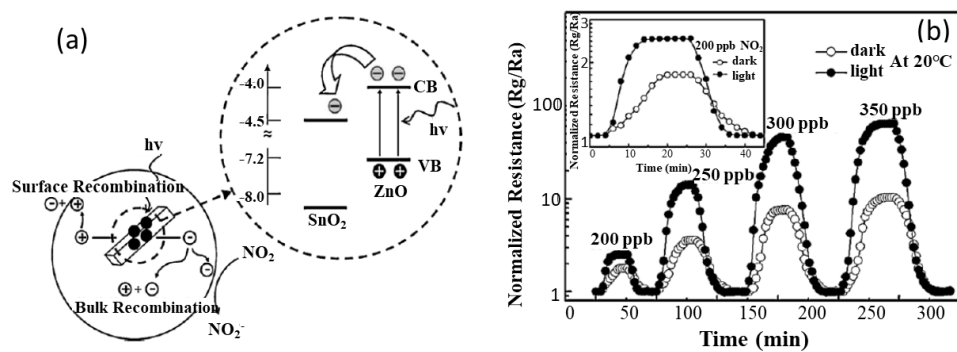


Fig. 25. (a) Schematic diagram of the carrier transport under UV light and the electron-hole pair separation on heterostructure of $ZnO/SnO_2$ composite; (b) Response/recovery of $ZnO/SnO_2$ composite at different concentration of $NO_2$ with and without UV light stimulation at room temperature. [393], © 2011 Elsevier.

Apart from the UV light, visible light (including blue light and white light) assisted RT gas sensors with enhanced performance have also been reported [387, 398-400]. Klaus *et al.* [387] reported a blue light (460 nm) activated ozone gas sensor based on nanoporous $In_2O_3$ particles, which showed a high response value of 200 and a low LOD of 50 ppb at RT. Geng *et al.* [399] reported that a sensor made of $CuxO_{1-y}/ZnO_{1-\alpha}$ nanocomposites showed enhanced $NO_2$ sensing properties at RT with high response and good selectivity after illuminated with the white light. Similarly, infrared (IR) should also be beneficial for the improvement in the sensing performance.

Although the photoactivated SMONs gas sensors could achieve the improved gas sensing performance operated at RT, the light-emitting diodes, UV source, or infrared light, as well as optical power detection device are necessary to be used, which will increase the size and production cost of the sensor device. The integration and shrinkage of the devices along with mass production capabilities are challenges. In addition, for the application of the gas sensors in the real environment, the gas sensor will be exposed in the air for real-time monitoring. The sunlight will severely influence the gas sensing response.

## 4. Mechanically flexible gas sensors based on semiconducting metal oxide nanostructures

Mechanically flexible gas sensors are in a great demand due to their promising applications in wearable electronic devices. The SMONs with a potentially higher carrier mobility and mechanical robustness are good candidates to the realization of stretchable and flexible sensors [223]. The mechanically flexible and wearable RT gas sensors based on the SMONs have been an active research area recently as listed in Table 8. Compared with those on the rigid substrates, the wearable devices need substrates which are flexible, light weight, transparent, transportable, with a small volume, and low cost [401]. Due to their excellent dielectric properties, and thermal and chemical stability, many plastic substrates have been used as flexible substrates for the RT gas sensors including polyethylene terephthalate (PET) [223, 402-404], polypropylene (PP) [405, 406], polyimide (PI) [265, 407, 408], Polyvinyl Acetate (PVA) [105] and nylon [409].

Table 8 Sensing performance of room temperature flexible gas sensor based on semiconducting metal oxide nanostructures

| Material | Structure | Substrate | Synthesis method | Target gas | C (ppm) | Response | $t_{res}/t_{rec}$ | LOD | Ref |
|---|---|---|---|---|---|---|---|---|---|
| CuO | Nanorectangles | PET | Hydrothermal | $NH_3$ | 5 | ~0.25* | 90/120 s | 5 ppm | 223 |
| ZnO | Nanorods | Nylon | Hydrothermal | $H_2$ | 500 | 109# | 149/122 s | - | 409 |
| ZnO | Nanowire | PET | Hydrothermal | $H_2$ | 1000 | 5# | ~600/- s | - | 402 |
| Ag/ZnO | Nanorods | PI | Hydrothermal | $C_2H_2$ | 1000 | 26.2 | 66/68 s | 3 ppm | 410 |
| Ga/ZnO | Nanorods | PI | Hydrothermal | $H_2$ | 1000 | 91# | ~18.8/- s | 0.2 ppm | 265 |
| Pd/ZnO | Nanorods | PI/PET | Hydrothermal | $H_2$ | 1000 | 91.2# | ~18.8/- s | 0.2 ppm | 173 |
| $ZnO_{1-x}$ | Sheet-like | PP | Suspension flame spraying | $NO_2$ | 1 | 2.568* | 60/230 min | 0.25 ppm | 405 |
| ZnO | Nanoparticles | Cotton fabrics | Sol-gel | $NH_3$ | 100 | 9 | 39/34 s | - | 411 |
| In/Ga/Zn/Oxide | Thin-Film | PI | CVD | $NO_2$ | 5 | ~1.3 | - | 2 ppm | 407 |
| $PdO/Co_3O_4$ | Nanocube | PI | Chemical precipitation | $NO_2$ | 20 | 27.33# | - | 1 ppm | 408 |
| $SnO_2/SnS_2$ | Nanotube | PET | Hydrothermal | $NH_3$ | 100 | 2.48 | 21/110 s | 1 ppm | 403 |
| $CeO_2/CuBr$ | Nanoparticles | PI | Electronbeam evaporation | $NH_3$ | 5 | 68 | 112/74 s | 20 ppb | 412 |
| Polyaniline/$CeO_2$ | Thin film | PI | Self-assembly | $NH_3$ | 50 | 262.7# | 14/6 min | 16 ppb | 413 |
| $WO_{3-\delta}$ | Film | PI | Granule spray | $NO_2$ | 10 | 18500# | 17/25 s | 1.88 ppm | 414 |
| Polyaniline/$WO_3$ | Flowerlike | PET | Polymerization | $NH_3$ | 10 | 7 | 13/49 s | 500 ppb | 415 |
| rGO/$WO_3$ | Nanoneedle | PET | Hydrothermal | Isopropanol | 200 | ~8.5 | 60/- s | 1 ppm | 404 |
| MWCNTs/$WO_3$ | Nanoparticle | PET | Hydrothermal | $NO_2$ | 5 | 14# | 10/27 min | 0.1 ppm | 416 |
| $WO_3$/MWCNT/rGO | Nanoparticle | PI/PET | Hydrothermal | $NO_2$ | 5 | 17# | 7/15 min | 1 ppm | 417 |
| SWNT/$Fe_2O_3$ | Composite | PP | CVD | $NO_2$ | 100 | 18.3# | - | ~1 ppm | 406 |
| Polyaniline/$\alpha$-$Fe_2O_3$ | Fiber network | PET | Sol-gel | $NH_3$ | 100 | 72# | 50/1575 s | 2.5 ppm | 418 |
| Cellulose/$Fe_2O_3$ | Nanoparticle | PET | Hydrothermal | $NO_2$ | 200 | ~1100# | 50/30 s | 1 ppm | 419 |
| $In_2O_3$ | Cubic crystals | PVA | Hydrothermal | Ethanol | 100 | ~1.4 | 5/3 s | 10 ppm | 105 |
| Au/$In_2O_3$/Polyaniline | Nanospheres | PI | Hydrothermal | $NH_3$ | 100 | 46 | 118/144 s | - | 420 |

*Notes:*

61

*C = concentration;*

*t_res/t_rec = response time /recovery time;*

*LOD = limit of detection;*

*Response is defined as Ra/Rg (for reducing gases) or Rg/Ra (for oxidizing gases), Ra: resistance of the sensor exposed to reference, Rg: resistance of the sensor exposed to target:*

*\* Here the response is defined as ΔR/Rg (for reducing gases) or ΔR/Ra (for oxidizing gases), ΔR: the change in resistance.*

*# Here the response is defined as (ΔR/Rg)×100% (for reducing gases) or (ΔR/Ra)×100% (for oxidizing gases).*

For many of these flexible RT gas sensors, a sensitive layer such as ZnO nanorods is often used to deposit onto the device, for example, ZnO nanorods/nylon [409], Ga-ZnO naorods/PI [265], Pd-ZnO nanorods/PI/PET [173]. The aqueous solution method to prepare these ZnO nanorod layers on the polymer substrate is facile with advantages of low growth temperature and easy modifications. For example, Mohammad *et al.* [409] prepared well-aligned ZnO nanorods on a thin nylon substrate with a thickness of 15 μm using a hydrothermal process, and then made $H_2$ gas sensor. There are many contact points among ZnO nanorods which form paths of electric carriers and result in the improvement of electron transport. The mechanically flexible hydrogen gas sensor exhibited a good response value of 109% (defined as (ΔR/Rg)×100%) with fast response/recovery.
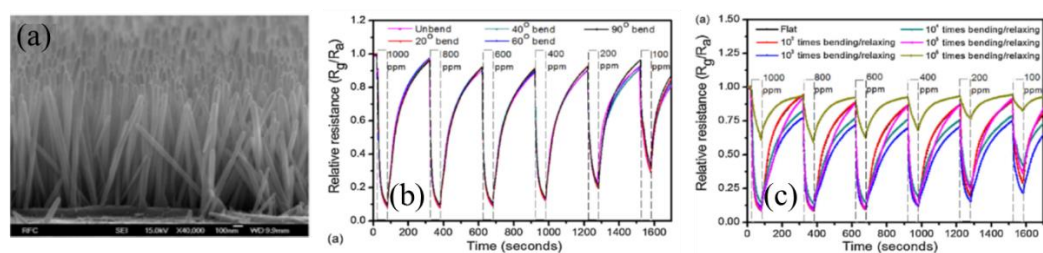


Fig. 26. (a) SEM images of Pd/ZnO nanorods after $10^3$ times bending/relaxing. (b) response/recovery curves of the flexible sensor to $H_2$ at different bending angles (c) the reliability test of the flexible sensor. [173], © 2013 Elsevier.

Rashid *et al.* [173] prepared vertically aligned ZnO nanorods on the PI substrate using a hydrothermal method, and then made the sensors for hydrogen detection at RT. Pd nanoparticles with 10 nm in size were further sputtered on the surface of ZnO nanorods

using an RF magnetron sputtering. After bent for $10^3$ cycles, there were no cracks or breaks on the ZnO nanorod film (see Fig. 26a). Such the flexible hydrogen sensors had a response value ~91% (defined as $(\Delta R/Rg) \times 100\%$) for 1000 ppm hydrogen with good repeatability and stability, and a low LOD of 0.2 ppm at RT. The gas sensing performance at different bent angles from 0°, to 90° did not exhibit apparent changes (see Fig. 26b). Even after the sensor was bent to the curvature angle of 90° for $10^5$ cycles, the sensing performance of this flexible $H_2$ sensor did not show any degradation (see Fig. 26c). The vertically well-aligned ZnO nanorods with the Pd catalyst on Ga-modified ZnO seed layer on flexible PI substrate also showed good $H_2$ sensing properties and good mechanical flexibility at RT with good repeatability, stability and low LOD of 0.2 ppm, even after bent at a curvature angle of 90° [265].

In addition to being directly grown onto the plastic substrates, the ZnO nanowires were also transferred onto plastic substrates of PET to fabricate a flexible gas sensor using various methods, including slide transfer, roll transfer and heat transfer [402]. 2D sheet-like ZnO layer was deposited onto the flexible polypropylene papers using a suspension flame spraying method, and the prepared ZnO flexible sensor exhibited good responses and stability to sub-ppm level of $NO_2$ at RT under white LED light illumination [405].

The other types of SMONs have also been applied for making the flexible RT gas sensors, and these include $WO_3$, $SnO_2$, $CeO_2$, $Co_3O_4$, $In_2O_3$, etc. For example, Ryu *et al.* [414] fabracted flexible RT $NO_2$ gas sensors based on a $WO_3-\delta$ film on a plastic substrate of polyimide (PI) using granule spray method with a vacuum process. The sensor has a repsonse up to 18500% to 10 ppm $NO_2$ with fast response/recovery times of 17/25 s and reliable flexibility after 4000 bending/extending cycles. For anotehr example, a nanocompsite of polyaniline and nonoflower-like $WO_3$ synthesized using a facile chemicaloxidation polymerization precess was prepared on the PET substrate to fabricate a $NH_3$ flexible sensors, which shows high response and fast response/recovery times (13/49 s) to 10 ppm $NH_3$ operated at RT [415].

Modifying the SMONs using the polyaniline (PANI) can effectivly enhance the sensing performance and stable of the flexible gas sensors, such as PANI-$CeO_2$,

PANI/α-Fe$_2$O$_3$ and PANI/WO$_3$. The morphology and sensing performance of flexible RT NH$_3$ gas sensors based on PANI-CeO$_2$ nanocomposite thin film are stable after bent/cycled for 500 times [413]. Furthermore, adding the noble metals into the SMONS/PANI composites can further improve its RT sensing performance. For examples, after adding the Au nanoparticles, the response of the RT NH$_3$ gas sensor made of the composite of mesoporous In$_2$O$_3$ nanospheres/polyaniline has been increased up to 4 times higher [420].
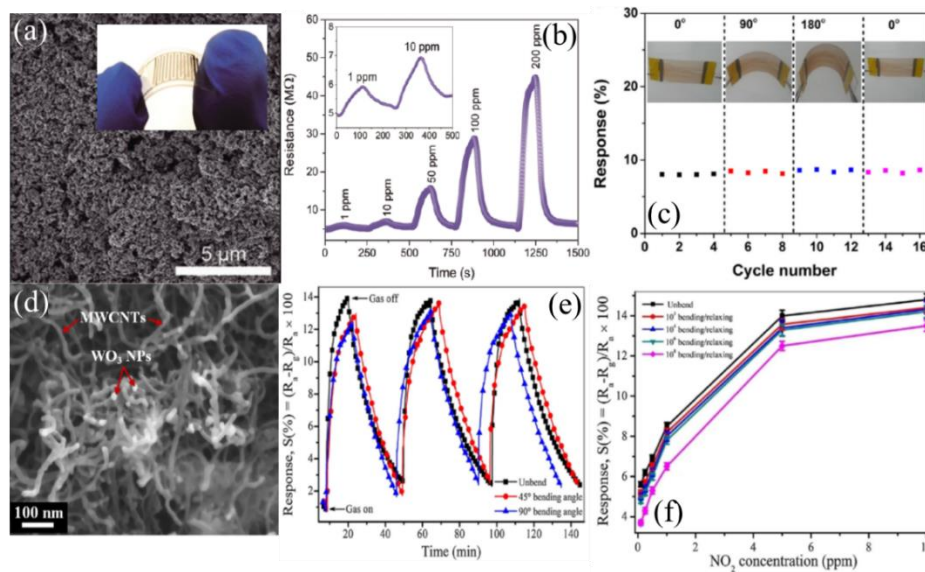


Fig. 27. (a) SEM images of 5%rGO/WO$_3$□0.33H$_2$O deposited on polyethylene terephthalate, the inset is the photograph of the flexible gas sensor, (b) response/recovery curves to isopropanol with different concertation. [404], © 2018 Royal Society of Chemistry. (c) Responses of the SWNT/Fe$_2$O$_3$ gas sensor to 20 ppm H$_2$S under different bending angles from 0° to 180° and returned to 0°. [406], © 2017 Elsevier. (d) SEM images of the MWCNTs/WO$_3$ composite, (e) response curves to 5 ppm NO$_2$ at RT under different bending angles, (f) responses to different NO$_2$ concentration at RT after bending/relaxing several times (90° angle). [416], © 2015 Elsevier.

Graphene and carbon nanotubes have excellent performance during severe plastic deformation, thus the composite integrating these carbon nanomaterials with the SMONs can achieve excellent sensing performance and mechanical flexibility. For

example, a flexible isopropanol sensor was fabricated using a mixture of WO$_3$□0.33H$_2$O nano-needles and rGO on PET substrates (see Fig. 27a) [404]. Compared with the sensor made on the pure WO$_3$□0.33H$_2$O nano-needles, the 5%rGO/WO$_3$□0.33H$_2$O based sensor showed a better selectivity and a superior response (4.96 to 100 ppm to isopropanol) (see Fig. 27b), with a good performance after repeated bending for many cycles. Similarly, SWNT-Fe$_2$O$_3$ composite films were prepared using CVD method and then transferred onto the flexible PP polymer substrate [406]. Compared that fabricated using the single SWNTs, the flexible gas sensor of the SWNT-Fe$_2$O$_3$ composite film exhibited an improved response to H$_2$S at RT. Under repeated bending to large angles (such as 90∘ and 180∘) for 16 times as shown in Fig. 27c, the flexible sensor exhibited stable sensing response values to H$_2$S. For another example, hydrothermally synthesized WO$_3$ nanoparticles were mixed with MWCNTs (see Fig 27d), and then casted onto a PET substrate to fabricate a flexible NO$_2$ gas sensor [416]. This sensors not only shows a good sensing performance, but also has an excellent mechanical flexibility (see Fig. 27e). There was no significant degradation of response values after bending/ relaxing for 10$^6$ cycles, demonstrating the excellent mechanical robustness of the MWCNTs/WO$_3$ composite layers on the flexible gas sensors (see Fig. 27f).

Cotton fabrics are also reported to be used as a good substrate for the flexible RT gas sensor, for example, a flexible NH$_3$ gas sensor was made by growing the nanostructured ZnO onto the cotton fabrics [411]. Flexible nanowires of the SMONs can also be isostatically pressed into a thin paper, and then the nanowire paper is cut into small pieces to directly fabricate flexible gas sensor. Based on this idea, a-MoO$_3$ nanowires paper [421] have been fabricated and a flexible gas sensor was made to detect hydrogen gas. The sensor shows fast response and recovery speeds (3.0 and 2.7 s toward 1.5% H$_2$), good selectivity, and high sensitivity at RT. Wei et al. [422] also reported a flexible gas sensors based on cellulose/TiO$_2$/PANI composite nanofibers, which showed an excellent ammonia gas sensing performance at RT. Similarly, a stretchable ZnO nano-accordion structures has also shown its good applications in flexible RT gas sensors [423].

In summary, the flexible RT gas sensors can be fabricated using the SMONs as the

sensing materials onto a mechanically flexible platform, and the sensors have demonstrated excellent mechanical robustness and can maintain good sensing performance at RT after bending/recovering many times. Furthermore, the composite of SMONs with graphene or CNT can achieve better mechanical robustness for the flexible gas sensor. However, so far, the sensing performance of the flexible RT gas sensors and reliability and stability have not achieved excellent performance as those of the rigid counterparts.

## 5. Conclusions and outlook

In this paper, we have summarized the recent progress on designs and mechanisms of RT gas sensors based on the different SMONs. Our emphasis has been on the critical review of different structures of SMONs-based gas sensors that may help the design of new devices. The key topics covered in this paper include: single phase n-type SMONs, single phase p-type SMONs, noble metal nanoparticles modified SMONs, metal ion modified SMONs, SMONs composites with multiple metal oxides, and the SMONs composites with carbon nanomaterials. The different nanostructures of these SMONs include nanoparticles, nanowires, nanofibers, nanorods, nanosheets, nanotubes etc. Sensing performance of these SMONs based RT sensors have been reviewed for detecting various toxic or flammable gases, such as hydrogen disulfide, nitrogen dioxide, ammonia, carbon monoxide and hydrogen, as well as organic gas of formaldehyde, acetone, methanol and ethanol, etc. In addition, the photoactivated RT gas sensors and flexible RT gas sensors based on SMONs are also summarized.

Availability of numerous surface chemisorbed oxygen species of $O_2^-$ at the RT was identified to be the key reason for the high sensitivity of these RT gas sensors. These oxygen species react with the target molecules to change the electronic resistance of the sensor. However, many RT $H_2S$ sensors are exceptional as the sensing mechanism is dominant by the formation of metallic conducting metal sulfide.

Noble metal nanoparticles on the surface of SMONs can stimulate the adsorption of oxygen molecules to form oxygen ions by the reduction processes. These oxygen ions spill onto the surface of SMONs to improve the concentration of oxygen ions on the

surface of SMONs for sensing reaction. In addition, noble metal nanoparticles can accelerate the transfer of electrons to SMONs. Therefore, both the chemical sensitization and electronic sensitization enhance the sensitivity and speed of the SMONs-based sensors. Doping of metal ions in the SMONs can increase the number of active sites and defects on the surface of SMON nanocrystals, thus enhance the amount of oxygen species and increase the adsorbed gas molecules on the sensor surface. Heterojunctions can form at the interfaces of different etal oxides or at the interfaces between the SMONs and carbon nanomaterials. These can effectively accelerate the transformation of electrons and enhance oxygen adsorption, and are beneficial to improve the sensitivity and response rates in application of RT gas sensors. The sensing performance also depends significantly on the nanostructures of the SMONs. Large specific surfaces are beneficial to the formation of more oxygen species, and porous nanostructures facilitate the adsorption and desorption of target gases, thus achieving fast response and recovery.

Generally, the RT SMONs based gas sensors show high response values and low LODs, however, their response and recovery times could be too long. Modifications of the SMONs sensors using various methods can improve their sensing performance, which include using: the noble metal modified SMONs; the metal ion doped SMONs, the composite SMONs, and the composite with carbon nanomaterials. The key conclusions are summarized below:

(1) Surface modifications of the SMONs using noble metal nanoparticles can effectively enhance their sensitivity, response/recovery speeds, selectivity and LODs through both chemical sensitization and electronic sensitization.

(2) Metal ion doped SMONs have increased number of active sites and more defects on their surfaces, which can enhance the oxygen species for sensing reactions and improve the adsorption of gas molecules.

(3) SMON composites can form abundant oxygen vacancies on their surfaces, thus providing many active sites. Heterojunctions can be formed at the interfaces of different metal oxides, which can effectively accelerate the transformation of electrons between different particles, thus improving the response rates. The

composite SMONs often contain numerous mesopores which are beneficial to the adsorption and desorption of gas molecules. Hence, sensors based on the majority of reported composite oxides exhibit high response value and very fast response.

(4) Because of the high conductivity of carbon nanomaterials, the composites of SMONs combined with carbon nanomaterials can achieve fast response/recovery.

(5) The photo-generated electrons on the surfaces of SMON sensing materials can enhance the chemisorption of oxygen molecules to form more $O_2^-$, which can enhance the sensitivity and response/recovery speed of the SMONs.

(6) RT flexible gas sensors based on the sensing layer of the SMONs sensing materials have the excellent mechanical robustness and can maintain good sensing performance after repeated bending/recovering.

Although up there has been significant progress in developing novel SMONs for gas sensing at RT, there are still many challenges and problems towards achieving high response, fast response/recovery speed, good selectivity and long-term stability:

(1) One of the key challenges is the durability and long-term stability of the sensors for application in varying environmental conditions, such as different humidity levels and different temperatures, which could cause significant influences for the sensing properties of many RT gas sensors. This is especially important for RT $NH_3$ sensing, as high humidity seriously affects the sensitivity and the response time. Light exposure, especially ultraviolet lights and infrared, and even visible lights, all influence the response of the RT SMONs sensors. In the literature, the performance of sensors has been normally characterized based on experiments conducted in well-controlled laboratory environment. However, in a practical setting with variable environmental conditions, the sensing performance may be altered with light exposure. Therefore, the sensing properties under different environmental conditions should be systematically investigate in order to establish the relationship between environmental conditions and sensing properties, which are then used to correct the sensing results.

(2) Interfering gases often affect the sensing performance, resulting in a drastically reduced response. Lack of good selectivity is still the most serious problem

hindering the wide applications of these RT gas sensors. There are few reports of the specific gas sensors which only respond to a target gas but not all the other gases. Because the resistive gas sensors are relied on their changes of resistance upon adsorption of gas molecules, it can distinguish between the reducing gases and oxidizing gas based on the increase or decrease of resistance, however, it is difficult to discriminate a group of gases which can produce the similar changing trends of resistance values.

Therefore, selectivity is particularly important for multiple-agent gas sensors. To solve this problem, arrays of different sensing materials can be fabricated such that forming an array of gas sensors, which could obtain good selectivity by analyzing and comparing data from the different single sensors [424]. For example, Zhang e*t al.* [425] reported a method to detect multiple VOCs using an array of gas sensors based on Ag doped $LaFeO_3$ (ALFO). The device was optimized for the detection of acetone, benzene, methanol and formaldehyde to monitor air quality. The selectivity of ALFO can be altered using a molecular imprinting technique towards specific targets. Responsivity values of individual sensing elements vary between 14 and 21 while the values to other VOCs are lower than 4. The response and recovery times are on the order of 10 s and 100 s levels. Flitti *et al.*[426] reported a micromachined 4×4 array of sensors for multiple target detection. The sensing film for individual elements is based on $SnO_2$ and the elements are post-treated using metal catalysts of Pt, Pd, and Au and ion implanted using B, P, and H. The basic post-treatment methods are effective to selectively detect gases of CO, $CH_4$, Ethanol, $CH_4$-CO, Ethanol-CO, and Ethanol-$CH_4$ using an algorithm based on a vector angle similarity. Recognition accuracy higher than 95% is reported in this study [427]. This method has been demonstrated being capable of forming 12,000 virtual sensors using dedicated temperature modulations. Sensing network will be the future trends.

(3) The sensing mechanism of the SMONs is mainly based on the interaction between the target gas molecules and chemisorbed oxygens species, such as $O_2^-$, $O^-$ and $O^{2-}$ ions. However, other oxygen groups such as $OH^-$ can also react with the target gas

molecules. More effective analysis and theory development of the surface groups is urgently needed to assess its effect on the sensing properties, and the surface modification methods should be developed to minimize this influence.

(4) Many gas sensing mechanisms of SMONs based materials with various sizes and morphologies have been presented to explain their sensing properties. However, it is not clearly elucidated why the same SMON based materials with similar sizes and morphologies show remarkably different sensing properties. Therefore, *in situ* characterization techniques and theory development for the sensing mechanisms are necessary.

(5) Response times of many RT gas sensors is very long, which cannot meet the need for timely triggering of the alarm. Exploring novel SMONs based sensing materials for rapid response at RT is still necessary. 3-D nano-arrays of SMONs facilitate the gas diffusion, which might be promising to shorten the response time.

(6) Flexible wearable RT gas sensors are in a great demand due to their promising applications. The SMONs with a potential of higher carrier mobility and mechanical robustness, are one of the good candidates for making the stretchable and flexible gas sensors. For RT gas sensors, there is still challenges for their manufacturing technologies, and cracking and spalling problems of SMONs layers on the flexible substrates usually happen, which need to be solved to achieve reliable RT flexible gas sensors. Therefore, finding new low-cost SMONs based sensing materials with excellent sensing performance and mechanical robustness is still the major challenge.

## Conflicts of interest

There are no conflicts to declare.

## Acknowledgements

**Uncategorized References**

1.      M. Jerrett, D. Donaire-Gonzalez, O. Popoola, R. Jones, R. C. Cohen, E. Almanza, A. de Nazelle, I. Mead, G. Carrasco-Turigas, T. Cole-Hunter, M. Triguero-Mas, E. Seto and M. Nieuwenhuijsen, *Environ Res*, 2017, **158**, 286-294.

2.      Z. A. Barakeh, P. Breuil, N. Redon, C. Pijolat, N. Locoge and J.-P. Viricelle, *Sensors and Actuators B: Chemical*, 2017, **241**, 1235-1243.

3.      D. Sett and D. Basak, *Sensors and Actuators B: Chemical*, 2017, **243**, 475-483.

4.      Z. Song, Z. Wei, B. Wang, Z. Luo, S. Xu, W. Zhang, H. Yu, M. Li, Z. Huang, J. Zang, F. Yi and H. Liu, *Chemistry of Materials*, 2016, **28**, 1205-1212.

5.      H. Ren, C. Gu, S. W. Joo, J. Zhao, Y. Sun and J. Huang, *Sensors and Actuators B: Chemical*, 2018, **266**, 506-513.

6.      G. Tuerdi, P. Nizamidin, N. Kari, A. Yimit and F. Wang, *RSC Advances*, 2018, **8**, 5614-5621.

7.      A. Paliwal, A. Sharma, M. Tomar and V. Gupta, *Sensors and Actuators B: Chemical*, 2017, **250**, 679-685.

8.      B. Gong, T. Shi, W. Zhu, G. Liao, X. Li, J. Huang, T. Zhou and Z. Tang, *Sensors and Actuators B: Chemical*, 2017, **245**, 821-827.

9.      R. Kitture, D. Pawar, C. N. Rao, R. K. Choubey and S. N. Kale, *Journal of Alloys and Compounds*, 2017, **695**, 2091-2096.

10.     M. Asad and M. H. Sheikhi, *Sensors and Actuators B: Chemical*, 2014, **198**, 134-141.

11.     S.-H. Wang, C.-Y. Shen, H.-M. Huang and Y.-C. Shih, *Sensors and Actuators A: Physical*, 2014, **216**, 237-242.

12.     L. Rana, R. Gupta, M. Tomar and V. Gupta, *Sensors and Actuators B: Chemical*, 2017, **252**, 840-845.

13.     T. Goto, T. Itoh, T. Akamatsu, N. Izu and W. Shin, *Sensors and Actuators B: Chemical*, 2016, **223**, 774-783.

14.     L. Sun, W. L. Luan, T. C. Wang, W. X. Su and L. X. Zhang, *Nanotechnology*, 2017, **28**, 075501.

15.     H. Liang, X. Zhang, H. Sun, H. Jin, X. Zhang, Q. Jin, J. Zou, H. Haick and J. Jian, *ACS Sens*, 2017, **2**, 1467-1473.

16.     G. Jiang, M. Goledzinowski, F. J. E. Comeau, H. Zarrin, G. Lui, J. Lenos, A. Veileux, G. Liu, J. Zhang, S. Hemmati, J. Qiao and Z. Chen, *Advanced Functional Materials*, 2016, **26**, 1729-1736.

17.     E. Menart, V. Jovanovski and S. B. Hočevar, *Sensors and Actuators B: Chemical*, 2017, **238**, 71-75.

18.     S. S. Shendage, V. L. Patil, S. A. Vanalakar, S. P. Patil, N. S. Harale, J. L. Bhosale, J. H. Kim and P. S. Patil, *Sensors and Actuators B: Chemical*, 2017, **240**, 426-433.

19.     Y. Li, N. Chen, D. Deng, X. Xing, X. Xiao and Y. Wang, *Sensors and Actuators B: Chemical*, 2017,

**238**, 264-273.

20.    R. Kumar, O. Al-Dossary, G. Kumar and A. Umar, *Nano-Micro Letters*, 2014, **7**, 97-120.

21.    A. Dey, *Materials Science and Engineering: B*, 2018, **229**, 206-217.

22.    S. W. Lee, W. Lee, Y. Hong, G. Lee and D. S. Yoon, *Sensors and Actuators B: Chemical*, 2018, **255**, 1788-1804.

23.    H. Wu, Z. Chen, J. Zhang, F. Wu, C. He, Y. Wu and Z. Ren, *Journal of Materials Chemistry A*, 2017, **5**, 24493-24501.

24.    S. Park, M. Park, S. Kim, S.-G. Yi, M. Kim, J. Son, J. Cha, J. Hong and K.-H. Yoo, *Applied Physics Letters*, 2017, **111**.

25.    S. W. Lee, W. Lee, D. Lee, Y. Choi, W. Kim, J. Park, J. H. Lee, G. Lee and D. S. Yoon, *Sensors and Actuators B: Chemical*, 2018, **266**, 485-492.

26.    N. Joshi, T. Hayasaka, Y. Liu, H. Liu, O. N. Oliveira, Jr. and L. Lin, *Mikrochim Acta*, 2018, **185**, 213.

27.    Y. Li, M. Jiao, H. Zhao and M. Yang, *Sensors and Actuators B: Chemical*, 2018, **264**, 285-295.

28.    J. Cai, C. Zhang, A. Khan, C. Liang and W.-D. Li, *RSC Advances*, 2018, **8**, 5312-5320.

29.    H. J. Park, W.-J. Kim, H.-K. Lee, D.-S. Lee, J.-H. Shin, Y. Jun and Y. J. Yun, *Sensors and Actuators B: Chemical*, 2018, **257**, 846-852.

30.    H. T. Hien, H. T. Giang, N. V. Hieu, T. Trung and C. V. Tuan, *Sensors and Actuators B: Chemical*, 2017, **249**, 348-356.

31.    V. L. Patil, S. A. Vanalakar, P. S. Patil and J. H. Kim, *Sensors and Actuators B: Chemical*, 2017, **239**, 1185-1193.

32.    M. Jiao, N. V. Chien, N. V. Duy, N. D. Hoa, N. V. Hieu, K. Hjort and H. Nguyen, *Materials Letters*, 2016, **169**, 231-235.

33.    D. N. Oosthuizen, D. E. Motaung and H. C. Swart, *Sensors and Actuators B: Chemical*, 2018, **266**, 761-772.

34.    X. Liu, M. Hu, Y. Wang, J. Liu and Y. Qin, *Journal of Alloys and Compounds*, 2016, **685**, 364-369.

35.    A. Umar, J.-H. Lee, R. Kumar, O. Al-Dossary, A. A. Ibrahim and S. Baskoutas, *Materials & Design*, 2016, **105**, 16-24.

36.    O. Lupan, V. Postica, V. Cretu, N. Wolff, V. Duppel, L. Kienle and R. Adelung, *physica status solidi (RRL) - Rapid Research Letters*, 2016, **10**, 260-266.

37.    S. Xu, H. Zhao, Y. Xu, R. Xu and Y. Lei, *ACS Appl Mater Interfaces*, 2018, **10**, 13895-13902.

38.    I. Cho, K. Kang, D. Yang, J. Yun and I. Park, *ACS Appl Mater Interfaces*, 2017, **9**, 27111-27119.

39.    Y. Zhao, W. Zhang, B. Yang, J. Liu, X. Chen, X. Wang and C. Yang, *Nanotechnology*, 2017, **28**, 452002.

40.    X. Tong, W. Shen, X. Chen and J.-P. Corriou, *Ceramics International*, 2017, **43**, 14200-14209.

41.    W. Guo, Q. Feng, Y. Tao, L. Zheng, Z. Han and J. Ma, *Materials Research Bulletin*, 2016, **73**, 302-307.

42.    Z. Li, Y. Huang, S. Zhang, W. Chen, Z. Kuang, D. Ao, W. Liu and Y. Fu, *J Hazard Mater*, 2015, **300**, 167-174.

43.    Z. Li, Z. Lin, N. Wang, Y. Huang, J. Wang, W. Liu, Y. Fu and Z. Wang, *Materials & Design*, 2016, **110**, 532-539.

44.    D. Han, L. Zhai, F. Gu and Z. Wang, *Sensors and Actuators B: Chemical*, 2018, **262**, 655-663.

45.    J. Hu, Y. Sun, Y. Xue, M. Zhang, P. Li, K. Lian, S. Zhuiykov, W. Zhang and Y. Chen, *Sensors and Actuators B: Chemical*, 2018, **257**, 124-135.

46.    S. C. Zhang, Y. W. Huang, Z. Kuang, S. Y. Wang, W. L. Song, D. Y. Ao, W. Liu and Z. J. Li, *Nanoscience*

*and Nanotechnology Letters*, 2015, **7**, 455-461.

47.  Z. Li, S. Yan, Z. Wu, H. Li, J. Wang, W. Shen, Z. Wang and Y. Fu, *International Journal of Hydrogen Energy*, 2018, DOI: 10.1016/j.ijhydene.2018.10.101.

48.  T. Zhou, T. Zhang, J. Deng, R. Zhang, Z. Lou and L. Wang, *Sensors and Actuators B: Chemical*, 2017, **242**, 369-377.

49.  S. F. Shen, M. L. Xu, D. B. Lin and H. B. Pan, *Applied Surface Science*, 2017, **396**, 327-332.

50.  Z. Zhang, L. Zhu, Z. Wen and Z. Ye, *Sensors and Actuators B: Chemical*, 2017, **238**, 1052-1059.

51.  S. Poongodi, P. S. Kumar, D. Mangalaraj, N. Ponpandian, P. Meena, Y. Masuda and C. Lee, *Journal of Alloys and Compounds*, 2017, **719**, 71-81.

52.  H. Kim, Y. Pak, Y. Jeong, W. Kim, J. Kim and G. Y. Jung, *Sensors and Actuators B: Chemical*, 2018, **262**, 460-468.

53.  S. G. R, N. M, V. L. Patil, P. S, M. C, S. Kawasaki, P. S. Patil and Y. Hayakawa, *Sensors and Actuators B: Chemical*, 2018, **255**, 672-683.

54.  X. Hu, Z. Zhu, C. Chen, T. Wen, X. Zhao and L. Xie, *Sensors and Actuators B: Chemical*, 2017, **253**, 809-817.

55.  L. Xiao, S. Xu, G. Yu and S. Liu, *Sensors and Actuators B: Chemical*, 2018, **255**, 2002-2010.

56.  V. S. Bhati, S. Ranwa, S. Rajamani, K. Kumari, R. Raliya, P. Biswas and M. Kumar, *ACS Appl Mater Interfaces*, 2018, **10**, 11116-11124.

57.  V. S. Bhati, S. Ranwa, M. Fanetti, M. Valant and M. Kumar, *Sensors and Actuators B: Chemical*, 2018, **255**, 588-597.

58.  V. V. Ganbavle, S. I. Inamdar, G. L. Agawane, J. H. Kim and K. Y. Rajpure, *Chemical Engineering Journal*, 2016, **286**, 36-47.

59.  X. Kou, N. Xie, F. Chen, T. Wang, L. Guo, C. Wang, Q. Wang, J. Ma, Y. Sun, H. Zhang and G. Lu, *Sensors and Actuators B: Chemical*, 2018, **256**, 861-869.

60.  Q. Zhou, W. Chen, L. Xu, R. Kumar, Y. Gui, Z. Zhao, C. Tang and S. Zhu, *Ceramics International*, 2018, **44**, 4392-4399.

61.  C. Zhao, H. Gong, W. Lan, R. Ramachandran, H. Xu, S. Liu and F. Wang, *Sensors and Actuators B: Chemical*, 2018, **258**, 492-500.

62.  H. W. Kim, H. G. Na, Y. J. Kwon, S. Y. Kang, M. S. Choi, J. H. Bang, P. Wu and S. S. Kim, *ACS Appl Mater Interfaces*, 2017, **9**, 31667-31682.

63.  P. Tyagi, A. Sharma, M. Tomar and V. Gupta, *Sensors and Actuators B: Chemical*, 2017, **248**, 980-986.

64.  B. Zhang, M. Cheng, G. Liu, Y. Gao, L. Zhao, S. Li, Y. Wang, F. Liu, X. Liang, T. Zhang and G. Lu, *Sensors and Actuators B: Chemical*, 2018, **263**, 387-399.

65.  S. Park, S. Kim, H. Kheel, S. K. Hyun, C. Jin and C. Lee, *Materials Research Bulletin*, 2016, **82**, 130-135.

66.  D. Li, L. Qin, P. Zhao, Y. Zhang, D. Liu, F. Liu, B. Kang, Y. Wang, H. Song, T. Zhang and G. Lu, *Sensors and Actuators B: Chemical*, 2018, **254**, 834-841.

67.  H. Gao, L. Zhao, L. Wang, P. Sun, H. Lu, F. Liu, X. Chuai and G. Lu, *Sensors and Actuators B: Chemical*, 2018, **255**, 3505-3515.

68.  I. Eisele, T. Doll and M. Burgmair, *Sensors and Actuators B-Chemical*, 2001, **78**, 19-25.

69.  S. Stegmeier, M. Fleischer, A. Tawil, P. Hauptmann, K. Egly and K. Rose, *Sensors and Actuators B: Chemical*, 2011, **154**, 270-276.

70.  A. I. Ayesh, *Journal of Nanomaterials*, 2016, **2016**, 1-17.

71. Z. S. Hosseini, A. I. zad and A. Mortezaali, *Sensors and Actuators B: Chemical*, 2015, **207**, 865-871.

72. T. Sin Tee, T. Chun Hui, C. Wu Yi, Y. Chi Chin, A. A. Umar, G. Riski Titian, L. Hock Beng, L. Kok Sing, M. Yahaya and M. M. Salleh, *Sensors and Actuators B: Chemical*, 2016, **227**, 304-312.

73. A. Azam, S. S. Habib, N. A. Salah and F. Ahmed, *Int J Nanomedicine*, 2013, **8**, 3875-3881.

74. H. Wang, Q. Sun, Y. Yao, Y. Li, J. Wang and L. Chen, *Ceramics International*, 2016, **42**, 8565-8571.

75. W. Li, J. Liang, J. Liu, L. Zhou, R. Yang and M. Hu, *Materials Letters*, 2016, **173**, 199-202.

76. Y. Wei, C. Chen, G. Yuan and S. Gao, *Journal of Alloys and Compounds*, 2016, **681**, 43-49.

77. Y. Li, Q. Zhang, X. Li, H. Bai, W. Li, T. Zeng and G. Xi, *RSC Advances*, 2016, **6**, 95747-95752.

78. S. Mohamed Sali, S. Joy, N. Meenakshisundaram, R. K. Karn, C. Gopalakrishnan, P. Karthick, K. Jeyadheepan and K. Sankaranarayanan, *RSC Advances*, 2017, **7**, 37720-37728.

79. Z. P. Tshabalala, D. E. Motaung, G. H. Mhlongo and O. M. Ntwaeaborwa, *Sensors and Actuators B: Chemical*, 2016, **224**, 841-856.

80. Y. Huang, W. Chen, S. Zhang, Z. Kuang, D. Ao, N. R. Alkurd, W. Zhou, W. Liu, W. Shen and Z. Li, *Applied Surface Science*, 2015, **351**, 1025-1033.

81. R. K. Bedi and I. Singh, *ACS Appl Mater Interfaces*, 2010, **2**, 1361-1368.

82. P. Shankar and J. B. B. Rayappan, *ACS Appl Mater Interfaces*, 2017, **9**, 38135-38145.

83. N. Kumar, A. K. Srivastava, R. Nath, B. K. Gupta and G. D. Varma, *Dalton Trans*, 2014, **43**, 5713-5720.

84. Z. Zeng, K. Wang, Z. Zhang, J. Chen and W. Zhou, *Nanotechnology*, 2009, **20**, 045503.

85. Y. Shen, S. Zhao, J. Ma, X. Chen, W. Wang, D. Wei, S. Gao, W. Liu, C. Han and B. Cui, *Journal of Alloys and Compounds*, 2016, **664**, 229-234.

86. Z. Li, X. Niu, Z. Lin, N. Wang, H. Shen, W. Liu, K. Sun, Y. Q. Fu and Z. Wang, *Journal of Alloys and Compounds*, 2016, **682**, 647-653.

87. O. Lupan, V. Postica, R. Adelung, F. Labat, I. Ciofini, U. Schürmann, L. Kienle, L. Chow, B. Viana and T. Pauporté, *physica status solidi (RRL) - Rapid Research Letters*, 2018, **12**.

88. Y. L. Wang, X. C. Jiang and Y. N. Xia, *Journal of the American Chemical Society*, 2003, **125**, 16176-16177.

89. O. Lupan, L. Chow, T. Pauporté, L. K. Ono, B. Roldan Cuenya and G. Chai, *Sensors and Actuators B: Chemical*, 2012, **173**, 772-780.

90. W. Song, H. Wu, J. Wang, Y. Lin, J. Song, Y. Xie, L. Li and K. Shi, *Australian Journal of Chemistry*, 2015, **68**, 1569.

91. L. Yu, F. Guo, S. Liu, B. Yang, Y. Jiang, L. Qi and X. Fan, *Journal of Alloys and Compounds*, 2016, **682**, 352-356.

92. Z. Li, Z. Lin, N. Wang, J. Wang, W. Liu, K. Sun, Y. Q. Fu and Z. Wang, *Sensors and Actuators B: Chemical*, 2016, **235**, 222-231.

93. Z. Li, N. Wang, Z. Lin, J. Wang, W. Liu, K. Sun, Y. Q. Fu and Z. Wang, *ACS Appl Mater Interfaces*, 2016, **8**, 20962-20968.

94. J. Zhang, D. Zeng, Q. Zhu, J. Wu, Q. Huang and C. Xie, *The Journal of Physical Chemistry C*, 2016, **120**, 3936-3945.

95. C. Jiang, G. Zhang, Y. Wu, L. Li and K. Shi, *CrystEngComm*, 2012, **14**, 2739.

96. A. Hazra, K. Dutta, B. Bhowmik, P. P. Chattopadhyay and P. Bhattacharyya, *Applied Physics Letters*, 2014, **105**, 081604.

97. B. Bhowmik, A. Hazra, K. Dutta and P. Bhattacharyya, *IEEE Transactions on Device and Materials*

*Reliability*, 2014, **14**, 961-967.

98. J. Z. Zhang and Y. Yan, *Journal of Materials Science*, 2017, **52**, 13711-13718.

99. S. Shao, H. Wu, S. Wang, Q. Hong, R. Koehn, T. Wu and W.-F. Rao, *J. Mater. Chem. C*, 2015, **3**, 10819-10829.

100. H. Duan, L. Yan, Y. He, H. Li, L. Liu, Y. Cheng and L. Du, *Materials Research Express*, 2017, **4**, 095022.

101. Y. Wang, G. Duan, Y. Zhu, H. Zhang, Z. Xu, Z. Dai and W. Cai, *Sensors and Actuators B: Chemical*, 2016, **228**, 74-84.

102. J. Gao, H. Wu, J. Zhou, L. Yao, G. Zhang, S. Xu, Y. Xie, L. Li and K. Shi, *New Journal of Chemistry*, 2016, **40**, 1306-1311.

103. B. Wu, L. Wang, H. Wu, K. Kan, G. Zhang, Y. Xie, Y. Tian, L. Li and K. Shi, *Microporous and Mesoporous Materials*, 2016, **225**, 154-163.

104. M. Kaur, N. Jain, K. Sharma, S. Bhattacharya, M. Roy, A. K. Tyagi, S. K. Gupta and J. V. Yakhmi, *Sensors and Actuators B: Chemical*, 2008, **133**, 456-461.

105. M. Seetha, P. Meena, D. Mangalaraj, Y. Masuda and K. Senthil, *Materials Chemistry and Physics*, 2012, **133**, 47-54.

106. R. Senthilkumar, G. Ravi, C. Sanjeeviraja, M. Arivanandhan and Y. Hayakawa, 2013, DOI: 10.1063/1.4791204, 648-649.

107. D. F. Rodriguez, P. M. Perillo, C. A. Rinaldi, A. Lamagna and P. Gouma, 2011, DOI: 10.1063/1.3626358, 199-200.

108. M. N. Cardoza-Contreras, J. M. Romo-Herrera, L. A. Rios, R. Garcia-Gutierrez, T. A. Zepeda and O. E. Contreras, *Sensors (Basel)*, 2015, **15**, 30539-30544.

109. C. Wang, X. Chu and M. Wu, *Sensors and Actuators B: Chemical*, 2006, **113**, 320-323.

110. Y. Xia, J. Wang, X. Li, X. Dan, D. Zhou, L. Xiang and S. Komarneni, *Ceramics International*, 2016, **42**, 15876-15880.

111. N. Du, H. Zhang, B. D. Chen, X. Y. Ma, Z. H. Liu, J. B. Wu and D. R. Yang, *Advanced Materials*, 2007, **19**, 1641-1645.

112. P. Dhivya and M. Sridharan, *Journal of Electronic Materials*, 2014, **43**, 3211-3216.

113. S. Arunkumar, T. Hou, Y.-B. Kim, B. Choi, S. H. Park, S. Jung and D.-W. Lee, *Sensors and Actuators B: Chemical*, 2017, **243**, 990-1001.

114. S.-W. Choi and S. S. Kim, *Sensors and Actuators B: Chemical*, 2012, **168**, 8-13.

115. K. Wang, T. Zhao, G. Lian, Q. Yu, C. Luan, Q. Wang and D. Cui, *Sensors and Actuators B: Chemical*, 2013, **184**, 33-39.

116. P. P. Subha, K. Hasna and M. K. Jayaraj, *Materials Research Express*, 2017, **4**, 105037.

117. S. Wang, D. Huang, S. Xu, W. Jiang, T. Wang, J. Hu, N. Hu, Y. Su, Y. Zhang and Z. Yang, *Phys Chem Chem Phys*, 2017, **19**, 19043-19049.

118. G. H. Mhlongo, K. Shingange, Z. P. Tshabalala, B. P. Dhonge, F. A. Mahmoud, B. W. Mwakikunga and D. E. Motaung, *Applied Surface Science*, 2016, **390**, 804-815.

119. J. Wang, L. Wei, L. Zhang, J. Zhang, H. Wei, C. Jiang and Y. Zhang, *Journal of Materials Chemistry*, 2012, **22**, 20038.

120. J. Wang, P. Yang and X. Wei, *ACS Appl Mater Interfaces*, 2015, **7**, 3816-3824.

121. P. Chaudhari and S. Mishra, *Measurement*, 2016, **90**, 468-474.

122. J. Zhou, M. Ikram, A. U. Rehman, J. Wang, Y. Zhao, K. Kan, W. Zhang, F. Raziq, L. Li and K. Shi, *Sensors and Actuators B: Chemical*, 2018, **255**, 1819-1830.

123. M. Kaur, B. K. Dadhich, R. Singh, KailasaGanapathi, T. Bagwaiya, S. Bhattacharya, A. K. Debnath, K. P. Muthe and S. C. Gadkari, *Sensors and Actuators B: Chemical*, 2017, **242**, 389-403.

124. V. Srivastava and K. Jain, *Materials Letters*, 2016, **169**, 28-32.

125. P.-G. Su and T.-T. Pan, *Materials Chemistry and Physics*, 2011, **125**, 351-357.

126. H. Zhang, L. Yu, Q. Li, Y. Du and S. Ruan, *Sensors and Actuators B: Chemical*, 2017, **241**, 109-115.

127. Z. Li, J. Wang, S. Zhang, S. Yan, B. Cao, W. Shen, Z. Wang and Y. Q. Fu, *Journal of Alloys and Compounds*, 2018, **742**, 712-720.

128. V. Inderan, M. M. Arafat, S. Kumar, A. Haseeb, Z. T. Jiang, M. Altarawneh and H. L. Lee, *Nanotechnology*, 2017, **28**, 265702.

129. A. U. Rehman, J. Zhang, J. Zhou, K. Kan, L. Li and K. Shi, *Microporous and Mesoporous Materials*, 2017, **240**, 50-56.

130. J. Liang, K. Zhu, R. Yang and M. Hu, *Ceramics International*, 2018, **44**, 2261-2268.

131. H. Xu, J. Zhang, A. U. Rehman, L. Gong, K. Kan, L. Li and K. Shi, *Applied Surface Science*, 2017, **412**, 230-237.

132. D. Liu, L. Lin, Q. Chen, H. Zhou and J. Wu, *ACS Sens*, 2017, **2**, 1491-1497.

133. Y. Wang, Y. Zhou, C. Meng, Z. Gao, X. Cao, X. Li, L. Xu, W. Zhu, X. Peng, B. Zhang, Y. Lin and L. Liu, *Nanotechnology*, 2016, **27**, 425503.

134. S. Xu, J. Gao, L. Wang, K. Kan, Y. Xie, P. Shen, L. Li and K. Shi, *Nanoscale*, 2015, **7**, 14643-14651.

135. Z. Liu, L. Yu, F. Guo, S. Liu, L. Qi, M. Shan and X. Fan, *Applied Surface Science*, 2017, **423**, 721-727.

136. N. Van Hieu, L. T. B. Thuy and N. D. Chien, *Sensors and Actuators B: Chemical*, 2008, **129**, 888-895.

137. N. Tiwale, *Materials Science and Technology*, 2015, **31**, 1681-1697.

138. A. Mirzaei, B. Hashemi and K. Janghorban, *Journal of Materials Science: Materials in Electronics*, 2015, **27**, 3109-3144.

139. G. Korotcenkov and B. K. Cho, *Sensors and Actuators B: Chemical*, 2014, **196**, 80-98.

140. S. Das and V. Jayaraman, *Progress in Materials Science*, 2014, **66**, 112-255.

141. H.-J. Kim and J.-H. Lee, *Sensors and Actuators B: Chemical*, 2014, **192**, 607-627.

142. D. R. Miller, S. A. Akbar and P. A. Morris, *Sensors and Actuators B: Chemical*, 2014, **204**, 250-272.

143. G. Korotcenkov, V. Brinzari and B. K. Cho, *Microchimica Acta*, 2016, **183**, 1033-1054.

144. P. Rai, S. M. Majhi, Y.-T. Yu and J.-H. Lee, *RSC Advances*, 2015, **5**, 76229-76248.

145. S. Gupta Chatterjee, S. Chatterjee, A. K. Ray and A. K. Chakraborty, *Sensors and Actuators B: Chemical*, 2015, **221**, 1170-1181.

146. M. Gardon and J. M. Guilemany, *Journal of Materials Science: Materials in Electronics*, 2012, **24**, 1410-1421.

147. P. T. Moseley, *Measurement Science and Technology*, 2017, **28**, 082001.

148. Y. F. Sun, S. B. Liu, F. L. Meng, J. Y. Liu, Z. Jin, L. T. Kong and J. H. Liu, *Sensors (Basel)*, 2012, **12**, 2610-2631.

149. H. Gu, Z. Wang and Y. Hu, *Sensors (Basel)*, 2012, **12**, 5517-5550.

150. A. Mirzaei, S. G. Leonardi and G. Neri, *Ceramics International*, 2016, **42**, 15119-15141.

151. L. Zhu and W. Zeng, *Sensors and Actuators A: Physical*, 2017, **267**, 242-261.

152. A. D. Faisal, *Bulletin of Materials Science*, 2017, **40**, 1061-1068.

153.    N. Zhang, K. Yu, Q. Li, Z. Q. Zhu and Q. Wan, *Journal of Applied Physics*, 2008, **103**, 104305.

154.    T. Kondo, Y. Sato, M. Kinoshita, P. Shankar, N. N. Mintcheva, M. Honda, S. Iwamori and S. A. Kulinich, *Japanese Journal of Applied Physics*, 2017, **56**, 080304.

155.    Y. Li, S. Wang, P. Hao, J. Tian, H. Cui and X. Wang, *Sensors and Actuators B-Chemical*, 2018, **273**, 751-759.

156.    A. Beniwal, P. K. Sahu and S. Sharma, *Journal of Sol-Gel Science and Technology*, 2018, **88**, 322-333.

157.    M. Kodu, T. Avarmaa, A. Floren and R. Jaaniso, *Journal of the European Ceramic Society*, 2013, **33**, 2335-2340.

158.    K. Khun Khun, A. Mahajan and R. K. Bedi, *Journal of Applied Physics*, 2009, **106**, 124509.

159.    T. Yang, M. Zhu, K. Gu, C. Zhai, Q. Zhao, X. Yang and M. Zhang, *New Journal of Chemistry*, 2018, **42**, 13612-13618.

160.    D. Hanft, M. Bektas and R. Moos, *Materials (Basel)*, 2018, **11**.

161.    L. Xu, B. Dong, Y. Wang, X. Bai, Q. Liu and H. Song, *Sensors and Actuators B: Chemical*, 2010, **147**, 531-538.

162.    T. M. Perfecto, C. A. Zito and D. P. Volanti, *CrystEngComm*, 2017, **19**, 2733-2738.

163.    X. W. Huang, X. B. Zou, J. Y. Shi, J. W. Zhao, Y. Li, L. Hao and J. Zhang, *Anal Chim Acta*, 2013, **787**, 233-238.

164.    H. Liu, W. Shen, X. Chen and J.-P. Corriou, *Journal of Materials Science-Materials in Electronics*, 2018, **29**, 18380-18387.

165.    L. Y. Hong and H. N. Lin, *Beilstein J Nanotechnol*, 2016, **7**, 1044-1051.

166.    Z. P. Tshabalala, K. Shingange, B. P. Dhonge, O. M. Ntwaeaborwa, G. H. Mhlongo and D. E. Motaung, *Sensors and Actuators B: Chemical*, 2017, **238**, 402-419.

167.    P. M. Perillo and D. F. Rodríguez, *Sensors and Actuators B: Chemical*, 2014, **193**, 263-266.

168.    B. C. Yadav, S. Singh and A. Yadav, *Applied Surface Science*, 2011, **257**, 1960-1966.

169.    X. Song, Q. Xu, T. Zhang, B. Song, C. Li and B. Cao, *Sensors and Actuators B-Chemical*, 2018, **268**, 170-181.

170.    Y. X. Li, Z. X. Song, F. Jiang, Q. Sun, F. Ma, H. R. Wang and K. Chen, *Ceramics International*, 2016, **42**, 18318-18323.

171.    J. Liang, W. Li, J. Liu and M. Hu, *Journal of Alloys and Compounds*, 2016, **687**, 845-854.

172.    C. A. Zito, T. M. Perfecto and D. P. Volanti, *New Journal of Chemistry*, 2018, **42**, 15954-15961.

173.    T.-R. Rashid, D.-T. Phan and G.-S. Chung, *Sensors and Actuators B: Chemical*, 2013, **185**, 777-784.

174.    P. Dhivya, A. K. Prasad and M. Sridharan, *Ceramics International*, 2014, **40**, 409-415.

175.    S. A. Hakim, Y. Liu, G. S. Zakharova and W. Chen, *RSC Advances*, 2015, **5**, 23489-23497.

176.    S. Lin, D. Li, J. Wu, X. Li and S. A. Akbar, *Sensors and Actuators B: Chemical*, 2011, **156**, 505-509.

177.    B. Zhang, M. Li, Z. Song, H. Kan, H. Yu, Q. Liu, G. Zhang and H. Liu, *Sensors and Actuators B: Chemical*, 2017, **249**, 558-563.

178.    W. Ponhan, S. Phadungdhitidhada and S. Choopun, *Materials Today: Proceedings*, 2017, **4**, 6342-6348.

179.    M. Thepnurat, T. Chairuangsri, N. Hongsith, P. Ruankham and S. Choopun, *ACS Appl Mater Interfaces*, 2015, **7**, 24177-24184.

180.    P. Shankar and J. B. B. Rayappan, *J. Mater. Chem. C*, 2017, **5**, 10869-10880.

181.    N. Van Quy, V. A. Minh, N. Van Luan, V. N. Hung and N. Van Hieu, *Sensors and Actuators B:*

*Chemical*, 2011, **153**, 188-193.

182. G. K. Mani and J. B. B. Rayappan, *Sensors and Actuators B: Chemical*, 2013, **183**, 459-466.

183. X. Pan, X. Zhao, J. Chen, A. Bermak and Z. Fan, *Sensors and Actuators B: Chemical*, 2015, **206**, 764-771.

184. V. P. Verma, S. Das, S. Hwang, H. Choi, M. Jeon and W. Choi, *Materials Science and Engineering: B*, 2010, **171**, 45-49.

185. X. Pan and X. Zhao, *Sensors (Basel)*, 2015, **15**, 8919-8930.

186. O. Lupan, G. Chai and L. Chow, *Microelectronics Journal*, 2007, **38**, 1211-1216.

187. O. Lupan, G. Chai and L. Chow, *Microelectronic Engineering*, 2008, **85**, 2220-2225.

188. B.-R. Huang and J.-C. Lin, *Applied Surface Science*, 2013, **280**, 945-949.

189. K. Vijayalakshmi and D. Gopalakrishna, *Journal of Materials Science: Materials in Electronics*, 2014, **25**, 2253-2260.

190. Y. T. Lim, J. Y. Son and J. S. Rhee, *Ceramics International*, 2013, **39**, 887-890.

191. J. J. Hassan, M. A. Mahdi, C. W. Chin, H. Abu-Hassan and Z. Hassan, *Sensors and Actuators B: Chemical*, 2013, **176**, 360-367.

192. S. Yang, Z. Wang, Y. Hu, X. Luo, J. Lei, D. Zhou, L. Fei, Y. Wang and H. Gu, *ACS Appl Mater Interfaces*, 2015, **7**, 9247-9253.

193. I. H. Kadhim and H. Abu Hassan, *Journal of Electronic Materials*, 2016, **46**, 1419-1426.

194. M. Belaqziz, M. b. Amjoud, A. Gaddari, B. Rhouta and D. Mezzane, *Superlattices and Microstructures*, 2014, **71**, 185-189.

195. A. Kaur Bal, A. Singh and R. K. Bedi, *Physica B: Condensed Matter*, 2010, **405**, 3124-3128.

196. X. Mu, C. Chen, L. Han, B. Shao, Y. Wei, Q. Liu and P. Zhu, *Journal of Alloys and Compounds*, 2015, **637**, 55-61.

197. L. Yanxiao, Z. Xiao-bo, H. Xiao-wei, S. Ji-yong, Z. Jie-wen, M. Holmes and L. Hao, *Biosens Bioelectron*, 2015, **67**, 35-41.

198. J. Wang, Z. Li, S. Zhang, S. Yan, B. Cao, Z. Wang and Y. Fu, *Sensors and Actuators B: Chemical*, 2018, **255**, 862-870.

199. Z. Li, S. Yan, S. Zhang, J. Wang, W. Shen, Z. Wang and Y. Q. Fu, *Journal of Alloys and Compounds*, 2019, **770**, 721-731.

200. C. Zhang, X. Geng, H. Liao, C.-J. Li and M. Debliquy, *Sensors and Actuators B: Chemical*, 2017, **242**, 102-111.

201. R. Chen, J. Wang and L. Xiang, *Sensors and Actuators B-Chemical*, 2018, **270**, 207-215.

202. Y. Wu, M. Hu and Y. Tian, *Chinese Physics B*, 2017, **26**, 020701.

203. V. Annapureddy, Y. Kim, G.-T. Hwang, H. W. Jang, S.-D. Kim, J.-J. Choi, B. Cho and J. Ryu, *Advanced Materials Interfaces*, 2018, **5**, 1700811.

204. L. Han, C. Chen, Y. Wei, B. Shao, X. Mu, Q. Liu and P. Zhu, *Journal of Alloys and Compounds*, 2016, **656**, 326-331.

205. M. Hu, D.-L. Jia, Q.-L. Liu, M.-D. Li and P. Sun, *Chinese Physics B*, 2013, **22**, 068204.

206. W. Liu, L. Xu, K. Sheng, C. Chen, X. Zhou, B. Dong, X. Bai, S. Zhang, G. Lu and H. Song, *Journal of Materials Chemistry A*, 2018, **6**, 10976-10989.

207. S. S. Kim, H. G. Na, Y. J. Kwon, H. Y. Cho and H. W. Kim, *Metals and Materials International*, 2015, **21**, 415-421.

208. X. Gou, R. Li, G. Wang, Z. Chen and D. Wexler, *Nanotechnology*, 2009, **20**, 495501.

209. S. Bai, Y. Ma, X. Shu, J. Sun, Y. Feng, R. Luo, D. Li and A. Chen, *Industrial & Engineering Chemistry*

*Research*, 2017, **56**, 2616-2623.

210. A. Wei, Z. Wang, L.-H. Pan, W.-W. Li, L. Xiong, X.-C. Dong and W. Huang, *Chinese Physics Letters*, 2011, **28**, 080702.

211. H. Abdollahi, M. Samkan and M. M. Hashemi, *Microsystem Technologies-Micro-and Nanosystems-Information Storage and Processing Systems*, 2018, **24**, 3741-3749.

212. R. S. Ganesh, G. K. Mani, R. Elayaraja, E. Durgadevi, M. Navaneethan, S. Ponnusamy, K. Tsuchiya, C. Muthamizhchelvan and Y. Hayakawa, *Applied Surface Science*, 2018, **449**, 314-321.

213. A. El Bouari, A. Gaddari, M. Amjoud, F. Berger, J. B. Sanchez, M. Lahcini, B. Rhouta, D. Mezzane, C. Mavon, R. El Ouatib, H. Hannache, S. Krimi, M. Lamire, I. Mansouri, R. Moussa and A. Aboulayt, *MATEC Web of Conferences*, 2013, **5**, 04010.

214. Y. Xiong, W. Xu, D. Ding, W. Lu, L. Zhu, Z. Zhu, Y. Wang and Q. Xue, *Journal of Hazardous Materials*, 2018, **341**, 159-167.

215. S. Yang, Y. Liu, W. Jin, Y. Qi, G. S. Zakharova and W. Chen, *Ferroelectrics*, 2015, **477**, 112-120.

216. Y. Xiong, Z. Zhu, T. Guo, H. Li and Q. Xue, *J Hazard Mater*, 2018, **353**, 290-299.

217. E. Zampetti, A. Macagnano and A. Bearzotti, *Journal of Nanoparticle Research*, 2013, **15**.

218. C. Shao, Y. Chang and Y. Long, *Sensors and Actuators B: Chemical*, 2014, **204**, 666-672.

219. M. Chitra, K. Uthayarani, N. Rajasekaran, N. Neelakandeswari, E. K. Girija and D. P. Padiyan, *Chinese Physics Letters*, 2015, **32**, 078101.

220. E. Wongrat, W. Ponhan and S. Choopun, *Ceramics International*, 2017, **43**, S520-S524.

221. L. Hou, C.-M. Zhang, P. Ma, L. Li, K.-K. Zhu, X.-F. Kang and W. Chen, *Chinese Journal of Analytical Chemistry*, 2018, **46**, E1854-E1862.

222. A. P. Sharma, P. Dhakal, D. K. Pradhan, M. K. Behera, B. Xiao and M. Bahoura, *Aip Advances*, 2018, **8**.

223. B. Sakthivel, L. Manjakkal and G. Nammalvar, *IEEE Sensors Journal*, 2017, **17**, 6529-6536.

224. N. S. Ramgir, S. K. Ganapathi, M. Kaur, N. Datta, K. P. Muthe, D. K. Aswal, S. K. Gupta and J. V. Yakhmi, *Sensors and Actuators B: Chemical*, 2010, **151**, 90-96.

225. Z. Li, J. Wang, N. Wang, S. Yan, W. Liu, Y. Q. Fu and Z. Wang, *Journal of Alloys and Compounds*, 2017, **725**, 1136-1143.

226. J. Zhang, D. Zeng, Q. Zhu, J. Wu, K. Xu, T. Liao, G. Zhang and C. Xie, *The Journal of Physical Chemistry C*, 2015, **119**, 17930-17939.

227. J. Zhou, M. Ikram, A. U. Rehman, J. Wang, Y. Zhao, K. Kan, W. Zhang, F. Raziq, L. Li and K. Shi, *Sensors and Actuators B-Chemical*, 2018, **255**, 1819-1830.

228. I. Singh and R. K. Bedi, *Solid State Sciences*, 2011, **13**, 2011-2018.

229. D. N. Oosthuizen, D. E. Motaung and H. C. Swart, *Sensors and Actuators B-Chemical*, 2018, **266**, 761-772.

230. S. Li, M. Wang, C. Li, J. Liu, M. Xu, J. Liu and J. Zhang, *Science China-Materials*, 2018, **61**, 1085-1094.

231. Z. Wang, F. Li, H. Wang, A. Wang and S. Wu, *Journal of Materials Science-Materials in Electronics*, 2018, **29**, 16654-16659.

232. S. Wang, D. Huang, S. Xu, W. Jiang, T. Wang, J. Hu, N. Hu, Y. Su, Y. Zhang and Z. Yang, *Physical Chemistry Chemical Physics*, 2017, **19**, 19043-19049.

233. J. Wang, L. Wei, L. Zhang, J. Zhang, H. Wei, C. Jiang and Y. Zhang, *Journal of Materials Chemistry*, 2012, **22**, 20038-20047.

234. X. Zhang, J. Wang, L. Xuan, Z. Zhu, Q. Pan, K. Shi and G. Zhang, *Journal of Alloys and Compounds*,

2018, **768**, 190-197.

235. B. Geng, F. Zhan, C. Fang and N. Yu, *Journal of Materials Chemistry*, 2008, **18**, 4977-4984.

236. S. Li, F.-L. Li, S.-M. Zhou, P. Wang, K. Cheng and Z.-L. Du, *Chinese Physics B*, 2009, **18**, 3985-3989.

237. H. Liu, X. Du, X. Xing, G. Wang and S. Z. Qiao, *Chemical Communications*, 2012, **48**, 865-867.

238. S. Balamurugan, A. Rajalakshmi and D. Balamurugan, *Journal of Alloys and Compounds*, 2015, **650**, 863-870.

239. R. Kumar, R. Kumar, N. Kushwaha and J. Mittal, *Ieee Sensors Journal*, 2016, **16**, 4691-4695.

240. W. Zhang, C. Zeng, M. Kong, Y. Pan and Z. Yang, *Sensors and Actuators B-Chemical*, 2012, **162**, 292-299.

241. Y. Wang, B. Liu, D. Cai, H. Li, Y. Liu, D. Wang, L. Wang, Q. Li and T. Wang, *Sensors and Actuators B: Chemical*, 2014, **201**, 351-359.

242. N. S. Ramgir, P. K. Sharma, N. Datta, M. Kaur, A. K. Debnath, D. K. Aswal and S. K. Gupta, *Sensors and Actuators B: Chemical*, 2013, **186**, 718-726.

243. Q. A. Drmosh, Z. H. Yamani, A. K. Mohamedkhair, A. H. Y. Hendi, M. K. Hossain and A. Ibrahim, *Materials Letters*, 2018, **214**, 283-286.

244. H. Fu, C. Hou, F. Gu, D. Han and Z. Wang, *Sensors and Actuators B: Chemical*, 2017, **243**, 516-524.

245. D. Naberezhnyi, M. Rumyantseva, D. Filatova, M. Batuk, J. Hadermann, A. Baranchikov, N. Khmelevsky, A. Aksenenko, E. Konstantinova and A. Gaskov, *Nanomaterials (Basel)*, 2018, **8**.

246. A. N. A. Anasthasiya, R. K. Kampara, P. K. Rai and B. G. Jeyaprakash, *Applied Surface Science*, 2018, **449**, 244-249.

247. Z. Zhu, C.-T. Kao and R.-J. Wu, *Applied Surface Science*, 2014, **320**, 348-355.

248. S. Yan, Z. Li, H. Li, Z. Wu, J. Wang, W. Shen and Y. Q. Fu, *Journal of Materials Science*, 2018, DOI: 10.1007/s10853-018-2789-z.

249. S. C. Wang and M. O. Shaikh, *Sensors (Basel)*, 2015, **15**, 14286-14297.

250. Q. A. Drmosh, Z. H. Yamani, A. K. Mohamedkhair, A. H. Y. Hendi and A. Ibrahim, *Vacuum*, 2018, **156**, 68-77.

251. L. Chandra, P. K. Sahu, R. Dwivedi and V. N. Mishra, *Materials Research Express*, 2017, **4**, 125017.

252. O. Lupan, V. Postica, F. Labat, I. Ciofini, T. Pauporté and R. Adelung, *Sensors and Actuators B: Chemical*, 2018, **254**, 1259-1270.

253. J. M. Lee, J.-e. Park, S. Kim, S. Kim, E. Lee, S.-J. Kim and W. Lee, *International Journal of Hydrogen Energy*, 2010, **35**, 12568-12573.

254. K. Vijayalakshmi, A. Renitta and A. Monamary, *Journal of Materials Science-Materials in Electronics*, 2018, **29**, 21023-21032.

255. X. Wei, X. Yang, T. Wu, S. Wu, W. Li, X. Wang and Z. Chen, *International Journal of Hydrogen Energy*, 2017, **42**, 24580-24586.

256. W. Lu, D. Ding, Q. Xue, Y. Du, Y. Xiong, J. Zhang, X. Pan and W. Xing, *Sensors and Actuators B-Chemical*, 2018, **254**, 393-401.

257. Z. S. Hosseini, A. Mortezaali, A. Iraji zad and S. Fardindoost, *Journal of Alloys and Compounds*, 2015, **628**, 222-229.

258. F.-C. Chung, Z. Zhu, P.-Y. Luo, R.-J. Wu and W. Li, *Sensors and Actuators B: Chemical*, 2014, **199**, 314-319.

259. H. Wu, H. Huang, J. Zhou, D. Hong, M. Ikram, A. U. Rehman, L. Li and K. Shi, *Sci Rep*, 2017, **7**, 14688.

260. Z. Zhu, J.-L. Chang and R.-J. Wu, *Sensors and Actuators B: Chemical*, 2015, **214**, 56-62.

261. J. Liang, J. Liu, W. Li and M. Hu, *Materials Research Bulletin*, 2016, **84**, 332-339.

262. J. Liang, W. Li, J. Liu and M. Hu, *Materials Letters*, 2016, **184**, 92-95.

263. S. Park, H. Kim, C. Jin and C. Lee, *Journal of the Korean Physical Society*, 2012, **60**, 1560-1564.

264. S. Ren, G. Fan, S. Qu and Q. Wang, *Journal of Applied Physics*, 2011, **110**, 084312.

265. T.-R. Rashid, D.-T. Phan and G.-S. Chung, *Sensors and Actuators B: Chemical*, 2014, **193**, 869-876.

266. Z. Wang, Z. Li, T. Jiang, X. Xu and C. Wang, *ACS Appl Mater Interfaces*, 2013, **5**, 2013-2021.

267. W. P. Chen, Y. Xiong, Y. S. Li, P. Cui, S. S. Guo, W. Chen, Z. L. Tang, Z. Yan and Z. Zhang, *International Journal of Hydrogen Energy*, 2016, **41**, 3307-3312.

268. B. Liu, D. Cai, Y. Liu, D. Wang, L. Wang, Y. Wang, H. Li, Q. Li and T. Wang, *Sensors and Actuators B: Chemical*, 2014, **193**, 28-34.

269. P. Li, Z. Xiong, S. Zhu, M. Wang, Y. Hu, H. Gu, Y. Wang and W. Chen, *International Journal of Hydrogen Energy*, 2017, **42**, 30186-30192.

270. B. Huang, Y. Wang, Q. Hu, X. Mu, Y. Zhang, J. Bai, Q. Wang, Y. Sheng, Z. Zhang and E. Xie, *Journal of Materials Chemistry C*, 2018, **6**, 10935-10943.

271. M. Chitra, K. Uthayarani, N. Rajasekaran, N. Neelakandeswari, E. K. Girija and D. P. Padiyan, *Surface Review and Letters*, 2016, **23**, 1550094.

272. L. Yang, L. Li, Y. Yang, G. Zhang, L. Gong, L. Jing, H. Fu and K. Shi, *Materials Research Bulletin*, 2013, **48**, 3657-3665.

273. S. Jain, A. Patrike, S. S. Badadhe, M. Bhardwaj and S. Ogale, *ACS Omega*, 2018, **3**, 1977-1982.

274. N. Singh, C. Yan and P. S. Lee, *Sensors and Actuators B: Chemical*, 2010, **150**, 19-24.

275. H. Ahn, Y. Wang, S. Hyun Jee, M. Park, Y. S. Yoon and D.-J. Kim, *Chemical Physics Letters*, 2011, **511**, 331-335.

276. M. R. Modaberi, R. Rooydell, S. Brahma, A. A. Akande, B. W. Mwakikunga and C.-P. Liu, *Sensors and Actuators B-Chemical*, 2018, **273**, 1278-1290.

277. C. Stella, D. Prabhakar, M. Prabhu, N. Soundararajan and K. Ramachandran, *Journal of Materials Science: Materials in Electronics*, 2015, **27**, 1636-1644.

278. Z. Li, A. A. Haidry, T. Wang and Z. J. Yao, *Applied Physics Letters*, 2017, **111**, 032104.

279. A. Renitta and K. Vijayalakshmi, *Catalysis Communications*, 2016, **73**, 58-62.

280. K. Karthick, D. Srinivasan and J. B. Christopher, *Journal of Materials Science: Materials in Electronics*, 2017, **28**, 11979-11986.

281. J. Ma, Y. Liu, H. Zhang, P. Ai, N. Gong, Y. Wu and D. Yu, *Sensors and Actuators B: Chemical*, 2015, **216**, 72-79.

282. X. Zou, H. Fan, Y. Tian, M. Zhang and X. Yan, *Dalton Trans*, 2015, **44**, 7811-7821.

283. K. Khun Khun, A. Mahajan and R. K. Bedi, *Chemical Physics Letters*, 2010, **492**, 119-122.

284. A. J. Kulandaisamy, J. R. Reddy, P. Srinivasan, K. J. Babu, G. K. Mani, P. Shankar and J. B. B. Rayappan, *Journal of Alloys and Compounds*, 2016, **688**, 422-429.

285. J. M. Wu, *Nanotechnology*, 2010, **21**, 235501.

286. R. Jaisutti, M. Lee, J. Kim, S. Choi, T. J. Ha, J. Kim, H. Kim, S. K. Park and Y. H. Kim, *ACS Appl Mater Interfaces*, 2017, **9**, 8796-8804.

287. M. Kaur, S. Bhattacharya, M. Roy, S. K. Deshpande, P. Sharma, S. K. Gupta and J. V. Yakhmi, *Applied Physics A*, 2007, **87**, 91-96.

288. A. Chaparadza and S. B. Rananavare, *Nanotechnology*, 2008, **19**, 245501.

289. K. Vijayalakshmi and K. Karthick, *International Journal of Hydrogen Energy*, 2014, **39**, 7165-7172.

290. T. Pauporte, O. Lupan, V. Postica, M. Hoppe, L. Chow and R. Adelung, *Physica Status Solidi a-Applications and Materials Science*, 2018, **215**.

291. H. Liu, D. Ding, C. Ning and Z. Li, *Nanotechnology*, 2012, **23**, 015502.

292. H. Tang, M. Yan, H. Zhang, S. Li, X. Ma, M. Wang and D. Yang, *Sensors and Actuators B: Chemical*, 2006, **114**, 910-915.

293. P. M. Calaque, C. J. Vergara, L. I. Ballesteros and A. Somintac, 2017, **1808**, 020013.

294. T.-t. Li, R.-r. Zheng, H. Yu, L. Xia, Y. Yang and X.-t. Dong, *Solid State Ionics*, 2018, **325**, 17-23.

295. M. Bao, Y. Chen, F. Li, J. Ma, T. Lv, Y. Tang, L. Chen, Z. Xu and T. Wang, *Nanoscale*, 2014, **6**, 4063-4066.

296. G. Cui, P. Zhang, L. Chen, X. Wang, J. Li, C. Shi and D. Wang, *Sci Rep*, 2017, **7**, 43887.

297. D. R. Patil, L. A. Patil and P. P. Patil, *Sensors and Actuators B: Chemical*, 2007, **126**, 368-374.

298. S. Bhuvaneshwari, S. Papachan and N. Gopalakrishnan, 2017, **1832**, 050126.

299. C. Jiang, S. Xu, G. Zhang, L. Li, Y. Yang and K. Shi, *CrystEngComm*, 2013, **15**, 2482.

300. H. Wu, K. Kan, L. Wang, G. Zhang, Y. Yang, H. Li, L. Jing, P. Shen, L. Li and K. Shi, *CrystEngComm*, 2014, **16**, 9116-9124.

301. R. Lu, W. Zhou, K. Shi, Y. Yang, L. Wang, K. Pan, C. Tian, Z. Ren and H. Fu, *Nanoscale*, 2013, **5**, 8569-8576.

302. J. Zhang, D. Zeng, Q. Zhu, J. Wu, Q. Huang, W. Zhang and C. Xie, *Phys Chem Chem Phys*, 2016, **18**, 5386-5396.

303. X. Yue, T. Hong, Z. Yang and S. Huang, *Chinese Science Bulletin*, 2012, **58**, 821-826.

304. L. A. Patil and D. R. Patil, *Sensors and Actuators B: Chemical*, 2006, **120**, 316-323.

305. X. Liu, B. Du, Y. Sun, M. Yu, Y. Yin, W. Tang, C. Chen, L. Sun, B. Yang, W. Cao and M. N. Ashfold, *ACS Appl Mater Interfaces*, 2016, **8**, 16379-16385.

306. W. Zang, Y. Nie, D. Zhu, P. Deng, L. Xing and X. Xue, *The Journal of Physical Chemistry C*, 2014, **118**, 9209-9216.

307. D. Zhu, Y. Fu, W. Zang, Y. Zhao, L. Xing and X. Xue, *Materials Letters*, 2016, **166**, 288-291.

308. M.-R. Yu, G. Suyambrakasam, R.-J. Wu and M. Chavali, *Materials Research Bulletin*, 2012, **47**, 1713-1718.

309. J. Liang, R. Yang, K. Zhu and M. Hu, *Journal of Materials Science: Materials in Electronics*, 2017, **29**, 3780-3789.

310. D. R. Patil and L. A. Patil, *Sensors and Actuators B: Chemical*, 2007, **123**, 546-553.

311. L. F. da Silva, J. C. M'Peko, A. C. Catto, S. Bernardini, V. R. Mastelaro, K. Aguir, C. Ribeiro and E. Longo, *Sensors and Actuators B: Chemical*, 2017, **240**, 573-579.

312. A. Mirzaei, G.-J. Sun, J. K. Lee, C. Lee, S. Choi and H. W. Kim, *Ceramics International*, 2017, **43**, 5247-5254.

313. S. Park, H. Kheel, G.-J. Sun, H. W. Kim, T. Ko and C. Lee, *Metals and Materials International*, 2016, **22**, 730-736.

314. G. Lu, L. E. Ocola and J. Chen, *Nanotechnology*, 2009, **20**, 445502.

315. Y. Wang and S. Gong, *Journal of Materials Science: Materials in Electronics*, 2015, **26**, 5024-5029.

316. W. Yang, P. Wan, X. Zhou, J. Hu, Y. Guan and L. Feng, *ACS Appl Mater Interfaces*, 2014, **6**, 21093-21100.

317.    S. Liu, B. Yu, H. Zhang, T. Fei and T. Zhang, *Sensors and Actuators B: Chemical*, 2014, **202**, 272-278.

318.    H. Tai, Z. Yuan, W. Zheng, Z. Ye, C. Liu and X. Du, *Nanoscale Res Lett*, 2016, **11**, 130.

319.    Y. Yang, L. Sun, X. Dong, H. Yu, T. Wang, J. Wang, R. Wang, W. Yu and G. Liu, *RSC Advances*, 2016, **6**, 37085-37092.

320.    R. Ghosh, A. K. Nayak, S. Santra, D. Pradhan and P. K. Guha, *RSC Advances*, 2015, **5**, 50165-50173.

321.    S. Liu, Z. Wang, Y. Zhang, J. Li and T. Zhang, *Sensors and Actuators B: Chemical*, 2016, **228**, 134-143.

322.    Z. Wang, Y. Zhang, S. Liu and T. Zhang, *Sensors and Actuators B: Chemical*, 2016, **222**, 893-903.

323.    Z. Wang, T. Zhang, C. Zhao, T. Han, T. Fei, S. Liu and G. Lu, *J Colloid Interface Sci*, 2018, **514**, 599-608.

324.    M. Shojaee, S. Nasresfahani and M. H. Sheikhi, *Sensors and Actuators B: Chemical*, 2018, **254**, 457-467.

325.    T. Wang, J. Hao, S. Zheng, Q. Sun, D. Zhang and Y. Wang, *Nano Research*, 2017, **11**, 791-803.

326.    J. Zhang, J. Wu, X. Wang, D. Zeng and C. Xie, *Sensors and Actuators B: Chemical*, 2017, **243**, 1010-1019.

327.    P.-G. Su, F.-Y. Chen and C.-H. Wei, *Sensors and Actuators B: Chemical*, 2018, **254**, 1125-1132.

328.    D. Zhang, J. Liu and B. Xia, *Journal of Electronic Materials*, 2016, **45**, 4324-4330.

329.    Z. Wang, T. Zhang, T. Han, T. Fei, S. Liu and G. Lu, *Sensors and Actuators B-Chemical*, 2018, **266**, 812-822.

330.    Y.-l. Dong, X.-f. Zhang, X.-l. Cheng, Y.-m. Xu, S. Gao, H. Zhao and L.-h. Huo, *RSC Adv.*, 2014, **4**, 57493-57500.

331.    X. Liu, J. Li, J. Sun and X. Zhang, *RSC Advances*, 2015, **5**, 73699-73704.

332.    X. Liu, J. Sun and X. Zhang, *Sensors and Actuators B: Chemical*, 2015, **211**, 220-226.

333.    Y. Xia, J. Wang, J. L. Xu, X. Li, D. Xie, L. Xiang and S. Komarneni, *ACS Appl Mater Interfaces*, 2016, **8**, 35454-35463.

334.    J. Zhang, D. Zeng, S. Zhao, J. Wu, K. Xu, Q. Zhu, G. Zhang and C. Xie, *Phys Chem Chem Phys*, 2015, **17**, 14903-14911.

335.    F. Gu, R. Nie, D. Han and Z. Wang, *Sensors and Actuators B: Chemical*, 2015, **219**, 94-99.

336.    W. Fang, Y. Yang, H. Yu, X. Dong, R. Wang, T. Wang, J. Wang, Z. Liu, B. Zhao and X. Wang, *New Journal of Chemistry*, 2017, **41**, 7517-7523.

337.    X. Jiang, H. Tai, Z. Ye, Z. Yuan, C. Liu, Y. Su and Y. Jiang, *Materials Letters*, 2017, **186**, 49-52.

338.    J. Pan, W. Li, L. Quan, N. Han, S. Bai, R. Luo, Y. Feng, D. Li and A. Chen, *Industrial & Engineering Chemistry Research*, 2018, **57**, 10086-10094.

339.    Z. Li, Y. Liu, D. Guo, J. Guo and Y. Su, *Sensors and Actuators B-Chemical*, 2018, **271**, 306-310.

340.    N. Chen, X. Li, X. Wang, J. Yu, J. Wang, Z. Tang and S. A. Akbar, *Sensors and Actuators B: Chemical*, 2013, **188**, 902-908.

341.    Y. Yang, C. Tian, J. Wang, L. Sun, K. Shi, W. Zhou and H. Fu, *Nanoscale*, 2014, **6**, 7369-7378.

342.    Y. Yang, C. Tian, L. Sun, R. Lü, W. Zhou, K. Shi, K. Kan, J. Wang and H. Fu, *Journal of Materials Chemistry A*, 2013, **1**, 12742.

343.    R. Kumar, N. Kushwaha and J. Mittal, *Sensors and Actuators B: Chemical*, 2017, **244**, 243-251.

344.    Y. Chen, W. Zhang and Q. Wu, *Sensors and Actuators B: Chemical*, 2017, **242**, 1216-1226.

345.    X. Li, Y. Zhao, X. Wang, J. Wang, A. M. Gaskov and S. A. Akbar, *Sensors and Actuators B: Chemical*,

2016, **230**, 330-336.

346. H. Meng, W. Yang, K. Ding, L. Feng and Y. Guan, *Journal of Materials Chemistry A*, 2015, **3**, 1174-1181.

347. G. Singh, A. Choudhary, D. Haranath, A. G. Joshi, N. Singh, S. Singh and R. Pasricha, *Carbon*, 2012, **50**, 385-394.

348. F. Schutt, V. Postica, R. Adelung and O. Lupan, *ACS Appl Mater Interfaces*, 2017, **9**, 23107-23118.

349. G. P. Evans, M. J. Powell, I. D. Johnson, D. P. Howard, D. Bauer, J. A. Darr and I. P. Parkin, *Sensors and Actuators B: Chemical*, 2018, **255**, 1119-1129.

350. Z. Bo, M. Yuan, S. Mao, X. Chen, J. Yan and K. Cen, *Sensors and Actuators B: Chemical*, 2018, **256**, 1011-1020.

351. Z. Ye, H. Tai, T. Xie, Z. Yuan, C. Liu and Y. Jiang, *Sensors and Actuators B: Chemical*, 2016, **223**, 149-156.

352. D. Acharyya and P. Bhattacharyya, *IEEE Electron Device Letters*, 2016, **37**, 656-659.

353. D. Zhang, Y. e. Sun and Y. Zhang, *Journal of Materials Science: Materials in Electronics*, 2015, **26**, 7445-7451.

354. D. Zhang, C. Jiang, J. Liu and Y. Cao, *Sensors and Actuators B: Chemical*, 2017, **247**, 875-882.

355. A. Yang, X. Tao, R. Wang, S. Lee and C. Surya, *Applied Physics Letters*, 2007, **91**, 133110.

356. D. Zhang, A. Liu, H. Chang and B. Xia, *RSC Advances*, 2015, **5**, 3016-3022.

357. D. Kathiravan, B. R. Huang and A. Saravanan, *ACS Appl Mater Interfaces*, 2017, **9**, 12064-12072.

358. D. Zhang, N. Yin, C. Jiang and B. Xia, *Journal of Materials Science: Materials in Electronics*, 2016, **28**, 2763-2768.

359. S. Dhall and N. Jaggi, *Sensors and Actuators B: Chemical*, 2015, **210**, 742-747.

360. S. G. Chatterjee, S. Dey, D. Samanta, S. Santra, S. Chatterjee, P. K. Guha and A. K. Chakraborty, *Journal of Materials Science-Materials in Electronics*, 2018, **29**, 20162-20171.

361. Y. Peng, L. Zheng, K. Zou and C. Li, *Nanotechnology*, 2017, **28**.

362. M. Shojaee, S. Nasresfahani and M. H. Sheikhi, *Sensors and Actuators B-Chemical*, 2018, **254**, 457-467.

363. S. Nasresfahani, M. H. Sheikhi, M. Tohidi, A. Zarifkar and Ieee, in *2016 24th Iranian Conference on Electrical Engineering*, 2016, pp. 1014-1018.

364. Z. Wang, Y. Zhang, S. Liu and T. Zhang, *Sensors and Actuators B-Chemical*, 2016, **222**, 893-903.

365. P.-G. Su and L.-Y. Yang, *Sensors and Actuators B-Chemical*, 2016, **223**, 202-208.

366. P.-G. Su, F.-Y. Chen and C.-H. Wei, *Sensors and Actuators B-Chemical*, 2018, **254**, 1125-1132.

367. S. Ghosal and P. Bhattacharyya, *Microelectronics Reliability*, 2017, **78**, 299-306.

368. N. Du, H. Zhang, X. Ma and D. Yang, *Chemical Communications*, 2008, DOI: 10.1039/b812695j, 6182-6184.

369. T. Wang, J. Hao, S. Zheng, Q. Sun, D. Zhang and Y. Wang, *Nano Research*, 2018, **11**, 791-803.

370. S. Liu, Z. Wang, Y. Zhang, J. Li and T. Zhang, *Sensors and Actuators B-Chemical*, 2016, **228**, 134-143.

371. J. Hu, C. Zou, Y. Su, M. Li, X. Ye, B. Cai, E. S.-W. Kong, Z. Yang and Y. Zhang, *Sensors and Actuators B-Chemical*, 2018, **270**, 119-129.

372. D. Ding, Q. Xue, W. Lu, Y. Xiong, J. Zhang, X. Pan and B. Tao, *Sensors and Actuators B: Chemical*, 2018, **259**, 289-298.

373. B.-Y. Wei, M.-C. Hsu, P.-G. Su, H.-M. Lin, R.-J. Wu and H.-J. Lai, *Sensors and Actuators B: Chemical*, 2004, **101**, 81-89.

374.    G. Lu, L. E. Ocola and J. Chen, *Advanced Materials*, 2009, **21**, 2487-2491.

375.    R. Leghrib, A. Felten, J. J. Pireaux and E. Llobet, *Thin Solid Films*, 2011, **520**, 966-970.

376.    X. Luo, H. Giessen, Y. Zhou, G. Xie, T. Xie, T. Kang and Y. Jiang, 2014, **9285**, 928509.

377.    A. Sharma, M. Tomar and V. Gupta, *Journal of Materials Chemistry*, 2012, **22**, 23608.

378.    M. Asad and M. H. Sheikhi, *Sensors and Actuators B: Chemical*, 2016, **231**, 474-483.

379.    H. Liu, W. Zhang, H. Yu, L. Gao, Z. Song, S. Xu, M. Li, Y. Wang, H. Song and J. Tang, *ACS Appl Mater Interfaces*, 2016, **8**, 840-846.

380.    K. Anothainart, M. Burgmair, A. Karthigeyan, M. Zimmer and I. Eisele, *Sensors and Actuators B: Chemical*, 2003, **93**, 580-584.

381.    L. Meng, Q. Xu, Z. Sun, G. Li, S. Bai, Z. Wang and Y. Qin, *Materials Letters*, 2018, **212**, 296-298.

382.    P. Wang, Y. Fu, B. Yu, Y. Zhao, L. Xing and X. Xue, *Journal of Materials Chemistry A*, 2015, **3**, 3529-3535.

383.    L. Peng, Q. Zhao, D. Wang, J. Zhai, P. Wang, S. Pang and T. Xie, *Sensors and Actuators B: Chemical*, 2009, **136**, 80-85.

384.    J. Cui, L. Shi, T. Xie, D. Wang and Y. Lin, *Sensors and Actuators B: Chemical*, 2016, **227**, 220-226.

385.    L. Vogel, R. Wagner, R. Moos and D. Schoenauer-Kamin, *Functional Materials Letters*, 2018, **11**.

386.    N. D. Chinh, N. D. Quang, H. Lee, T. Thi Hien, N. M. Hieu, D. Kim, C. Kim and D. Kim, *Sci Rep*, 2016, **6**, 35066.

387.    D. Klaus, D. Klawinski, S. Amrehn, M. Tiemann and T. Wagner, *Sensors and Actuators B: Chemical*, 2015, **217**, 181-185.

388.    X. Li, X. Li, J. Wang and S. Lin, *Sensors and Actuators B: Chemical*, 2015, **219**, 158-163.

389.    T. Xie, N. Sullivan, K. Steffens, B. Wen, G. Liu, R. Debnath, A. Davydov, R. Gomez and A. Motayed, *Journal of Alloys and Compounds*, 2015, **653**, 255-259.

390.    J. D. Prades, R. Jimenez-Diaz, F. Hernandez-Ramirez, S. Barth, A. Cirera, A. Romano-Rodriguez, S. Mathur and J. R. Morante, *Sensors and Actuators B: Chemical*, 2009, **140**, 337-341.

391.    Y. Xiong, W. Lu, D. Ding, L. Zhu, X. Li, C. Ling and Q. Xue, *Acs Sensors*, 2017, **2**, 679-686.

392.    H. Chen, Y. Liu, C. Xie, J. Wu, D. Zeng and Y. Liao, *Ceramics International*, 2012, **38**, 503-509.

393.    G. Lu, J. Xu, J. Sun, Y. Yu, Y. Zhang and F. Liu, *Sensors and Actuators B: Chemical*, 2012, **162**, 82-88.

394.    J. Sun, J. Xu, Y. Yu, P. Sun, F. Liu and G. Lu, *Sensors and Actuators B: Chemical*, 2012, **169**, 291-296.

395.    X. Li, N. Chen, S. Lin, J. Wang and J. Zhang, *Sensors and Actuators B: Chemical*, 2015, **209**, 729-734.

396.    J. Cui, D. Wang, T. Xie and Y. Lin, *Sensors and Actuators B: Chemical*, 2013, **186**, 165-171.

397.    R. Gao, Z. Ying, W. Sheng and P. Zheng, *Materials Letters*, 2018, **229**, 210-212.

398.    X. Geng, C. Zhang, Y. Luo, H. Liao and M. Debliquy, *Ceramics International*, 2017, **43**, 5990-5998.

399.    X. Geng, C. Zhang, Y. Luo and M. Debliquy, *Applied Surface Science*, 2017, **401**, 248-255.

400.    T. Wang, Q. Yu, S. Zhang, X. Kou, P. Sun and G. Lu, *Nanoscale*, 2018, **10**, 4841-4851.

401.    K. Zhang, M. Peng, W. Wu, J. Guo, G. Gao, Y. Liu, J. Kou, R. Wen, Y. Lei, A. Yu, Y. Zhang, J. Zhai and Z. L. Wang, *Materials Horizons*, 2017, **4**, 274-280.

402.    W. L. Ong, C. Zhang and G. W. Ho, *Nanoscale*, 2011, **3**, 4206-4214.

403.    R. Li, K. Jiang, S. Chen, Z. Lou, T. Huang, D. Chen and G. Shen, *RSC Advances*, 2017, **7**, 52503-52509.

404.    T. M. Perfecto, C. A. Zito, T. Mazon and D. P. Volanti, *Journal of Materials Chemistry C*, 2018, **6**,

2822-2829.

405. X. Geng, C. Zhang, Y. Luo and M. Debliquy, *Journal of the Taiwan Institute of Chemical Engineers*, 2017, **75**, 280-286.

406. C. Hua, Y. Shang, Y. Wang, J. Xu, Y. Zhang, X. Li and A. Cao, *Applied Surface Science*, 2017, **405**, 405-411.

407. S. Knobelspies, B. Bierer, A. Daus, A. Takabayashi, G. A. Salvatore, G. Cantarella, A. Ortiz Perez, J. Wollenstein, S. Palzer and G. Troster, *Sensors (Basel)*, 2018, **18**.

408. S. J. Choi, H. J. Choi, W. T. Koo, D. Huh, H. Lee and I. D. Kim, *ACS Appl Mater Interfaces*, 2017, **9**, 40593-40603.

409. S. M. Mohammad, Z. Hassan, R. A. Talib, N. M. Ahmed, M. A. Al-Azawi, N. M. Abd-Alghafour, C. W. Chin and N. H. Al-Hardan, *Journal of Materials Science: Materials in Electronics*, 2016, **27**, 9461-9469.

410. A. S. M. I. Uddin and G.-S. Chung, *Journal of Electroceramics*, 2018, **40**, 42-49.

411. D. K. Subbiah, G. K. Mani, K. J. Babu, A. Das and J. B. B. Rayappan, *Journal of Cleaner Production*, 2018, **194**, 372-382.

412. H.-Y. Li, C.-S. Lee, D. H. Kim and J.-H. Lee, *Acs Applied Materials & Interfaces*, 2018, **10**, 27858-27867.

413. C. Liu, H. Tai, P. Zhang, Z. Yuan, X. Du, G. Xie and Y. Jiang, *Sensors and Actuators B-Chemical*, 2018, **261**, 587-597.

414. V. Annapureddy, Y. Kim, G.-T. Hwang, H. W. Jang, S.-D. Kim, J.-J. Choi, B. Cho and J. Ryu, *Advanced Materials Interfaces*, 2018, **5**.

415. S. Li, P. Lin, L. Zhao, C. Wang, D. Liu, F. Liu, P. Sun, X. Liang, F. Liu, X. Yan, Y. Gao and G. Lu, *Sensors and Actuators B-Chemical*, 2018, **259**, 505-513.

416. U. Yaqoob, D.-T. Phan, A. S. M. I. Uddin and G.-S. Chung, *Sensors and Actuators B: Chemical*, 2015, **221**, 760-768.

417. U. Yaqoob, A. S. M. I. Uddin and G.-S. Chung, *Sensors and Actuators B: Chemical*, 2016, **224**, 738-746.

418. D. K. Bandgar, S. T. Navale, Y. H. Navale, S. M. Ingole, F. J. Stadler, N. Ramgir, D. K. Aswal, S. K. Gupta, R. S. Mane and V. B. Patil, *Materials Chemistry and Physics*, 2017, **189**, 191-197.

419. K. K. Sadasivuni, D. Ponnamma, H.-U. Ko, H. C. Kim, L. Zhai and J. Kim, *Sensors and Actuators B-Chemical*, 2016, **233**, 633-638.

420. S. Li, Y. Diao, Z. Yang, J. He, J. Wang, C. Liu, F. Liu, H. Lu, X. Yan, P. Sun and G. Lu, *Sensors and Actuators B-Chemical*, 2018, **276**, 526-533.

421. X. Luo, K. You, Y. Hu, S. Yang, X. Pan, Z. Wang, W. Chen and H. Gu, *International Journal of Hydrogen Energy*, 2017, **42**, 8399-8405.

422. Z. Pang, Z. Yang, Y. Chen, J. Zhang, Q. Wang, F. Huang and Q. Wei, *Colloids and Surfaces a-Physicochemical and Engineering Aspects*, 2016, **494**, 248-255.

423. A. Bagal, E. C. Dandley, J. Zhao, X. A. Zhang, C. J. Oldham, G. N. Parsons and C.-H. Chang, *Materials Horizons*, 2015, **2**, 486-494.

424. A. Sanaeifar, H. ZakiDizaji, A. Jafari and M. d. l. Guardia, *TrAC Trends in Analytical Chemistry*, 2017, **97**, 257-271.

425. Y. Zhang, J. Zhao, T. Du, Z. Zhu, J. Zhang and Q. Liu, *Sci Rep*, 2017, **7**, 1960.

426. A. B. Far, F. Flitti, B. Guo and A. Bermak, *IEEE Sensors Journal*, 2009, **9**, 713-722.

427. F. Flitti, A. Far, B. Guo and A. Bermak, *Journal of Sensors*, 2008, **2008**, 1-6.